Viscoelastic properties of glass-forming polymer melts

Stephan Frey

UNIVERSITÉ DE STRASBOURG

Thèse présentée pour obtenir le titre de
Docteur de l'Université de Strasbourg
Discipline : Physique

Propriétés viscoélastiques des fondus de polymères vitrifiables

Stephan Frey

Thèse soutenue publiquement le 29 juin 2012

Membres du Jury :

Directeur de thèse :	**J. Baschnagel** Professeur Université de Strasbourg
Co-directeur de thèse :	**H. Meyer** Chargé de recherche, Institut Charles Sadron, Strasbourg
Co-directeur de thèse :	**M. Fuchs** Professeur Universität Konstanz
Rapporteur externe :	**J. Horbach** Professeur Universität Düsseldorf
Rapporteur externe :	**W. Kob** Professeur Université de Montpellier
Examinateur externe :	**A. Blumen** Professeur Universität Freiburg
Examinateur interne :	**P.-A. Hervieux** Professeur Université de Strasbourg

To Henrika who loves dedications

M. Stephan Frey a été membre de la promotion Jane Goodall du Collège Doctoral Européen de l'Université de Strasbourg pendant la préparation de sa thése de 2010 à 2012. Il a bénéficié des aides spécifiques du CDE et a suivi un enseignement hebdomadaire sur les affaires européennes dispensé par des spécialistes internationaux. Ses travaux de recherche ont été effectués dans le cadre d'une convention de cotutelle avec l'Université de Konstanz, Allemagne, et l'Université de Strasbourg.

Mr. Stephan Frey was a member of the European Doctoral College of the University of Strasbourg during the preparation of his PhD, from 2010 to 2012, class Jane Goodall. He benefited from specific financial supports offered by the EDC and, along with his mainstream research, has followed a special course on topics of general European interests presented by international experts. This PhD research project has been led with the collaboration of two universities: the University of Konstanz, Germany, and the University of Strasbourg.

Acknowledgments

I thank all those who supported me while I was working on this thesis.

First of all I wish to thank Prof. Dr. Jörg Baschnagel for the inspiring discussions and his passion for physics that never failed to motivate me, and that his door was always open to discuss physics and everything else.

I thank Dr. Hendrik Meyer for his valuable guidance and the tenacity he showed towards my work. I profited greatly from his experience in simulation and his expertise in polymer physics.

I had the great privilege to also be a member of the "Soft Matter Theory" group of Prof. Dr. Matthias Fuchs. During my stay in Konstanz I benefited greatly from his helpful advice and useful discussions, for which I am very thankful.

I thank all the jury members and especially the referees for their time and effort: Prof. Dr. Jörg Baschnagel, Dr. Hendrik Meyer, Prof. Dr. Matthias Fuchs, Prof. Dr. Jürgen Horbach, Prof. Dr. Walter Kob, Prof. Dr. Alexander Blumen and Prof. Dr. Paul-Antoine Hervieux.

I acknowledge financial support from the Ministère de l'Enseignement Supérieur et de la Recherche in the framework of the International Research Training Group "Soft Condensed Matter Physics of Model Systems".

In his capacity as a system administrator Dr. Olivier Benzerara solved numerous computer problems, and in his capacity as a French man he helped me navigate the French administrative system. Special thanks to all the members of the "Theory and Simulation of Polymers" group at the Institut Charles Sadron, who enriched my time in Strasbourg both in and outside the institute. Moreover I am grateful to all the members of the "Soft Matter Theory" group, who made my 2011 stay in Konstanz so enjoyable.

Last but not least I wish to thank my parents for their continuous love and support.

And most of all to Henrika.

Contents

Résumé

L'utilisation des polymères influence une grande partie de notre vie quotidienne; notre époque pourrait, sans exagération, être appelée l'âge des polymères [68]. L'impact du développement de la chimie des polymères sur nos habitudes de consommation moderne a été important: la plupart des matériaux d'emballage est fait de polymères solides [44]. L'exemple le plus simple d'une molécule de polymère est une longue chaîne linéaire liant N unités élémentaires un peu à la manière d'un collier de perles [30, 71]. Les matériaux d'emballage sont présents sous forme solide, le plus souvent dans l'état vitreux ou semi-cristallin. Pour leur utilisation, il est important de comprendre les propriétés viscoélastiques des fondus de polymères [68, 71].

Les constituants d'un polymère sont nommés monomères et ont une taille typique de ~ 0.5 nm. Dans le fondu de polymères les monomères remplissent le volume quasiment dans son intégralité et ne présentent aucun ordre à longue distance [11]. Lors du refroidissement, la structure de l'ensemble ne change que légèrement, une propriété qui est aussi connue pour les liquides simples surfondus [17, 20]. Les monomères sont beaucoup plus petits que le polymère qu'ils forment. La taille d'un polymère se mesure, par exemple, par le rayon de gyration R_g [26, 39, 71]. Celui-ci est accessible de manière expérimentale à partir de méthodes de diffraction de la lumière ou de diffusion de neutrons [46] et varie de 10 nm à 100 nm [11]. À plus grandes échelles les polymères présentent une structure auto-similaire ce qui permet de les traiter théoriquement comme des fractales [24, 68].

Dans un fondu de polymères les interactions inter-moléculaires agissant sur un polymère sont ecrantées par les polymères voisins. Ceci est dû au fait que, en moyenne, un polymère interagit avec $\sqrt{N}$ autres chaînes [24, 26, 68]. Le fait que les chaînes puissent se pénétrer les unes les autres si massivement implique des contraintes topologiques [24, 26, 56]. Le résultat de ces enchevêtrements est une viscosité élevée en raison du fort ralentissement de la dynamique de la chaîne [11].

À l'approche de la température de transition vitreuse, T_{g} [53, 61], les fondus de

polymères subissent une augmentation remarquable de leur viscosité de plusieurs ordres de grandeur. Cette forte augmentation est observée pour tous les temps de relaxation structurale et ceci est un exemple caractéristique des liquides vitrifiables polymériques et non-polymériques. [18, 27].

En comparaison de ce changement dramatique de dynamique, la structure du fondu ne subit que très peu de changements lors du refroidissement. Comprendre l'origine des phenomènes intervenant dans la transition vitreuse reste l'un des plus grands défis de la physique de la matière molle [7, 17, 25].

But de cette étude. Le but de cette étude est d'acquérir une compréhension approfondie des processus qui sont impliqués dans ce phénomène de transition vitreuse. Nous abordons ce problème par une approche numérique grâce aux simulations sur ordinateur en utilisant un modèle générique "bead-spring" [48]. Dans ce modèle les polymères sont modélisés par des chaînes flexibles possédant un volume exclu. La présente étude s'appuie sur des travaux antérieurs [4, 15, 22]. Ici, nous étudions en particulier l'influence de la longueur de la chaîne sur les propriétés dynamiques d'un fondu de polymères, ceux-ci étant principalement analysés dans le cadre méthodologique de la théorie de couplage de mode [4, 22, 23, 37].

Nous utilisons un modèle de simulation très semblable au modèle de polymères précédemment étudié, par Bennemann et al. [12–15], de manière systématique pour le régime de surfusion. L'analyse a été effectuée en relation avec les fonctions de diffusion cohérente et incohérente, les fonctions de corrélation des modes de Rouse et divers déplacements carré moyens (voir Réf. [11]).

En parallèle, le modèle a également été utilisé pour étudier les films minces confinés [11] ainsi que les films minces de polymères avec des surfaces libres (interface film/volume libre) [64, 65]. L'influence de particules de solvant dissoute dans le film a également été étudiée [66]. Le travail sur les films avec une interface polymère/air a été effectué à une pression nulle $p = 0$ qui est le choix le plus naturel pour des simulation de surfaces libres. Nous employons principalement la même pression dans nos simulations.

Nous étudions en particulier les petites chaînes (non enchevêtrées) comme suggéré par [69]. C'est dans ce domaine de longueur que la plus forte dépendance de T_g en fonction de la longueur de chaîne peut être observée. Cette analyse se concentre essentiellement sur les fonctions de diffusion résolues dans le temps et son autocorrélation temporelle en essayant d'atteindre des températures inférieures à ce qu'il

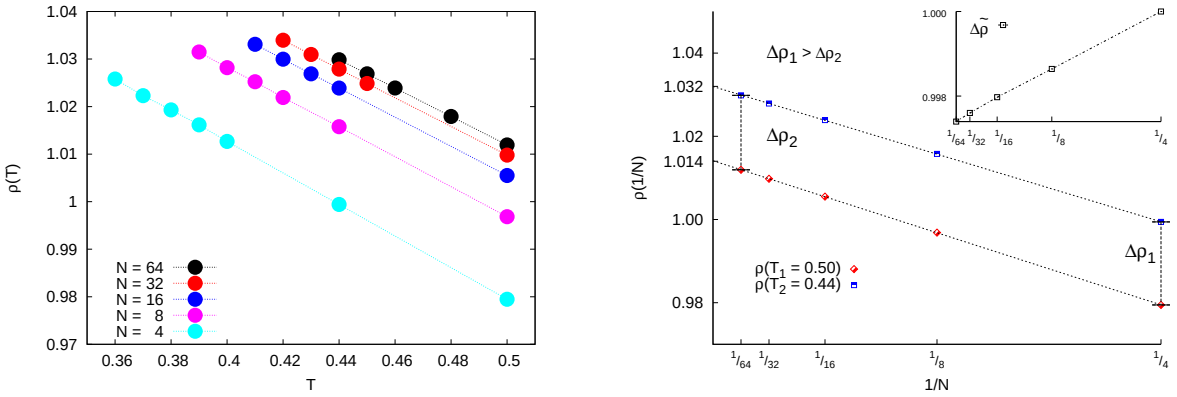

Figure 1: La densité ρ en fonction de la température T pour différentes longueurs de chaîne (à gauche). La densité ρ en fonction de l'inverse de la longueur de chaîne $1/N$ pour des températures $T = 0.44, 0.50$ (à droite). Insert: Un écart de $\Delta\tilde{\rho} = \frac{\rho(T_2,N)/\rho(T_1,N)}{\rho(T_2,N=4)/\rho(T_1,N=4)}$ à partir de 1 indique une déviation de la proportion de $\frac{\rho(T_2,N)}{\rho(T_1,N)}$ de celle de $\frac{\rho(T_2,N=4)}{\rho(T_1,N=4)}$. Cet écart croît presque linéairement avec l'augmentation de N.

était possible d'avoir dans les travaux antérieurs [4, 15, 22]. Nous étudions aussi la fonction de relaxation de cisaillement qui est expérimentalement pertinente, mais difficile à déterminer avec une statistique satisfaisante par simulation numérique [52, 54, 75].

Pour être en mesure d'étudier des systèmes de taille importante nous devons faire usage d'architectures informatiques parallèles. Nous avons décidé de travailler avec le code LAMMPS [49, 67].

Dans la première partie de notre travail, nous avons testé les paramètres pour un système monodisperse de taille de chaine $N = 10$ à la pression $p = 1$, où il était possible de comparer avec des données de références [1–4]. Puis nous avons choisi d'effectuer une variation systématique de la longueur de chaîne, ceci à une plus basse pression, $p = 0$, afin que nos données puissent servir de référence pour des travaux futurs sur des films avec une surface libre.

Dans la suite de ce résumé nous présentons les points importants de cette thèse qui commence par une introduction des méthodes de simulation. Dans cette introduction nous précisons le modèle de simulation que nous utilisons ainsi que la procédure pour générer des configurations au sein de la gamme de température de $2T_g \gtrsim T \gtrsim T_g$.

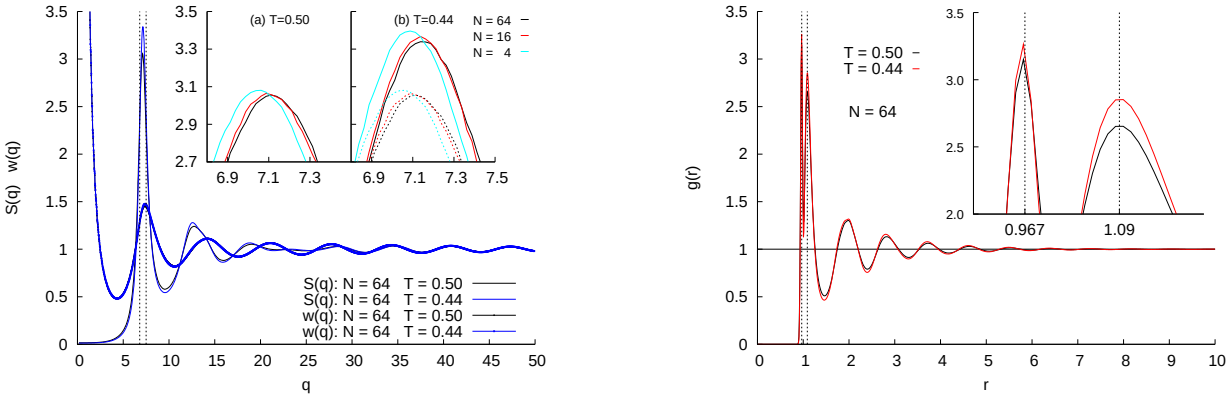

Figure 2: À gauche: Figure principale: Facteur de structure statique pour N = 64 et $T = 0.50, 0.44$ en fonction du module de l'onde vecteur **q**. Insert (a): facteur de structure statique pour N $= 64, 16, 4$ et $T = 0.50$. Insert (b): facteur de structure statique pour N $= 64, 16, 4$ et $T = 0.44$; les pointillés indiquent le facteur de structure statique pour $T = 0.50$. À droite: Figure principale: La fonction de distribution radiale pour les températures $T = 0.50$ et 0.44 ($N = 64$). Insert: zoom sur les maxima.

Nous analysons la densité en fonction de la température pour différentes longueurs de chaîne. Le graphe à gauche de la Fig. 1 montre la densité en fonction de la longueur de chaîne qui est analysée pour $T = 0.44$ et $T = 0.50$ (voir à droite de la Fig. 1). On constate que l'évolution de la densité peut être décrite par $\rho(N) = \rho_\infty\big(1 - \frac{\text{const}_T}{N}\big)$.

Le facteur de structure statique $S(q)$ [9, 21] est une fonction de la température T et de la longueur de chaîne (voir Fig. 2). Une signature de la dépendance de la densité à la longueur de chaîne est observée pour $S(q)$. Nous calculons de la même manière la fonction de distribution radiale [21] (voir Fig. 2).

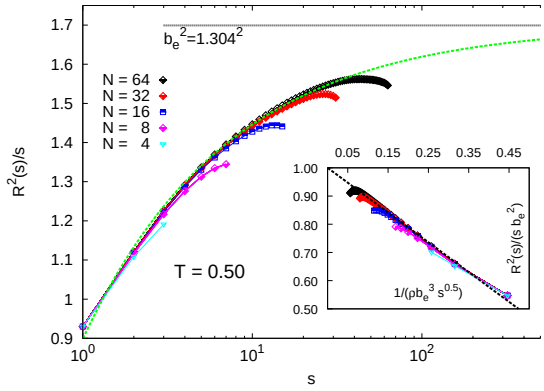

Figure 3: Figure principale: Distances quadratiques moyennes intra-chaîne pour N $= 64, 32, 16, 8, 4$ en fonction de distance curviligne s pour $T = 0.50$. $\frac{R_s^2}{s}$ est approché par la ligne pointillée comme décrit en Réf [79] pour déterminer la longueur de la liaison efficace b_e qui se trouve être $b_e = 1,304$ pour $T = 0.50$. Insert: $R^2(s)/(sb_e^2)$ en fonction de $1/(\rho b_e^3\sqrt{s})$. La ligne noire en pointillés est donnée par $f(x) = 1-c_1\sqrt{\frac{24}{\pi^3}}\,x$ [79]. Ainsi, la conformité de $\frac{R_s^2}{s}$ pour $N = 4, 8, 16, 32, 64$ avec elle représente la précision de l'ajustement.

Dans la partie suivante, nous analysons la longueur de liaison effective, comme le suggère la Réf. [79]. La Figure 3 montre l'analyse à $T = 0.50$. Il se trouve que la longueur de la liaison effective diminue en fonction de T. Ce comportement contre-intuitif provient de la flexibilité du modèle employé qui n'est chimiquement pas réaliste.

Par la suite, la dynamique des systèmes est analysée dans le cadre de la MCT, théorie de couplage de mode idéale [37]. Le principe de superposition des temps et des températures et le théorème de factorisation — deux prédictions de base de la MCT — sont analysés pour toutes les longueurs de chaîne (voir Fig. 4 où cette procédure est décrite pour $N = 64$). En outre, l'analyse suggère un intervalle de température approximatif où la MCT devrait être applicable.

Dans une étape ultérieure les exposants de "von Schweidler" b sont déterminés en fonction de la longueur de chaîne en ajustant les fonctions de diffusion cohérente tel que suggéré par la Réf. [11], selon l'équation suivante:

$$\phi_q(t) = f_q^{\rm c} - \widetilde{h}_q^{\rm fit}\,(t/t'_\sigma)^b + \widetilde{h}_q^{\rm fit}\widetilde{B}_q^{\rm fit}\,(t/t'_\sigma)^{2b} \qquad (t_\sigma \le t)\ . \tag{1}$$

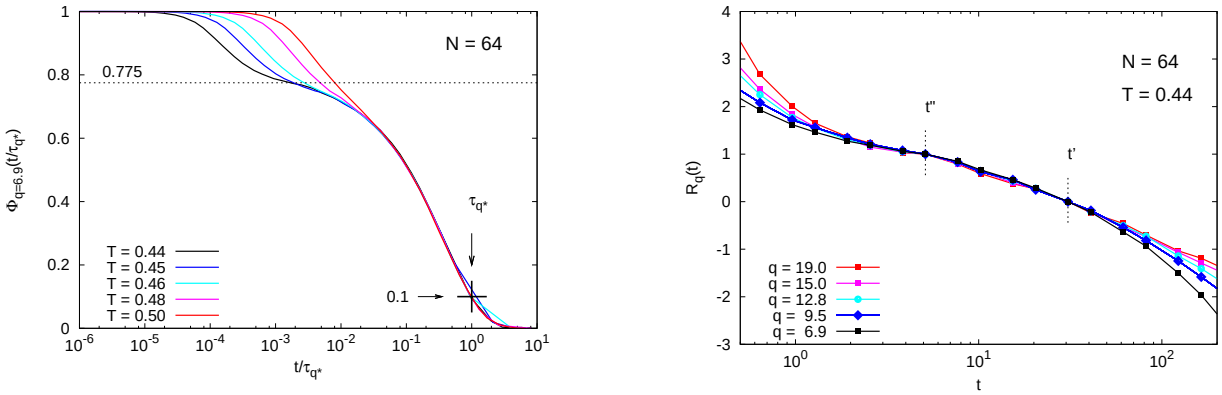

Figure 4: À gauche: La fonction de diffusion cohérente $\phi_{q=6.9}(t)$ pour $N = 64$ redimmensionnée en fonction du temps de relaxation α, $(\tau_{q^*})^{-1}$, qui est déterminé par $\phi_{q=6.9}(t = \tau_{q^*}) = 0.1$. À droite: Le théorème de factorisation est testé pour $T = 0.44$ et $N = 64$. Par définition $R_q(t'' = 5.12) = 1$ et $R_q(t' = 30.7)$=0. Les temps t'' et t' sont choisis de telle sorte qu'ils se trouvent dans la région correspondant au plateau. Le théorème de factorisation est validé: les courbes pour des valeurs différentes de q se superposent.

Ici $f_q^{\rm c}$ représente le paramètre non-ergodique, t'_σ le temps de relaxation α, et b l'exposant de "von Schweidler". Le paramètre $\widetilde{h}_q^{\rm fit}$ est donné par $h_q B$ où h_q désigne l'amplitude critique et B est une constante. Le paramètre $\widetilde{B}_q^{\rm fit}$ est donné par BB_q où B_q est dépendante de q.

En ajustant le temps de relaxation α, nous déterminons la température critique $T_{\rm c}$ de la théorie MCT en fonction de la longueur de chaîne N (voir Fig. 5). Il se trouve que les valeurs obtenues pour $T_{\rm c}$ peuvent être remises à l'échelle en fonction de l'inverse de la longueur de chaîne ce qui est représenté sur la Fig. 6.

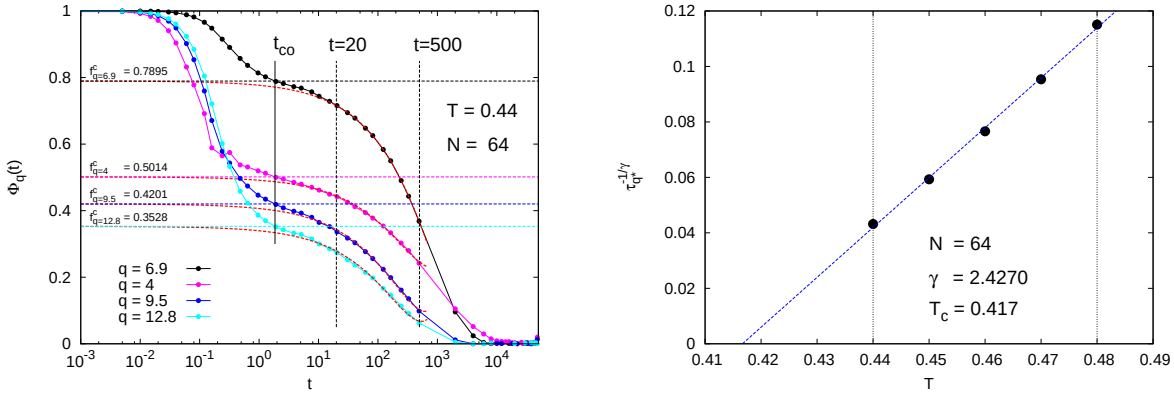

Figure 5: À gauche: La fonction de diffusion cohérente $\phi_{q=4,6.9,9.5,12.8}(t)$ pour $N = 64$ et $T = 0.44$; ajustée par rapport à Eq. (1). À droite: $N = 64$: Le temps de relaxation α pour $T = 0.44, 0.45, 0.46, 0.47, 0.48$ à $q = 6.9$. Le temps de relaxation α pour $\phi_{q=6.9}(t)$ est ajusté en fonction de $f(x) = A(x - T_c)$ où A et T_c sont les paramètres d'ajustement.

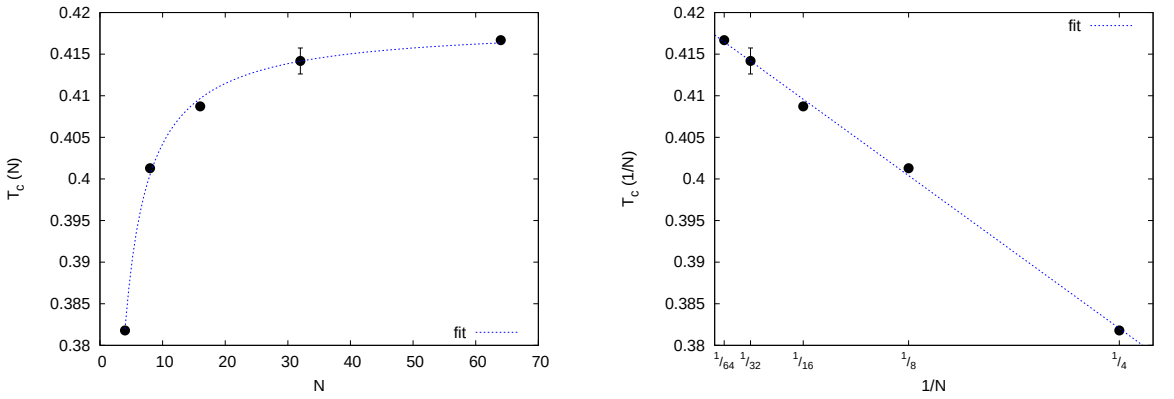

Figure 6: À gauche: T_c en fonction de la longueur de chaîne N. La ligne bleue indique un ajustement de la fonction $f(x) = Ax^{\alpha} + B$. À droite: T_c en fonction de l'inverse de la longueur de chaîne. La ligne bleue représente un ajustement linéaire donnée par $f(x) = Ax + B$.

En outre, nous sommes en mesure de calculer la fonction de diffusion cohérente avec une haute résolution afin que la queue de la courbe pour les grands temps, spécifiques aux polymères, devienne visible (voir bas de la Fig. 7).

Après l'analyse des fonctions de diffusion, nous considérons la fonction de relaxation de cisaillement [54] comme une quantité supplémentaire. En utilisant la fonction de relaxation de cisaillement, les systèmes considérés sont étudiés sur des échelles de longueur plus grandes. Nous avons constaté que les processus de relaxation polymériques, qui peuvent être décrits par la théorie de Rouse [26], ne sont pas modifiés, mais décalés vers des temps plus importants en approchant la transition vitreuse. Un comportement similaire est également observé par l'analyse de la fonction de diffusion pour les plus petites valeurs de q accessibles par la simulation (voir bas de Fig. 7). Cette étude montre que les effets significatifs de la structure polymère — qui montrent une signature en loi de puissance — ne deviennent visibles que pour les plus petites valeurs q et les chaînes les plus longues que nous avons étudiées.

La mise à l'échelle du déplacement quadratique moyen en fonction de la constante de diffusion montre un comportement d'échelle analogue à la fonction de diffusion cohérente en fonction du temps de relaxation α (voir Fig. 8). Pour la fonction de relaxation de cisaillement une mise à l'échelle selon une seule de ces quantités ne conduit pas à un résultat complètement satisfaisant.

Dans la dernière partie, nous entreprenons une étude sur les effets de taille finie. À cette fin, nous comparons deux tailles de système pour des polymères d'une longueur de chaîne $\mathrm{N} = 10$. Cette comparaison porte sur la fonction du déplacement quadratique moyen (voir Fig. 9). Ces fonctions mesurées à partir de ces deux systèmes sont comparées pour des températures autour de la valeur de T_c de la MCT idéale [15]. Il est intéressant de remarquer que pour la dynamique nous trouvons la plus grande différence entre ces deux tailles de système précisément pour la température T_c. Ce résultat suggère que la dynamique est modifiée qualitativement à la température critique de couplage de mode.

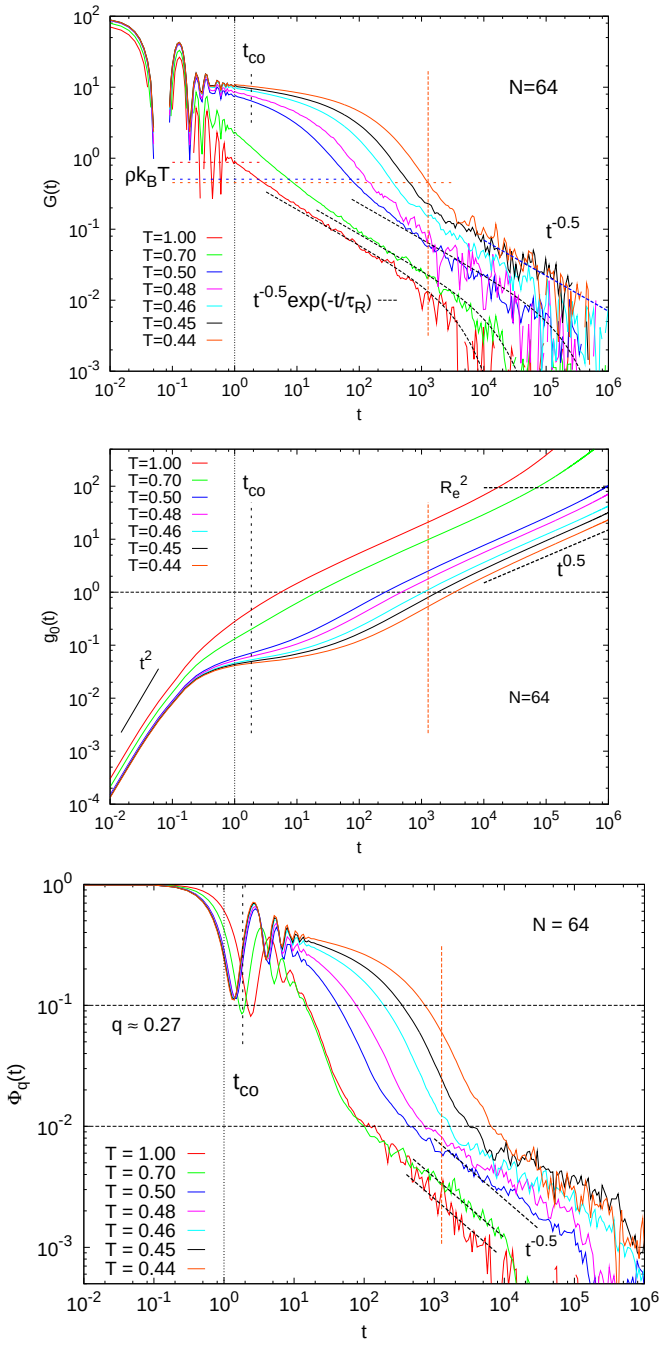

Figure 7: $N = 64$: Haut: fonction de relaxation de cisaillement $G(t)$ en fonction du temps t. Centre: Déplacement quadratique moyen pour tous les monomères $g_0(t)$ en fonction du temps t. Bas: $\phi_{q=q_{\min}}(t)$ en fonction du temps t. $T = 0.44, 0.45, 0.46, 0.48, 0.50, 0.70, 1.00$.

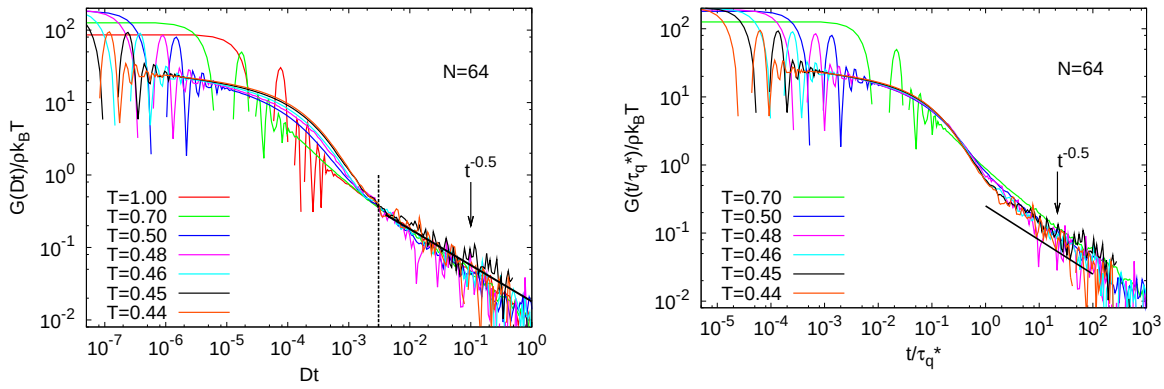

Figure 8: À gauche: $G(t)$ redimensionné par la constante de diffusion D. À droite: $G(t)$ redimensionné par le temps de relaxation τ_{q^*} déterminé par $\phi_{q=6,9}(\tau_{q^*}) = 0.1$.

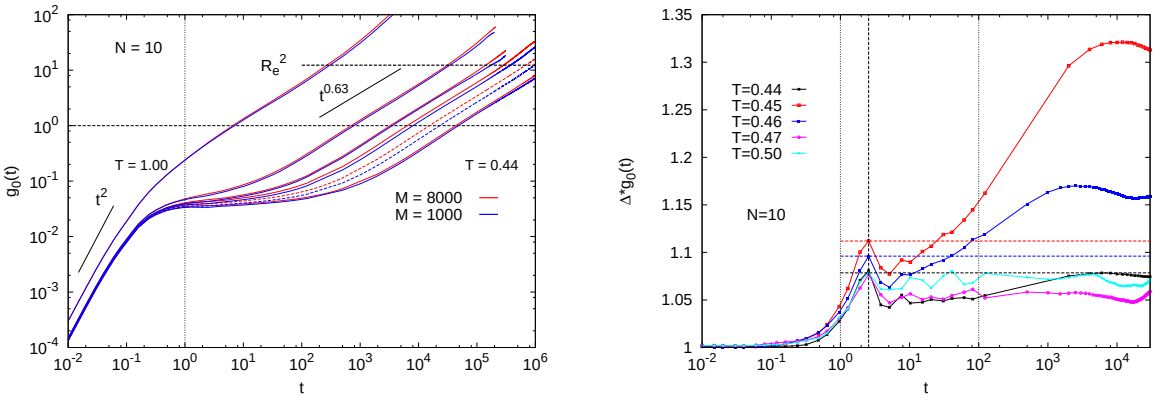

Figure 9: À gauche: Comparaison entre deux tailles de système (M = 1000 et $M = 8000$) à la pression de $p = 1$ et pour une longueur de chaîne de $N = 10$. Déplacement carré moyen $g_0(t)$ pour $T = 1.00, 0.50, 0.47, 0.46, 0.45, 0.44$ (de gauche à droite). $g_0(t)$ pour le système $M = 8000$ est représenté par la courbe rouge et $g_0(t)$ pour $M = 1000$ par la courbe bleue. Le plus petit système montre une dynamique plus lente. $g_0(t)$ pour $T = 0.45$ est représenté en pointillés. Cette température correspond à la température critique de la théorie de couplage de mode idéale. [15]. À droite: Le rapport entre le déplacement quadratique moyen pour les deux tailles de système différent $\Delta^* g_0(t) = \frac{g_{0,M=8000}(t)}{g_{0,M=1000}(t)}$ est représenté pour $T = 0.50, 0.47, 0.46, 0.45, 0.44$. Les lignes horizontales donnent la valeur de $\Delta g_0(t)$ au maximum du premier pic pour $T = 0.45$ (rouge), $T = 0.46$ (bleu) et $T = 0.44$ (noir).

Zusammenfassung

Die Verwendung von Polymeren durchdringt unser tägliches Leben so stark, dass man unser Zeitalter, in Anlehnung an Epochenbegriffe wie z.B. "Steinzeit" oder "Eisenzeit", auch "Polymerzeit" nennen könnte [68]. Der bedeutende Einfluss der Polymerchemie wird offenbar, wenn man an den täglichen Einkauf im Supermarkt denkt: Der Großteil der Verpackungsmaterialien besteht aus Polymeren [44].

Ein einfaches Modell eines Polymers ist eine lange lineare Kette, bestehend aus N miteinander verbundenen elementaren Einheiten [30, 71]. Die erwähnten Verpackungsmaterialien liegen in fester Form vor; meist im glasartigen oder semikristallinen Zustand. Bei ihrer Verarbeitung ist die Kenntnis der viskoelastischen Eigenschaften von Polymerschmelzen unerlässlich [68, 71]. In der Schmelze sind die intermolekularen Wechselwirkungen durch die benachbarten Polymere abgeschirmt, da ein Polymer im Mittel mit $\sqrt{N}$ anderen Polymeren wechselwirkt [24, 26, 68]. Die starke gegenseitige Durchdringung der Ketten führt zu topologischen Hindernissen [24, 26, 56]. Aufgrund dieser sog. Verschlaufungen weisen Polymerschmelzen eine hohe Viskosität auf, da die Dynamik der Ketten stark verlangsamt ist [11].

In der Nähe der Glasübergangstemperatur T_g [53, 61] zeigt die Viskosität von Polymerschmelzen einen dramtischen Anstieg um mehrere Größenordnungen. Dieser gewaltige Anstieg kann bei allen strukturellen Relaxationszeiten beobachtet werden und ist eine spezifische Eigenschaft aller glasbildenden Flüssigkeiten, sowohl polymerartiger als auch nicht polymerartiger. [18, 27]. Im Vergleich zu dieser dramatischen Änderung der Dynamik, ändert sich die Struktur der Schmelze kaum. Das Verstehen des Glasübergangs auf mikrokopischer Ebene ist noch immer eine der größten Herausforderungen der Physik der weichen Materie [7, 17, 25].

Das Ziel dieser Arbeit ist es, ein tieferes Verständnis der Prozesse zu erlangen, welche den Glasübergang von unterkühlten Polymerschmelzen begleiten. Zur Studie werden Computersimulationen von generischen Kugel-Federmodellen [48] verwendet. Hierbei werden die Polymere als flexible Ketten modelliert, wobei auf früheren

Arbeiten aufgebaut wird [4, 15, 22]. Dabei liegt der Fokus auf den dynamischen Eigenschaften der Kette, welche im Rahmen der idealen Modenkopplungstheorie (MCT) untersucht werden [4, 22, 23, 37].

Es wird ein Modell verwendet, welches ähnlich dem von Bennenmann et al. systematisch im unterkühlten Bereich untersuchten Modell ist [12–15]. Dieses wurde anhand von inkohärenten und kohärenten Streufunktionen und Korrelationsfunktionen der Rouse Moden untersucht. Des Weiteren wurden verschiedene Funktionen des mittleren Verschiebungsquadrats betrachtet (vgl. z.B. [11] für eine Übersicht).

In der vorliegenden Arbeit werden speziell kurze (nicht verschlaufte) Ketten untersucht, wie dies durch Ref. [69] nahegelegt wird. In diesem Bereich ist die größte Abhängigkeit der Kettenlänge von T_g zu erwarten. Der Fokus der Arbeit liegt auf der Analyse von Streufunktionen. Hierbei wird der Versuch unternommen, diese für tiefere Temperaturen zu untersuchen, als dies in früheren Arbeiten möglich war [4, 15, 22]. Im weiteren Verlauf der Arbeit wird die Scherrelaxationsfunktion untersucht, die experimentell relevant, allerdings in Computersimulationen mit ausreichender Statistik nur schwer zugänglich ist [52, 54, 75].

Um größere Systeme als Vorgängerarbeiten untersuchen zu können, wird in dieser Arbeit der LAMMPS Code verwendet [49, 67]. Zu Beginn unserer Arbeit wurden die verwendeten Parameter ausgiebig für ein "Bulk"-System mit $N = 10$ und Druck $p = 1$ getestet, wobei es möglich war die Ergebnisse mit denen der Ref. [1–4] zu vergleichen. Für die Untersuchung der oben erwähnten Größen in Abhängigkeit von der Kettenlänge wurde $p = 0$ verwendet. Dadurch können die erhaltenen Daten für "Bulk"-Systeme bei zukünftigen Studien freier Oberflächen als Referenz verwendet werden.

Die statischen Eigenschaften der untersuchten Systeme werden anhand ihrer Dichte, des Kompressionsmoduls, des statischen Strukturfaktors und weiterer Größen analysiert. Hierbei zeigt die Dichte ein Verhalten, das mit der reziproken Kettenlänge skaliert. Dies kann mit Kettenendeffekten plausibel gemacht werden [28].

Die effektive Bindungslänge [79] der Polymerketten wird als Funktion der Temperatur untersucht. Die effektive Bindungslänge nimmt mit sinkender Temperatur ab. Dieses Verhalten kann durch die Modellierung der Polymere als flexible Ketten erklärt werden. Es wäre daher interessant, in der Zukunft chemisch realistischere Modelle (wie z.B. in [16]) zu verwenden.

Die Dynamik wird im Rahmen der idealen MCT [37] analysiert: In Abhängigkeit von der Kettenlänge wird das Temperaturintervall untersucht, in welchem das Zeit-

Temperatur Superpositionsprinzip (TTSP) gültig ist. Ferner bestätigen sich die Vorhersagen das Faktorisierungstheorems im β-Regime. Zusammenfassend scheint das Faktorisierungstheorem noch gültig für Temperaturen zu sein, für welche das TTSP nicht mehr erfüllt ist. Die kritische Modenkopplungstemperatur wird als Funktion der Kettenlänge bestimmt. Sie skaliert — wie die Dichte — mit der reziproken Kettenlänge.

Für die untersuchten Systeme kann die kohärente Streufunktion sehr fein aufgelöst werden, so dass das polymerspezifische Langzeitverhalten beobachtet werden kann. Diese Untersuchung wird durch die Analyse der Scherrelaxationsfunktion [54] erweitert. Es zeigt sich, dass beim Abkühlen die Monomerrelaxationszeiten zunehmen. Dadurch werden Relaxationsprozesse auf Längenskalen der Polymere zu späteren Zeiten verschoben.

Im letzten Teil der Arbeit werden in einer Fallstudie die Effekte der endlichen Simulationsbox auf die Dynamik untersucht (vgl. z.B. [45]). Für zwei verschiedene Boxgrößen werden Unterschiede in der Dynamik, gemessen durch die kohärente Streufunktion und das mittlere Verschiebungsquadrat der Monomere, beobachtet. Interessanterweise sind die Unterschiede für die kritische Modenkopplungstemperatur [15] am größten. In einer zukünftigen Studie könnten diese Ergebnisse durch die Untersuchung noch größerer Systeme weiter untermauert werden. In diesem Fall könnte man folgendes schließen: Auch wenn bei der kritischen Modenkopplungstemperatur kein dynamischer Stillstand beobachtet werden kann, so ändert sich hier die Dynamik doch qualitativ.

Chapter 1

Introduction

The usage of polymers influences a wide range of our everyday life so that our age could be, without exaggeration, termed the Polymer Age [68]. The impact of the development of polymer chemistry might become quite apparent by considering modern supermarket culture: Most packing materials are made of polymer solids [44]. The simplest example of polymers are long linear chains of N linked elementary units [30, 71]. The mentioned packaging materials are present in solid form, mostly in the glassy or the semi-crystalline state. For the processing it is important to understand the viscoelastic properties of polymer melts [68, 71].

The constituents of a polymer are named monomers and have a typical size of ~ 0.5 nm . In the melt they are densely packed and exhibit no long range order [11]. Upon cooling this overall structure changes only slightly, a property which is also familiar from supercooled simple liquids [17, 20]. They are much smaller than the polymer that they form. The size of a polymer could be measured, for example by the radius of gyration R_g [26, 39, 71], which is accessible in experiments by methods of light or neutron scattering [46] and ranges from 10 nm to 100 nm [11].

On large length scales polymers exhibit a self-similar structure which allows to treat them theoretically as fractals [24, 68]. In a polymer melt intermolecular interactions are screened by neighboring polymers as a polymer interacts, on average, with $\sqrt{N}$ other chains [24, 26, 68]. The fact that the chains penetrate each other so massively results in topological constraints [24, 26, 56]. The entanglements lead to a high viscosity due to the great slowing down of the chain dynamics [11].

On approaching the glass transition temperature T_{g} [53, 61] polymer melts show a remarkable increase of their viscosity by many orders of magnitude. This enormous increase is observed for all structural relaxation times and is a typical feature of all

glass-forming liquids, polymeric and non-polymeric ones [18, 27].

In comparison to this dramatic change of the dynamics, the structure varies only slightly. A microscopic understanding of the glass transition remains one of the biggest challenges in condensed matter physics [7, 17, 25].

Aim of this study. The aim of this study is to gain a deeper insight into the processes which are involved in the phenomenon of glassy slowing down in supercooled polymer melts. We approach this problem by computer simulation using a generic bead-spring model [48] in which polymers are modeled as flexible chains. The present study builds upon previous work [4, 15, 22]. Here we especially focus on the chain length dependence of the dynamical properties of the melt, which are mainly analysed in the framework of the ideal mode-coupling theory [4, 22, 23, 37].

We employ a simulation model very similar to the bead-spring polymer model first studied systematically in the supercooled regime by Bennemann et al. [12–15]. It was analysed in terms of the incoherent and coherent scattering functions, Rouse mode correlation function, and various mean-square displacements (see e.g. [11] for a review). In parallel, the model has also been employed to study thin confined films [11] as well as supported and free standing thin polymer films [64, 65], and also the influence of solvent particles [66]. The work on supported and free standing films was performed at a pressure $p = 0$ which is the more natural choice when simulating free surfaces. We mainly employ the same pressure in our simulation.

Thereby especially small (nonentangled) chains are explored, as it is suggested by [69] that in this range the largest dependence of the chain length of T_{g} can be expected. This analysis mainly focuses on intermediate scattering functions by trying to achieve lower temperatures than it was possible in previous works [4, 15, 22]. As an additional quantity we study the shear relaxation function which is experimentally relevant, but difficult to determine with satisfying statistics in computer simulations [52, 54, 75].

The previous works have been performed with home-written sequential MD codes. To be able to study larger systems and to make use of today's parallel computer architectures, we decided to work with the LAMMPS code [49, 67]. In a first part of our work, we tested our implementation of the parameters with the bulk system $N = 10$ at $p = 1$ where it was possible to compare with the data of Ref. [1–4]. Then we chose to perform a systematic chain length variation in the main part at a lower pressure $p = 0$ so that our bulk data can serve as a reference for future work with

free surfaces.

Outline. This work is organised as follows: In the second chapter we describe the simulation methodology by shortly summarizing the used simulation technique and the employed simulation model. The third chapter deals with the static properties of the studied systems. In the forth and fifth chapter we turn to the dynamic properties. In the forth chapter the dynamics is studied in the framework of the ideal mode-coupling theory, whereas in the fifth chapter the dynamics is analysed by employing the shear relaxation function. Additionally, we undertake a case study on the finite size effects. The work finishes with a summary.

Chapter 2

Simulation

In this work we want to study the viscoelastic properties of glass-forming polymer melts. For this purpose we make use of computer simulations. In this chapter we want to answer the following questions: What is the appropriate simulation method to investigate the properties of glass-forming polyer melts? Which are the essential ingredients of a computer simulation?

2.1 Introduction

We want to use computer simulations to generate microscopic information of a physical system [5, 31]. Statistical mechanics provides us then with a tool to convert this microscopic information into macroscopic information of the studied system.

There are different approaches to simulate polymers [11]: the atomistic method and the coarse-grained method. The coarse-grained method captures the less details about the considered physical system. Atomistic models employ potentials for interactions between all atoms of the model. The form of these potentials (which account for example for the bond length, bond angles, ...) is assumed and related parameters are estimated by experiments and quantum chemical calculations: For the explicit atom model the constituents are the individual atoms of the system. In the case of the united atom model spherical sites comprising several atoms are the constituents. The coarse-grained method applies stronger approximations to the considered physical system. Groups of atoms as for example monomers are modelled by spherical interaction sites and realistic potentials are replaced by even simpler ones.

Although it is desirable to take into account the most details possible about the

system, the atomistic approach is often not feasible as it is too demanding in terms of CPU time [11]. Therefore we employ coarse-grained models in our work as this provides the possibility to simulate systems which are in a temperature region which is close to the glass transition temperature [53]. In addition, by reducing the number of different interactions, we concentrate on generic features.

2.2 MD simulations

Our short summary about molecular dynamics simulation mainly follows [5, 31]. An **MD** simulation consists of three steps:

Initialization First a configuration is generated consistent with the physical conditions of the considered system. By the term "configuration" we understand the collection of all data characterizing unambiguously the microscopic state of a physical system. During this initialization process positions and velocities of all particles are chosen such that they are compatible with the structure which is to be simulated. For example: If a system with excluded volume is simulated, distances between initial particle positions must not be so small that the particles penetrate each other. Our procedure will be explained in detail in section 2.5.

Computation of forces Next comes the computation of forces: When all particle positions are known, forces have to be calculated. The interactions between particles are described in terms of interaction potentials [5, 31]:

$$-\frac{\partial}{\partial \mathbf{r}_i} U(\mathbf{r}^M) = \mathbf{F}_i \ . \tag{2.1}$$

From all particle positions (denoted in Eq. (2.1) by $\mathbf{r}^M$) together with the interaction potential U the resulting force $\mathbf{F}_i$ acting on particle i can be computed. The potentials of pairwise interactions between particles are assumed to be additive so that the total sum of them gives the interaction potential U. In this equation, $\mathbf{r}_i$ denotes the position of particle i; so the derivative of $U(\mathbf{r}^M)$ with respect to the particle's position gives the force acting on it. Therefore the computation of all forces acting in the system is done by evaluating all derivatives with respect to all particles' positions.

Integration of Newton's equations of motion In a third step, the time evolution of the microscopic state of the system is calculated. This means that the positions and velocities of all particles are evaluated. This is achieved by integration of Newton's equations of motion:

$$\mathbf{F}_i(t) = m_i \frac{\mathrm{d}^2\mathbf{r}_i(t)}{\mathrm{d}t^2} \tag{2.2}$$

with m_i being the mass of particle i.[1]

This integration is done by time discretization. The discrete time intervals are called integration time steps. As a result one can only access information about the position and velocity of a certain particle for discrete points on the timeline. There are various algorithms to do this (see section 2.2.1). Each entity of positions and velocities of all particles gives one configuration.

The iteration of the last two steps represents the main core of an **MD** simulation. Following this scheme, after each integration time step positions and velocities of all particles are computed and a new configuration is generated. A set of sequential configurations forms a trajectory and provides information about the time evolution of the microscopic states of the considered system. The computation of forces and the integration of Newton's equation of motion are repeated until the trajectory has reached "sufficient" length. In other words, enough configurations are generated so that the studied property of the system is measurable with sufficient statistics. From a statistical point of view, we could say: The subset of the phase space probed by the simulation is large enough to draw conclusions about the physical behavior of the studied system [5].

Besides the underlying assumptions about the physical systems, which are incorporated in an **MD** simulation (like the assumption that the potential is pairwise additive), there are other sources of imprecisions [5]. After the forces are calculated, particles are moved during an integration time step according to the force acting on them and their initial velocity. Yet, the force changes permanently while a particle changes its positions and / or other particles change their position and thereby the interaction potential is changed. Therefore, an error will occur and it will grow with increasing integration time step. So, the integration time step should be chosen as small as possible. On the other hand, one is interested in generating sequential

[1] We consider only systems where all particles have the same mass, so $m_i \equiv m$ for all particles.

configurations, which cover the phase space as much as possible. This means that the configurations should not just differ in tiny changes of the particles' positions but rather particles should travel longer distances and thus scanning a larger part of the phase space. This is important, as every computation of positions and forces cost CPU time and this will eventually decide if a simulation is feasible or not. For this reason one has to find a compromise between these two demands to the size of the integration time step.

The computation of forces is the most time consuming part, which is necessary to generate configurations [31]. An effective way to reduce the needed computation time is to consider as little as possible interaction partners in this computation. The interaction potential is put together of pairwise additive potentials, and therefore the single parts of the potential can be treated separately. The larger the distance between particles is, the smaller the interaction between them. Thus, at some distance the interaction between two particles will be so small that it could be neglected compared to interactions exerted on them by closer particles.[2] One exploits this fact by introducing an arbitrary distance, which is called the cut-off radius. Particles that are separated by a distance larger than the cut-off radius do not interact with each other [5, 31]. The benefit of this is the following: When the forces acting on a particle are computed, particles that are farer apart than the cut-off radius do not have to be considered. This saves a lot of computational time as only a small fraction of all particles has to be considered in the force computation.

2.2.1 Integration algorithms

As an example for an algorithm to integrate Newton's equation of motion we show the Verlet algorithm [74]. This algorithm is the most basic one (and often the best one) [31]:

We consider the Taylor expansion of the coordinate of a particle for $t+\Delta t$, around t,

$$r(t+\Delta t) = r(t) + \frac{1}{1!}v(t)\Delta t + \frac{1}{2!}\frac{f(t)}{m}\Delta t^2 + \frac{1}{3!}\dddot{r}\Delta t^3 + \mathcal{O}(\Delta t^4)\ , \qquad (2.3)$$

[2] This procedure is strictly speaking only possible if no long range interactions are present. For our model the long range interactions become negligible for distances of $r \approx 2r_{\min}$, where $r_{\min}$ denotes the minimum of the Lennard-Jones potential.

and similarly for $t - \Delta t$, around t,

$$r(t - \Delta t) = r(t) - \frac{1}{1!}v(t)\Delta t + \frac{1}{2!}\frac{f(t)}{m}\Delta t^2 - \frac{1}{3!}\dddot{r}\Delta t^3 + \mathcal{O}(\Delta t^4) \ . \tag{2.4}$$

By summing up these equations (Eq. (2.3) and Eq. (2.4)) we get

$$r(t + \Delta t) + r(t - \Delta t) = 2r(t) + \frac{f(t)}{m}\Delta t^2 + \mathcal{O}(\Delta t^4) \ , \tag{2.5}$$

which can be rewritten as

$$r(t + \Delta t) \approx 2r(t) - r(t - \Delta t) + \frac{f(t)}{m}\Delta t^2 \ . \tag{2.6}$$

As it can be seen in Eq. (2.6) the Verlet algorithm does not make use of the velocities to update the positions of the system, and the integration error is only of the 4th order in Δt [31].

The velocity Verlet algorithm The velocity Verlet algorithm [72] is a variation of the Verlet algorithm, which uses velocities and positions evaluated for the same time. As this algorithm is implemented in the simulation code [49, 67] that we use (see section 2.5), we will describe it here as an additional example for an integration algorithm. Similar to the Verlet algorithm positions are computed using a Taylor expansion [31]:

$$r(t + \Delta t) = r(t) + v(t)\Delta t + \frac{1}{2}\frac{f(t)}{m}\Delta t^2 \ . \tag{2.7}$$

The extension of the velocity Verlet algorithm is based on the use of velocities. Velocities are updated by obeying the following scheme

$$v(t + \Delta t) = v(t) + \frac{f(t + \Delta t) + f(t)}{2m}\Delta t \ . \tag{2.8}$$

We point to the fact that first positions and from these forces have to be evaluated, before velocities can be computed (cf. Eq. (2.8)). It can be shown that the velocity Verlet algorithm is equivalent to the Verlet algorithm [31].

2.3 Simulations in different ensembles

By employing the simulation methods described so far we are able to simulate systems whose total energy E does not change with time. The introduced algorithm, which is built upon Newton's equations of motion, conserves the total energy of the

system. In the beginning of a simulation, we fix the number of particles and the volume of the system, that means we choose a specific simulation box geometry and size. This implies that the thermodynamic variables N, V, E are fixed and therefore we generate configurations in the micro canonical (NVE) ensemble [5, 31]. This method generates trajectories with realistic dynamics, the only draw back is, that the integration time step has to be chosen so small that it is guaranteed that the total energy does not change due to numerical errors. Another reason why other ensembles than the NVE ensemble are employed is that one is interested in simulating a system that mimics better the experimental situation.

In an experiment one usually controls temperature and external pressure as it is normally the easiest way of setting up a system to control these thermodynamical variables (T and p). Thermodynamical variables like temperature and pressure which do not scale with the system size are called intensive variable — opposite to extensive variables which scale with the system size, like energy E, volume V, entropy S, ... Controlling intensive variables can be easily achieved by bringing the system under consideration in contact with a much larger system. For example, temperature can be controlled by establishing thermal contact between the considered system and a much larger system which is called a "heat bath" [70].

Motivated by these facts we should answer the following question: How can this situation be realized in a simulation? Or more precisely: How can we control temperature T and pressure p in a simulation?

2.3.1 Thermostatting

Similarly to the experimental situation one could simulate the considered system being in contact with a larger system. This could be realized by simulating a large system of which the considered system is a subsystem. Eventually one would have to take care about a lot of degrees of freedom which in most cases is not feasible.

A way around this problem was proposed by Hoover [41]: By extending previous work from Andersen [6] and Nosé [62, 63] he came up with following equations [64, 73]:

$$\dot{\mathbf{r}}_i = \frac{\mathbf{p}_i}{m_i} , \tag{2.9}$$

$$\dot{\mathbf{p}}_i = \mathbf{F}_i - \xi \mathbf{p}_i , \tag{2.10}$$

$$\dot{\xi} = \frac{1}{Q}\Big(\sum_i \frac{\mathbf{p}_i^2}{m_i} - 3Nk_{\mathrm{B}}T_{\mathrm{ext}} \Big) , \tag{2.11}$$

with T_{ext} denoting the set external temperature.

Broadly speaking, in Hoover's approach all degrees of freedom of the heat bath are taken into account by just one degree of freedom. The heat bath accelerates or slows down particles depending on the mean kinetic energy.

The main modification of the Newtonian equations of motion is to introduce an additional term in Eq. (2.10). The additional term $-\xi \mathbf{p}_i$ acts as a dissipative part if ξ is positive, and accelerates particles if $\xi < 0$. It changes opposite to the mean kinetic energy: If the main kinetic energy is high it decreases it (by slowing down the particles) and vice versa. The time evolution of ξ (Eq. (2.11)) is coupled to the mean kinetic energy with Q being the coupling constant. Q sets the strength of the contact to the heat bath (Eq. (2.11)) and can also be regarded as the thermal inertia of the system. As the value of the friction variable ξ is given by a differential equation the thermostat acts smoothly on the whole system.

We employ this thermostat in production runs (see section 2.5.3). There we generate trajectories (see section 2.2) within the NVT ensemble [5, 31]. That means that the number of particles of the system N, the volume V and the temperature T is fixed. N and V are fixed by choosing an appropriate value for the number of particles and the simulation box size. T is set by using the Nosé-Hoover thermostat.

2.3.2 Barostatting

A barostat can be realized in a similar way as a thermostat. Here again the large number of degrees of freedom of the larger system is taken into account by just one variable that controls the pressure evolution. The time evolution of this variable is connected to the difference between the current and the chosen value of the pressure p. This is a similar approach as the one used for the Nosé-Hoover thermostat.

In the following we present the equations describing this approach in the formulation of Melchionna et al. [57]. In this way the barostat is implemented in the source

code [49, 67] that we use (see section 2.5) [73]:

$$\dot{\mathbf{r}}_i = \frac{\mathbf{p}_i}{m_i} + \eta(\mathbf{r}_i - \mathbf{R}_{\mathrm{cm}}) \,, \tag{2.12}$$

$$\dot{\mathbf{p}}_i = \mathbf{F}_i - (\xi + \eta)\mathbf{p}_i \,, \tag{2.13}$$

$$\dot{\xi} = \frac{1}{Q}\Big(\sum_i \frac{\mathbf{p}_i^2}{m_i} - 3Nk_{\mathrm{B}}T_{\mathrm{ext}}\Big) \,, \tag{2.14}$$

$$\dot{\eta} = \frac{V}{M}(p(t) - p_{\mathrm{ext}}) \,, \tag{2.15}$$

$$\dot{V} = 3V\eta \,, \tag{2.16}$$

where $p(t)$ denotes the instant pressure and p_{ext} the set external pressure. M[3] controls the coupling of η to the pressure difference $p(t) - p_{\mathrm{ext}}$ along with V.

By contrasting this set of equations with the one of the Nosé-Hoover thermostat we find the following differences and similarities: The time evolution of the volume is characterized by Eq. (2.16): Depending on η the volume evolves, but the time evolution of η itself depends on V and the difference of p and p_{ext}. η can be positive or negative and shows fluctuations around 0 in analogy to ξ. So — as in the case of the Nosé-Hoover thermostat — we have a set of coupled differential equations (Eq. (2.15) and Eq. (2.16)) which govern the time evolution of the volume. The equation (Eq. (2.14)) controlling the temperature dynamics of the system is left unchanged. Equation (2.10) is changed to Eq. (2.13) by adding the extra term $\eta\mathbf{p}_i$. The additional term in Eq. (2.12), $\eta(\mathbf{r}_i - \mathbf{R}_{\mathrm{cm}})$, where $\mathbf{R}_{\mathrm{cm}}$ denotes the center of mass position, guarantees that the NpT ensemble is realized [73].

Applying this simulation scheme generates configurations within the NpT ensemble as these thermodynamical variables are kept fixed [5, 31]. We will employ this method in equilibrating our system (see section 2.5.2).

2.4 Simulation model

In this work, we study the behavior of glass-forming polymer melts close to the glass transition. So we have to employ a model which features polymer properties and shows a glass transition when cooled to low enough temperatures. We model the chemical interactions of these polymers by interactions of spherical interaction sites. The interactions are described by simplified empirical potentials [11]. A defined

[3] The choice of M depends on the ratio between the time scale for volume fluctuations and the time it takes for a sound wave to travel through the simulation box [73].

number of these interaction sites — we will refer to them in the following just as beads — make up a chain which models an individual polymer. These kind of models are referred to as bead-spring models [48].

We use a bead-spring model for flexible chains. By flexible chains we understand that chains are only hindered from back folding by the excluded volume. This kind of model is among of the most simplest models which still captures the basic features of polymers: chain connectivity and excluded volume [11].

In this model chain connectivity is induced via a harmonic potential, which is effective between consecutive bonded monomers [65]:

$$U_{\mathrm{b}}(l) = \frac{1}{2} k_{\mathrm{b}} (l - l_0)^2 \,, \tag{2.17}$$

where $l_0 = 0.967\sigma_{\mathrm{LJ}}$ specifies the equilibrium bond length, $k_{\mathrm{b}} = 1110\frac{\epsilon_{\mathrm{LJ}}}{\sigma_{\mathrm{LJ}}^2}$ is the force constant and l denotes the distances between two bonded monomers.

Monomers of different chains and monomers which belong to the same chain but are not directly bonded interact by a Lennard-Jones potential. This potential is truncated and shifted by a constant $C = 0.02684\epsilon_{\mathrm{LJ}}$, so that, at the cutoff $r_{\mathrm{cut}} = 2.3\sigma_{\mathrm{LJ}} \approx 2r_{\mathrm{min}}$[4], the potential vanishes continuously

$$U_{\mathrm{LJ}}(r) = \begin{cases} 4\epsilon_{\mathrm{LJ}}\left[\left(\frac{\sigma_{\mathrm{LJ}}}{r}\right)^{12} - \left(\frac{\sigma_{\mathrm{LJ}}}{r}\right)^{6}\right] + C & \text{for } r < r_{\mathrm{cut}} \,, \\ 0 & \text{else.} \end{cases} \tag{2.18}$$

For small r ($r \ll \sigma_{\mathrm{LJ}}$) Eq. (2.18) shows a sharp increase of its value and will finally diverge for $r \to 0$. This divergence mimics the excluded volume.

Lennard Jones units In the following all quantities are given in Lennard-Jones units [5, 11]: distance is measured in units of σ_{LJ}, temperatures in $\epsilon_{\mathrm{LJ}}/k_{\mathrm{B}}$, and time in $\tau_{\mathrm{LJ}} = (m\sigma_{\mathrm{LJ}}^2/\epsilon_{\mathrm{LJ}})^{1/2}$, where the Boltzmann constant and the monomer mass are given by $k_{\mathrm{B}} = m = 1$.

2.5 Set up of simulations

Using the flexible chain model described in section 2.4 we simulate various systems consisting of different chain lengths N (monomers per chain) and system sizes. Additionally, we employ two different pressure values: $p = 0$ and $p = 1$. We started

[4] The minimum of the LJ potential is given by $r_{\mathrm{min}} = 2^{\frac{1}{6}}\sigma_{\mathrm{LJ}}$.

simulating systems for $p = 1$ and $N = 10$, as many data for this pressure and chain length exist, especially for low temperatures [4, 22]. Thereby we tested our employed simulation algorithm by comparing static and dynamical data. Then we proceeded to $p = 0$ where we set up different chain lengths (see Table 2.1 for an overview of the simulated systems and Table A.1 for the used simulation parameters).

To generate simulation data we employ the open-source code "Large-scale Atomic/ Molecular Massively Parallel Simulator" (**LAMMPS**) [49, 67]. This has two advantages: Firstly, this code is widely used for simulations of large systems and therefore well tested. Secondly this code is parallelized and hence well adapted for today's computer architectures.

The generation of simulation data — which provide microscopic information of the simulated system — is divided into three steps: In the first step, the simulation is set up which means that basic conditions of the simulation are fixed: size of simulation (number of objects which are to be simulated; simulation box size; boundary conditions (e.g. periodic boundary conditions); ...) and an initial configuration of the system is generated which is in accordance with the physical conditions of the considered system [5, 31] (see section 2.5.1).

In a second step the initial configuration is equilibrated which means that it is transferred to a state of minimum free energy (see section 2.5.2). This is done in the NpT ensemble. Equilibrated configurations are cooled in a subsequent step to lower temperatures in such a way that the system is not trapped in local minima of the free energy. Afterwards the so obtained configurations are equilibrated again.

In a last step, equilibrated configurations produced during the last steps are used as a starting configuration from which the actual production runs are started (see section 2.5.3).

In the course of our work we analyse mostly quantities which are calculated in the reciprocal space (e.g. coherent intermediate scattering functions). Therefore a fixed simulation box size will be convenient for subsequent calculations. For the sake of comparability with experiments a fixed pressure is desirable. These two requirements can be fulfilled by the following implementation of the simulation procedure:

2.5.1 Initial configuration

In the following we shortly summarize how an initial configuration can be set up. In the beginning, chains are generated as random walks with an angular bias without

monomers / chain	chains	pressure
10	800	1
10	100	1
64	192	0
32	384	0
16	768	0
8	1536	0
4	3072	0

Table 2.1: Overview of simulated systems. Pressure is given in LJ-units. A harmonic bond potential and cut-off radius of $r_{\text{cut}} = 2.3\sigma_{\text{LJ}}$ is used for every system.

excluded volume. These chains are randomly distributed in the simulation box. Then a soft potential between the monomers is introduced and the monomers are propagated with Langevin dynamics. The random distribution of the chains is likely to generate overlap of some particles. To avoid diverging forces, a force-cap parameter is introduced to limit the maximum possible forces. This amounts to a modified (soft) pair-potential with a linearly decreasing term for small distances. In addition, the velocities are rescaled regularly to effeciently dissipate energy coming from strong initial overlap. Then, the soft potential is increased little by little to push still overlapping monomers apart from each other until the real potential is reached. In the end, a configuration is generated that can be used in a subsequent equilibration run. We have to state that there is no exact procedure to generate an initial configuration. The generated configuration has to be tested for possible local potential energy maxima. As a first test the bond length distribution can be checked. Note that our procedure is quite similar to the one described by Auhl et al. [8]. As our chains are still rather short, no additional Monte Carlo moves are necessary to accelerate equilibration, at least at high temperature. All configurations at lower temperatures are derived by the procedure described in the following section.

2.5.2 Equilibration run

The initial configuration is then equilibrated. The pressure and the temperature are set by using a barostat and thermostat as described in section 2.3.2. During the equilibration run the system has to be given the possibility to develop a volume which

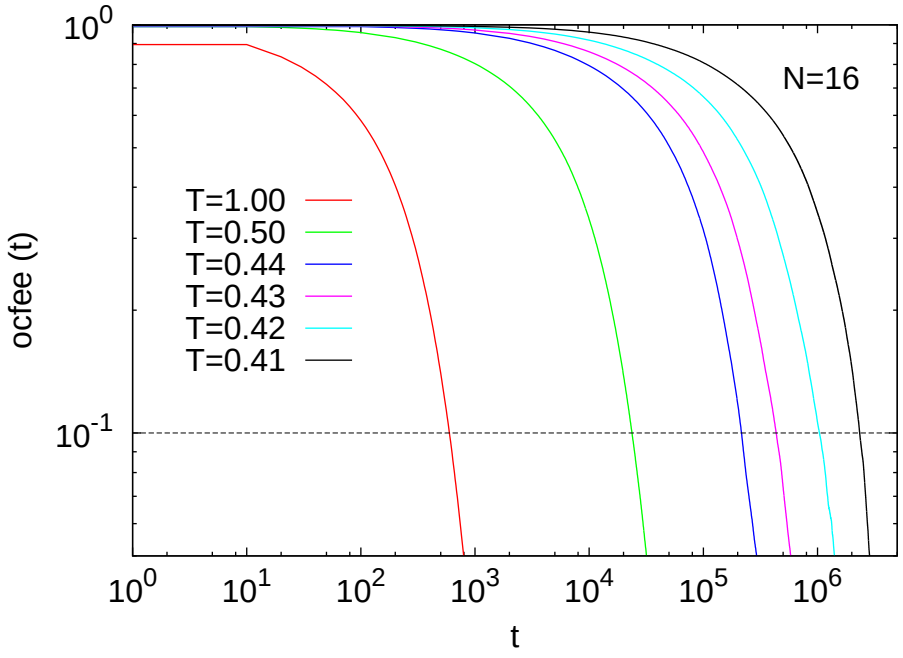

Figure 2.1: Orientational correlation function of the end-to-end vector for $N = 16$ and $T = 1, 0.5, 0.44, 0.43, 0.42, 0.41$.

is in accordance with the applied pressure. This can be achieved by propagating the initial configuration within the NpT-ensemble.

As a criterion for the level of equilibration we take the orientational correlation function of the end-to-end-vector [26], $\phi_{\mathrm{e}}(t)$, of every polymer chain averaged over all chains of the system

$$\phi_{\mathrm{e}}(t) = \frac{\langle \mathbf{R}_{\mathrm{e}}(t)\mathbf{R}_{\mathrm{e}}(0)\rangle}{\langle \mathbf{R}_{\mathrm{e}}^2(0)\rangle} , \tag{2.19}$$

where $\mathbf{R}_{\mathrm{e}}$ denotes the end-to-end vector (see section 3.5). When this averaged value of the polymer melt is about 0.1 ($\phi_{\mathrm{e}}(t) \lesssim 0.1$), we consider the system is adequately equilibrated (cf. Fig. 2.1), as $\phi_{\mathrm{e}}(t)$ measures the slowest relaxation process in terms of the chains [58]. (See Table A.2 and Table A.3 for a survey of the relaxation times.)

The initial configuration is equilibrated at $T = 1$, as this temperature is high compared to the glass transition temperature T_{g}, $1 \gtrsim 2T_{\mathrm{g}}$. In order to cool to lower temperatures without having the system getting trapped in a local free energy minimum we gradually decrease the temperature of the system so slowly that there is enough time for it to relax on all length scales in terms of the polymer chains.

To this end, we follow a cooling protocol which consists of two parts: In a first

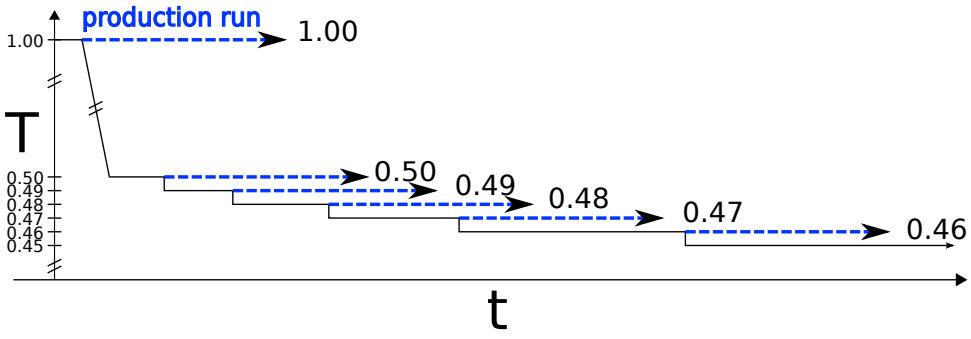

Figure 2.2: Schematic representation of the cooling process. Black lines indicate the cooling and equilibration procedure. Blue arrows indicate subsequent production runs.

part, the system is gradually cooled down towards a temperature of $T = 0.50$ (cf. Fig. 2.2). In the temperature interval of $0.5 \leqslant T \leqslant 1.0$ we can gradually cool our system without incurring the risk that it will get trapped in a local free energy minimum by choosing a slow enough cooling rate [58]. (Parts of the system which might not totally relax due to this schedule are given enough time to fully relax in a subsequent equilibration run at constant temperature.)

The cooling schedule is given by:

$$T(t) = T_{\text{start}} - \Gamma_T t \tag{2.20}$$

with T_{start} denoting the start temperature which is set to 1 for all simulations and Γ_T the cooling rate. For all systems the cooling rate Γ_T is given by $\Gamma_T = 10^{-5}$.

In the temperature interval below $T = 0.50$ we employ a different cooling schedule: We take configurations from equilibrated systems and set up the next equilibration run with a temperature that is instantaneously lowered by $\Delta T = 0.01$. In a subsequent equilibration run the system is given enough time to relax on all length scales in terms of the polymer chains [5]. When the criterion $\phi_{\text{e}}(t) \lesssim 0.1$ [6] is fulfilled we lower the temperature again and start the next equilibration run. By repeating this procedure we are able to lower the temperature of the system step by step without incurring the risk that it will get finally trapped in a local free energy minimum.

[5] Due to the procedure we employ for temperatures $T \leq 0.5$, the used cooling rates are in the order of $\Gamma_T \propto 10^{-8}$ or slower. These cooling rates are calculated by $\frac{\Delta T}{\Delta t}$ as in Ref. [19]. Compared to the slowest cooling rate that is used in this reference, we use cooling rates that are at least two orders of magnitude slower.

[6] For chain lengths with $N > 10$, not the orientational correlation function of the end-to-end-vector is considered but the orientational correlation function of a subsegment of $N = 10$.

2.5.3 Production run

A production run denotes a simulation run which generates the data that we analyze to broaden our knowledge about glass forming polymer melts. To set up a production run we take an equilibrated configuration (we take a configuration from the end of an equilibration run). Then - during a small preceding run - the simulation box size is smoothly adapted to the determined average volume of the equilibration run from which the end configuration was taken. This is achieved by changing the box length in all dimensions slowly with time.

In **LAMMPS** [49, 67] this is achieved by employing the "deform" command [50]. By using this command the box size of the taken configuration (described above) is continuatiously (every 10 (τ_{LJ})) changed over a time interval of $5,000$ (τ_{LJ}) so that it will finally reach the determined average volume. We have to employ this procedure as the volume during an equilibration run slightly fluctuates. Therefore the volume of the used end configuration can slightly differ from the average volume of the whole equilibration run.

When the average volume of the equilibration run is reached the actual production run is started. The configurations are propagated in the NVT ensemble where a thermostat is used (cf. section 2.3.1).

We want the simulation algorithm to have as little influence as possible on the results. For this reason we choose the NVT ensemble for the production run. (In the NVT ensemble we only employ a thermostat which enables us to choose a larger integration time step compared to an NVE ensemble simulation. In an NpT ensemble simulation pressure and temperature are influenced by the simulation algorithm. Thus, the influence on the results within an NpT ensemble simulation is larger, which is not desirable.)

Chapter 3

Static properties

In this chapter we analyze the static properties of our model system. This will also provide us with a foundation for a better understanding of the system's dynamics later on. First we will discuss the density as a function of the chain length and then we proceed with the bulk modulus and the high-frequency shear modulus. Thereafter we introduce the static structure factor and the radial distribution function. Finally we turn to polymer-specific quantities where we introduce the end-to-end vector and investigate the chain conformation via the internal distances along the chain backbone.

The systems that we are dealing with are glass-forming polymer melts. A polymer melt can be defined as a dense polymer system without solvent molecules [26]. The specification "glass-forming" points to the fact that these polymer melts will form a glass when the temperature is sufficiently decreased. Crystallization is effectively prevented by two properties [4]: Firstly, the bond length l_0 and the minimum of the Lennard-Jones potential $r_{\min}$ slightly differ, so l_0 is not compatible with $r_{\min}$. Secondly, we employ a totally flexible model. Theses two points result in local distortion of the regular arrangement which impedes crystallization when the melt is cooled from high temperatures. (However, the choice of the Lennard-Jones and the bond potential does not preclude crystallization [19, 59, 60]).

The application of a totally flexible model limits the possible manners which could lead to a glass transition. In our model the glass transition is only driven by the temperature dependent closer packing of the monomers. In more realistic chemical models the freezing of intramolecular modes provides an additional way (see e.g. [16]). This results in higher glass transition temperatures.

monomers / chain N	chains n	monomers Nn	pressure p
64	192	12288	0
32	384	12288	0
16	768	12288	0
8	1536	12288	0
4	3072	12288	0

Table 3.1: Overview of systems simulated with a pressure of $p = 0$.

3.1 Density

We set up systems with different chain length N in order to analyse the influence of the chain length on the structural and dynamical properties of polymer melts. These systems consist of 12288 monomers and are simulated at a pressure of $p = 0$. (As described in section 2.5.2 during an NpT run a pressure of $p = 0$ is imposed on the system using a barostat. After the equilibration the resulting volume of this simulation is determined and used to set up a subsequent NVT simulation.)

More precisely, we simulated 5 different chain lengths of $N = 64, 32, 16, 8, 4$. In the beginning, we have equilibrated the systems for $N = 64$. Shorter N are generated by cutting these chains at $T \geq 0.5$. For lower temperatures, the cooling protocol explained in section 2.5.2 has been applied to each chain length individually. These systems also differ in the total number of chains n, as the total number of monomers is fixed. For an overview of these systems see Table 3.1.

An essential feature of polymer melts is their high density. In the following, we will study how the density is connected to the chain length. The density ρ is given by

$$\rho = \frac{N\, n}{V}\,, \tag{3.1}$$

where V denotes the volume of the simulation box.

Figure 3.1 shows the density of these systems as a function of temperature T. The comparison of the densities for different chain length at a fixed temperature of $T = 0.50$ infers that the density increases with chain length. An argument for this observation can be found in the different distances between bonded monomers and non-bonded monomers [28]. The average distance between bonded monomers is given by the equilibrium bond length $l_0 = 0.967$. In contrast to this the average distance between monomers, that are not bonded, is set by the minimum of the

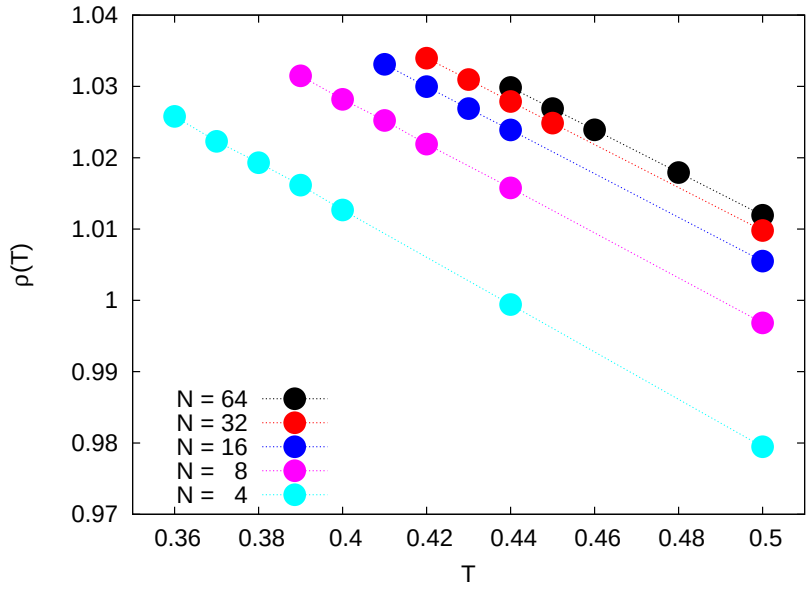

Figure 3.1: Main figure: Density ρ as a function of temperature T for chain length $N = 64, 32, 16, 8, 4$. (See Table A.4 for the numerical values.)

Lennard-Jones potential which is given by $r_{\min} = 2^{1/6}\sigma_{\mathrm{LJ}}$. Therefore the volume occupied by bonded monomers within a chain compared to the volume that is occupied by the end monomers, the outermost monomers, differ. See Fig. 3.2 for a schematic representation of this chain end effect.

Therefore — in a first approximation — the volume that a chain occupies can be split into two contributions. The volume occupied by the inner monomers and the volume occupied by the end monomers. The end monomers occupy a larger volume as they have only one binding partner in contrast to the inner monomers. This can be expressed by the following equations:

$$V_{\mathrm{chain}} = NV_{\mathrm{inner}} + 2[V_{\mathrm{end}} - V_{\mathrm{inner}}] \,, \tag{3.2}$$

$$V_{\mathrm{chain}} = NV_{\mathrm{inner}}\big[1 + \frac{2\Delta V_{\mathrm{e}}}{NV_{\mathrm{inner}}}\big] \,, \tag{3.3}$$

with V_{chain} denoting the volume occupied by a chain, V_{inner} by an inner monomer, V_{end} by an end monomer and ΔV_{e} the difference in their occupied volume. Obviously the chain volume is just split up into the contribution given by the inner and end monomers.

T	ρ_∞	const_T
0.50	1.014	0.137
0.44	1.032	0.126

Table 3.2: Values obtained by fitting the data of Fig. 3.3.

By inserting this into the equation for the density we get

$$\rho = \frac{nN}{V} = \frac{nN}{nV_{\text{chain}}} = \frac{1}{V_{\text{inner}}\left[1 + \frac{2\Delta V_{\text{e}}}{NV_{\text{inner}}}\right]} \tag{3.4}$$

By approximating this equation by a Taylor expansion (for $N \gg 1$ it follows that $\frac{2\Delta V_{\text{e}}}{NV_{\text{inner}}} \ll 1$) up to the first order we finally get:

$$\rho \approx \rho_\infty\left(1 - \frac{2\Delta V_{\text{e}}}{NV_{\text{inner}}}\right) = \rho_\infty\left(1 - \frac{\text{const}}{N}\right), \tag{3.5}$$

where we set $\frac{1}{V_{\text{inner}}} = \rho_\infty$ — which gives the density of a polymer melt in the limit of long chains — and $\text{const} = \frac{2\Delta V_{\text{e}}}{V_{\text{inner}}}$. Following Eq. (3.5) the density of the polymer melt in the limit of long chains is approximatively given by $\rho \approx \rho_\infty$. With increasing chain length the density of a polymer melt will approach this limit. Equation (3.5) states that the density scales with the reciprocal chain length. This describes quite well the behavior observed in Fig. 3.1.

In Fig. 3.3 the density of the considered systems is shown for temperatures $T = 0.50, 0.44$ as a function of the reciprocal chain length. The dependence on the reciprocal chain length $1/N$ of ρ can be described by Eq. (3.5). As the volume of the considered systems decreases with decreasing temperature ρ_∞ is clearly temperature dependent. By regarding $\Delta\tilde{\rho} = \frac{\rho(T_2,N)/\rho(T_1,N)}{\rho(T_2,N=4)/\rho(T_1,N=4)}$ (see inset of Fig. 3.3) we check if $\text{const} = \frac{2\Delta V_{\text{e}}}{V_{\text{inner}}}$ also shows a temperature dependence. As $\Delta\tilde{\rho}$ grows linearly with the reciprocal chain length $1/N$, it becomes obvious that the const in Eq. (3.5) should also be chosen temperature dependent.

The slightly smaller value of $\text{const}_{T=0.44}$ (cf. Table 3.2) compared to $\text{const}_{T=0.50}$ shows that with decreasing temperature the dependence of the density on the chain length decreases. In other words the ratio of the volume between inner and end monomers is less pronounced for higher densities.

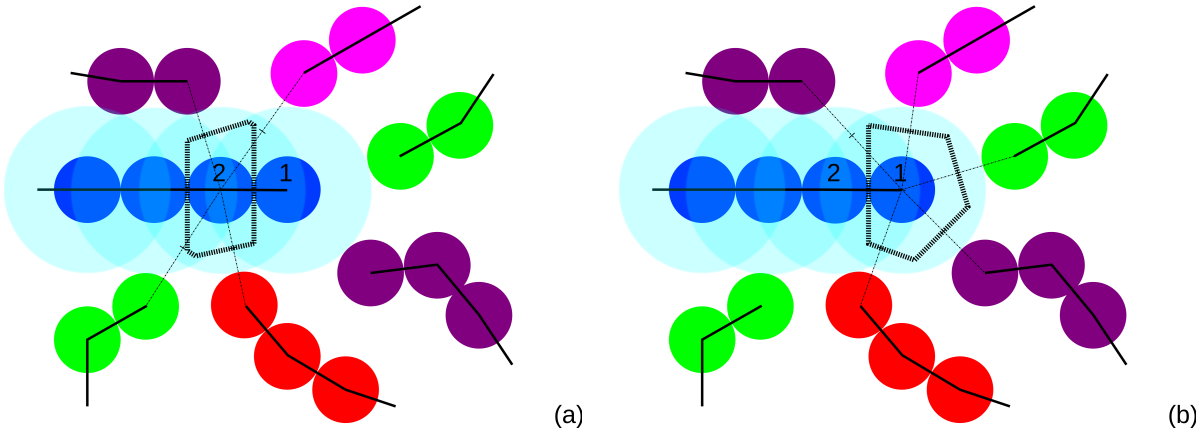

Figure 3.2: Schematic representation of the chain end effect. Monomers that are bonded within a chain are connected by black lines. For a better understanding the ratio of the distances between non-bonded and bonded monomers is exaggerated. Transparent light blue circles mark the space that is unaccessible to monomers that do not belong to the blue chain. In (a) the space occupied by the bonded monomer (denoted by 2) of the blue chain is marked by the black dashed frame. The definition of the assigned space region to a monomer is inspired by the definition of the Voronoi tessellation [10]. Space is assigned to a monomer by the following procedure: First the perpendicular bisectors between a monomer and its nearest neighbors are constructed. Then these perpendicular bisectors are connected so that they form the black dashed frames. (Thereby the perpendicular bisectors are chosen that allow to assign the smallest space region to the considered monomer. As a consequence, the formed black dashed frame does not have to be a polygon with six edges as it can be seen in (b)). In (b) the space occupied by the end monomer of the blue chain (denoted by 1) is marked by the black dashed frame. The bonded monomer within the chain occupies less space than the end monomer.

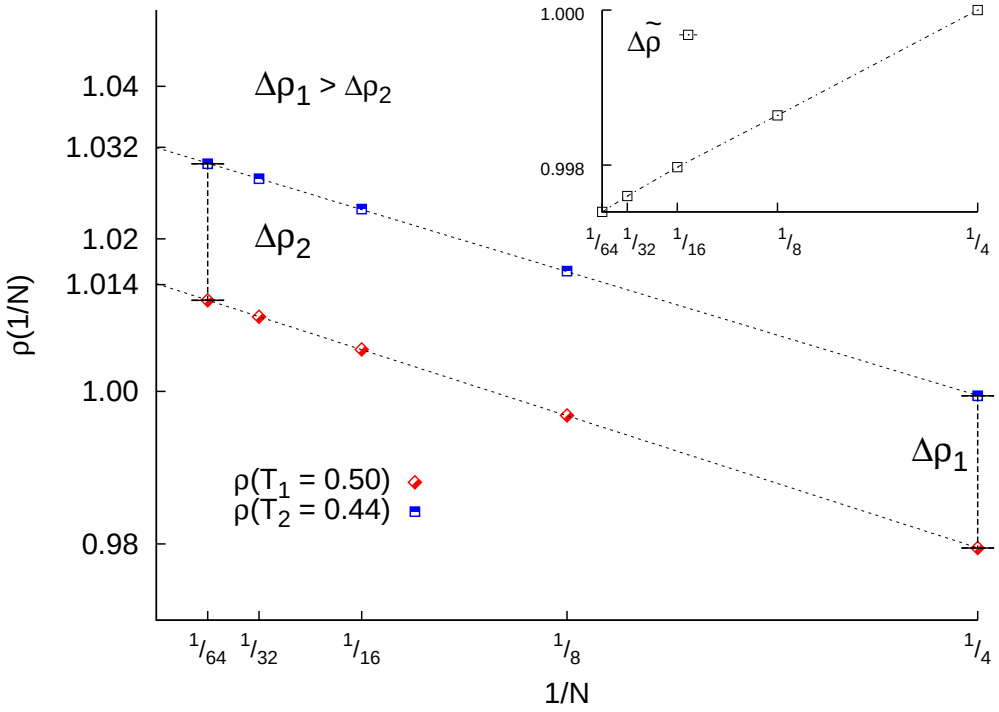

Figure 3.3: Main figure: Density ρ as a function of the reciprocal chain length $1/N$ for temperatures $T = 0.44, 0.50$. The black dashed lines indicate a fit using $f(N) = a(1 - \frac{b}{N})$ as suggested by Eq. (3.5). Due to the temperature dependence of the density, a is chosen to be temperature dependent. The inset indicates that b should also carry a temperature dependence. Inset: A deviation of $\Delta\tilde{\rho} = \frac{\rho(T_2,N)/\rho(T_1,N)}{\rho(T_2,N=4)/\rho(T_1,N=4)}$ from 1 indicates a deviation of the ratio of $\frac{\rho(T_2,N)}{\rho(T_1,N)}$ from that of $\frac{\rho(T_2,N=4)}{\rho(T_1,N=4)}$. This deviation nearly grows linearly with increasing N. Thus the const in Eq. (3.5) should also be temperature dependent.

3.2 Bulk modulus and high-frequency shear modulus

In this section we shortly discuss the bulk modulus and the high-frequency shear modulus [21]. We derive the bulk modulus from the isothermal compressibility. The isothermal compressibility can be defined as [21]

$$\kappa(T) = -\frac{1}{V}\frac{\mathrm{d}V}{\mathrm{d}p} \,. \tag{3.6}$$

It characterizes how the system's volume changes when a uniform infinitesimal pressure is exerted onto it. The prefactor $\frac{1}{V}$ sets this change in volume in relation to the probed volume and the minus sign accounts for the fact that the compressibility should be positive. (As the volume of a system will decrease when a pressure is exerted onto it, $\mathrm{d}V$ will be negative.)

There is a connection between the compressibility and the static structure factor (see section 3.3) in the limit for $q \to 0$. It can be shown that in the thermodynamic limit the compressibility is given by [40]

$$\kappa(T) = \lim_{q\to 0} \frac{S(q,T)}{k_\mathrm{B}T\rho} \tag{3.7}$$

The inverse of the compressibility is defined as the bulk modulus of the system, $K = \frac{1}{\kappa}$. In Fig. 3.4 we show the bulk modulus for $N = 64, 32, 16, 8, 4$ as a function of temperature T calculated as the reciprocal value of compressibility according to Eq. (3.7). The bulk modulus increases with decreasing T, i.e., the melt becomes less compressible; it also increases with increasing N, in a good approximation as

$$K = K_\infty - \frac{\mathrm{const}}{N} \,, \tag{3.8}$$

which is expected from Eq. (3.6) and the N dependence of ρ discussed before.

High frequency shear modulus We complete the discussion by considering the high-frequency shear modulus. This is especially motivated as we will discuss later (see section 5.1) its dynamic counterpart — the shear relaxation function — in greater detail. The high-frequency shear modulus can be defined as $G_\infty = G(t=0)$ with $G(t)$ being the shear relaxation function. The shear relaxation function is given by [5, 9]

$$G(t) = \frac{1}{k_\mathrm{B}TV}\big\langle \sigma_{zx}(t)\sigma_{zx}(0)\big\rangle \,, \tag{3.9}$$

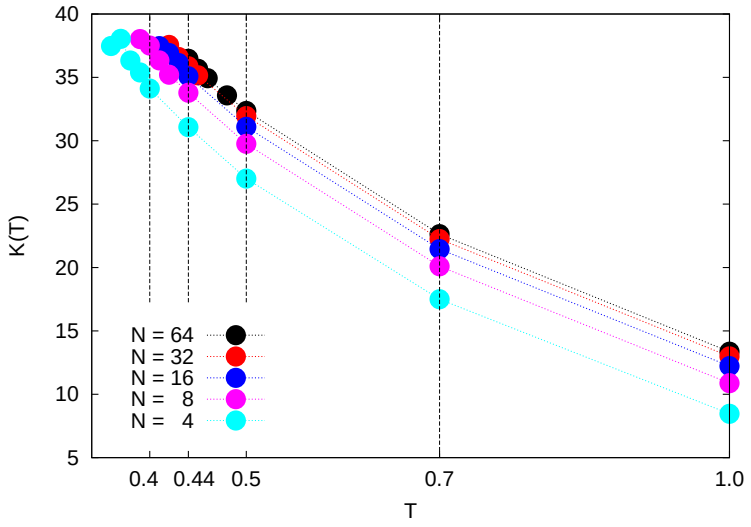

Figure 3.4: Bulk modulus $K(T)$ as a function of temperature T for $N = 64, 32, 16, 8, 4$. (See Table A.5 for the numerical values.)

where $\sigma_{\alpha\beta}$ denote the stress tensor with $(\alpha, \beta = x, y, z)$. The stress tensor is given by [55]

$$\sigma_{\alpha\beta} = \sum_{i=1}^{M} m v_{i,\alpha} v_{i,\beta} - \frac{1}{2} \sum_{i=1}^{M} \left(r_{i,\alpha} \frac{\partial U(\mathbf{r}^M)}{\partial r_{i,\beta}} + r_{i,\beta} \frac{\partial U(\mathbf{r}^M)}{\partial r_{i,\alpha}} \right) , \tag{3.10}$$

where the components of the position $\mathbf{r}_i$ (the velocity $\mathbf{v}_i$) of monomer i $(= 1, \ldots, M)$ are denoted by $r_{i,\alpha}$ $(v_{i,\alpha})$, and total potential is denoted by U. Here, for convenience, the monomers of the system are labeled by just one index $(i = 1, \ldots, M = nN)$.

In Fig. 3.5 G_∞ is depicted for all considered chain lengths. In the investigated temperature range G_∞ shows an almost linear dependence on the temperature.

3.3 Static structure factor

What are the basic ingredients that describe the structure of our system? And how can these basic ingredients be captured in a convenient way? One of these basic ingredients are the density fluctuations of the considered particles (monomers, chains) of the melt. By density fluctuations we understand the deviation of the local density from the averaged density.

The static structure factor [9, 21] can be seen as the mean square average of these density fluctuations. The static structure factor is closely related, via a Fourier

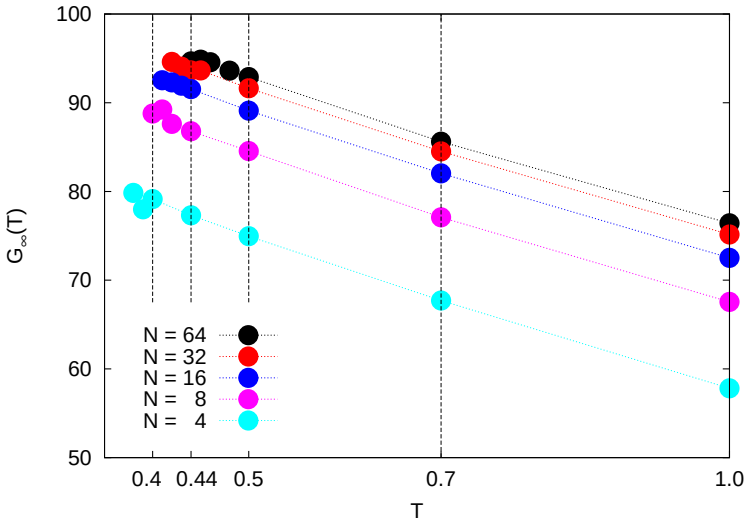

Figure 3.5: Shear modulus as a function of temperature T for $N = 64, 32, 16, 8, 4$. (See Table A.6 for the numerical values.)

transform, to the pair correlation function [9] which corresponds to the radial distribution function for the systems that we study (cf. section 3.4). In this context we want to mention that the first peak of the static structure factor (see for example Fig. 3.6) reveals informations about the ordering of monomers in shells around a labeled monomer [4]

In the following we introduce the static structure factor in terms of density fluctuations. Here we follow Ref. [37] and specially [4, 22]:

We consider a polymer melt consisting of n monodisperse chains of N monomers in a volume V. For a wave vector $\mathbf{q}$, the coherent monomer density fluctuations are given by

$$\rho_a(\mathbf{q}) = \sum_{i=1}^{n} \mathrm{e}^{\mathrm{i}\mathbf{q}\cdot\mathbf{r}_i^a} \quad (a = 1, \ldots, N) \,, \tag{3.11}$$

where $\mathbf{r}_i^a$ denotes the position of the ath monomer in the ith chain [22]. The sum over all monomers of a chain yields the total monomer density fluctuations

$$\rho_{\mathrm{tot}}(\mathbf{q}) = \sum_{a=1}^{N} \rho_a(\mathbf{q}) = \sum_{i=1}^{n}\sum_{a=1}^{N} \mathrm{e}^{\mathrm{i}\mathbf{q}\cdot\mathbf{r}_i^a} \,. \tag{3.12}$$

In terms of the total monomer density fluctuation the collective structure factor of the melt is then given by

$$S(q) = \frac{1}{nN}\langle \rho_{\mathrm{tot}}(\mathbf{q})^* \rho_{\mathrm{tot}}(\mathbf{q})\rangle \tag{3.13}$$

$$= \frac{1}{nN}\Big\langle \sum_{i,j=1}^{n}\sum_{a,b=1}^{N} \mathrm{e}^{-\mathrm{i}\mathbf{q}\cdot\mathbf{r}_i^a}\, \mathrm{e}^{\mathrm{i}\mathbf{q}\cdot\mathbf{r}_j^b} \Big\rangle\,, \tag{3.14}$$

with $\langle\cdot\rangle$ denoting the canonical averaging. This equation shows the above mentioned approach to the static structure factor as the mean square average of the density fluctuations.

The collective static structure can be split into an intra-chain and an inter-chain part [22] which yields

$$S(q) = w(q) + \rho h(q), \tag{3.15}$$

here $\rho = nN/V$ denotes the monomer density, $w(q)$ the intra-chain contribution and $\rho h(q)$ the inter-chain contribution[1]. These contributions are given by

$$\rho h(q) = \frac{1}{nN}\sum_{a,b=1}^{N}\Big\langle \sum_{i\neq j}^{n} \mathrm{e}^{-\mathrm{i}\mathbf{q}\cdot(\mathbf{r}_i^a - \mathbf{r}_j^b)} \Big\rangle \tag{3.16}$$

and

$$w(q) = \frac{1}{nN}\sum_{a,b=1}^{N}\Big\langle \sum_{i=1}^{n} \mathrm{e}^{-\mathrm{i}\mathbf{q}\cdot(\mathbf{r}_\mathrm{i}^a - \mathbf{r}_i^b)} \Big\rangle\,. \tag{3.17}$$

$w(q)$ is also named the "form factor" [22].

The main figures of Fig. 3.6 and Fig. 3.7 show the static structure factor $S(q)$ for two temperature $T = 0.50, 0.44$ and for chain lengths of $N = 64$ (Fig. 3.6) and $N = 4$ (Fig. 3.7). In this temperature interval all systems considered ($N = 64, 32, 16, 8, 4$ and pressure $p = 0$) have a structure that is typical of dense, disordered melts [4]. Additionally we show in Fig. 3.6 the form factor $w(q)$, it shows no differences upon cooling for the depicted temperature range.

The weak compressibility of the melt is reflected by the small value of $S(q)$ in the $q \to 0$ limit. In this context we want to remind of Eq. (3.7)

$$\kappa(T) = \lim_{q\to 0}\frac{S(q,T)}{k_\mathrm{B}T\rho(T)} \propto \lim_{q\to 0} S(q,T). \tag{3.18}$$

[1]Here $h(q)$ denotes the Fourier transform of the site-averaged intermolecular pair correlation function [4, 40]

In this sense the static structure factor is a continuation of the compressibility to finite wave vectors [37].

For larger values of q, $S(q)$ increases toward the first peak which is also the maximum of $S(q)$. The q-value for which $S(q)$ reaches its maximum will be denoted by $q_{\max}$. For our model $q_{\max} \simeq 7.1$ corresponds to the length scale of a monomer diameter. This points to the fact that the main contribution to $S(q_{\max})$ can be found in the amorphous packing of monomers in the nearest-neighbor shell located around a monomer [4].

From Fig. 3.6 it can be inferred that upon cooling the structure of the system stays essentially the same. Especially no long-range structural correlations develop. The only noticeable difference is that due to the increasing density the packing gets tighter which is reflected by the increase of $S(q_{\max})$ [4]. To illustrate this point we refer to the insets (a) and (b) of Fig. 3.6. These insets show that the first peak of $S(q)$ grows and shifts to larger q values upon cooling. The shift to larger q values indicates the increase of the density. This is also supported by the comparison of different chain lengths. In section 3.1 we showed that the density of systems compared at the same temperature and pressure depends on the chain length. The longer the chain length the higher the density. This is reflected when we compare the position of $q_{\max}$ for different chain length (see for example the inset (a) of Fig. 3.6): With increasing chain length $q_{\max}$ is shifted to higher values. By comparing this shift for the depicted chain lengths relatively to each other we find again a signature that the relative differences of the density scale like the reciprocal chain length. This observation seems even to hold for the height of the peak of $S(q_{\max})$.

3.4 Radial distribution function

In the last section we introduced the static structure which captures the static properties of a many body system in reciprocal space. Here we turn to a quantity that decodes the structure in real space. This is provided by the pair distribution function $g(\mathbf{r})$ [21]. It answers the question: Given that a particle sits in the origin how large is then the probability to find another particle at place $\mathbf{r}$.

As the systems that we study are homogeneous and isotropic there is no special point or a special direction. Thus it is sufficient to consider the radial pair distribution function $g(r)$, often just referred to as the radial distribution function, which depends only on the modulus of $r = |\mathbf{r}|$ [18]. It measures the probability to find a

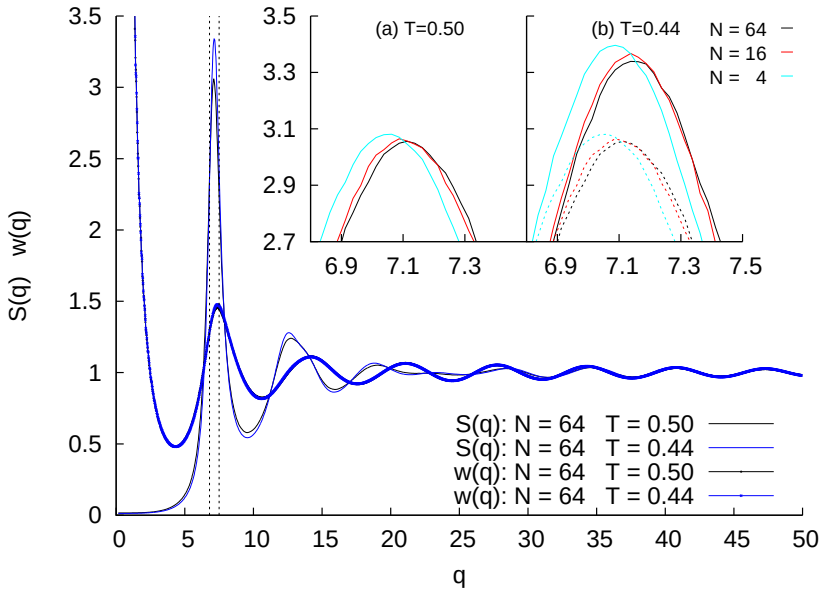

Figure 3.6: Main figure: Static structure factor $S(q)$ and form factor $w(q)$ for $N = 64$ and $T = 0.50; 0.44$ vs the modulus of the wave vector $\mathbf{q}$. The dash-dotted lines indicate the q-interval for which the insets are shown. It shows the region around the first peak of the static structure factor. Inset (a): Static structure factor for $N = 64; 16; 4$ and $T = 0.50$ for the indicated q-interval. Inset (b): Static structure factor for $N = 64; 16; 4$ and $T = 0.44$ for the indicated q-interval. The dash-dotted lines indicate the static structure factor for $T = 0.50$.

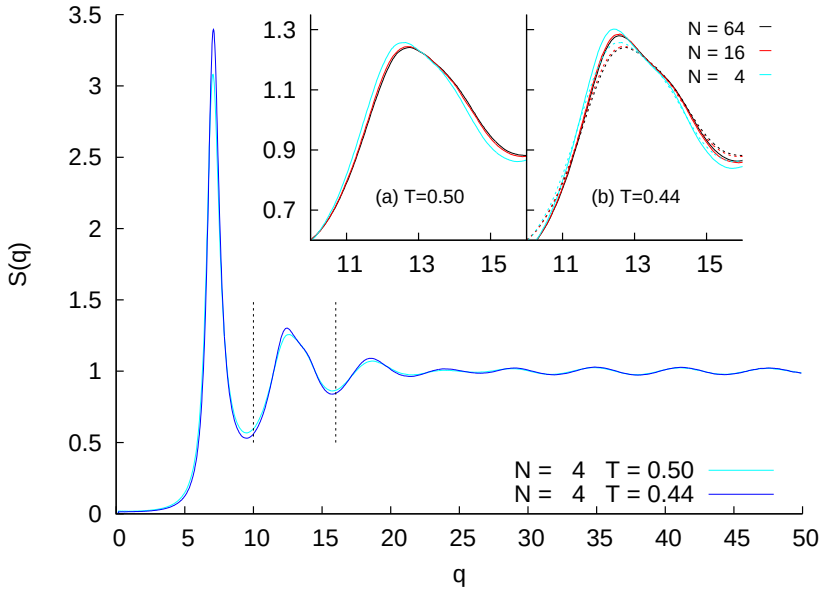

Figure 3.7: Main figure: Static structure factor for $N = 4$ and $T = 0.50; 0.44$ vs the modulus of the wave vector $\mathbf{q}$. The dash-dotted lines indicate the q-interval for which the insets are shown. It shows the region around the second peak of the static structure factor. Inset (a): Static structure factor for $N = 64; 16; 4$ and $T = 0.50$ for the indicated q-interval. Inset (b): Static structure factor for $N = 64; 16; 4$ and $T = 0.44$ for the indicated q-interval. The dash-dotted lines indicate the static structure factor for $T = 0.50$.

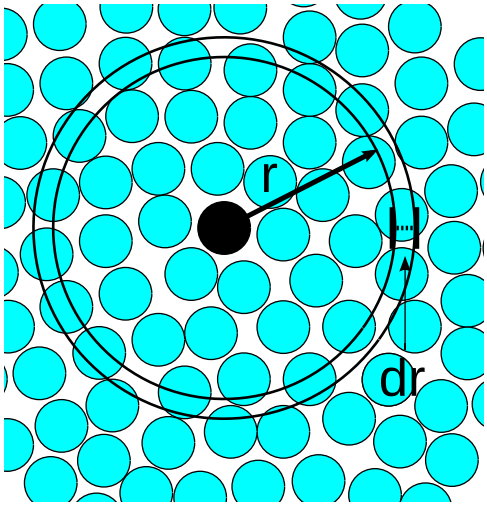

Figure 3.8: Schematic representation of the definition of the radial distribution function. Inspired by Ref. [21].

monomer at a distance r given there is a monomer in the origin. Figure 3.8 shows a schematic representation of $g(r)$. The radial distribution function for our systems can then be defined by [9]

$$\rho g(r) = \frac{1}{nN} \sum_{i \neq j}^{nN} \langle \delta(r - r_{ij}) \rangle \ , \tag{3.19}$$

with $r_{ij} = |\mathbf{r}_j - \mathbf{r}_j|$ denoting the distance between monomer i and j.

In this way the local density at a distance r from the origin is given by $\rho g(r)$. The prefactor $\frac{1}{nN}$ normalizes $\rho g(r)$ according to the total number of particles which is given by the number of chains n times the monomers per chain N.

As a result the average number of neighbors which reside within a distance R from a given monomer [9] is given by

$$\tilde{G}(R) = 4\pi\rho \int_0^R \mathrm{d}r \ r^2 g(r) \ . \tag{3.20}$$

By discretizing this concept spherical shells of thickness dr are considered at distance r from a labeled particle. The number of particles found in such a shell is proportional to $g(r)$ (cf. Fig. 3.8).

The position of the first peak of $g(r)$ reflects the distance between bonded monomers which is $\approx l_0$. The subsequent steep slope of $g(r)$ mirrors the stiff harmonic bond potential that we employ. The probability that bonded monomers are separated from each farer than the average bond length l_0 is very small. Non-bonded monomers cannot get so close to each other, as this is impeded by the steep slope of the repulsive part of the Lennard-Jones potential. The second peak shows the ordering of the monomers in shells around themselves. The subsequent oscillation around 1 accounts for the shells formed around the first nearest-neighbor shell. For large r $g(r)$ finally reaches a value of 1 which demonstrates that there is no long-range order in the polymer melts. This is equivalent to saying that $g(r)$ for large r probes the density of the system as the systems under consideration do not exhibit long range order.

The second peak shows the biggest temperature dependence of $g(r)$ (see the inset of Fig. 3.9). The temperature dependence of the first peak is less pronounced. From this observation we can extract the following: Decreasing the temperature goes along with increasing density which results in a tighter packing of the monomers. Due to this tighter packing monomers are rearranged. This rearrangement in the first shell among non-bonded monomers is more effective than for bonded chain monomers.

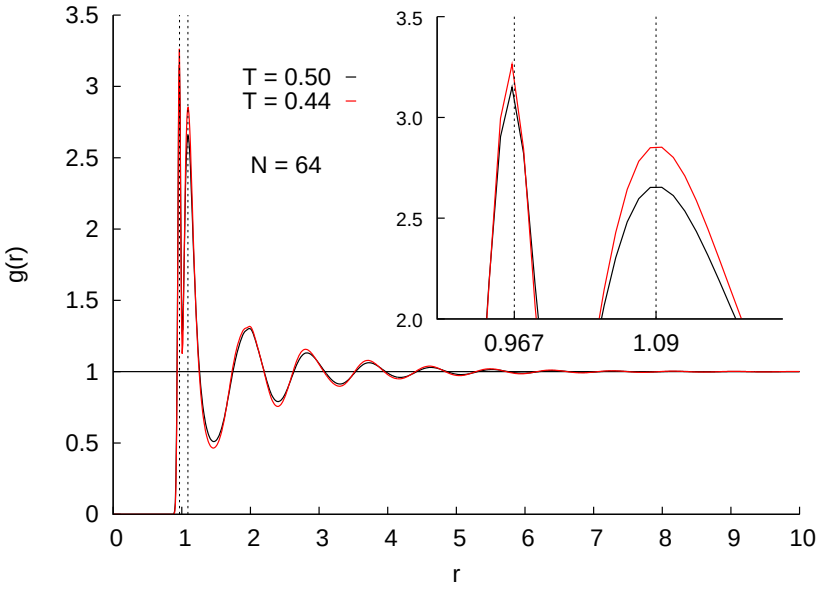

Figure 3.9: Main figure: For $N = 64$ the radial distribution function for the temperatures of $T = 0.50$ and 0.44 are compared. The black dash-dotted lines indicate $r = 0.967 = l_0$ and $r = 1.09$ around which the second peak occurs. Inset: Zoom on the first and second peaks of $g(r)$.

The impact of the chain length for totally flexible chains on the local structure is not large (see Fig. 3.10). By comparing $g(r)$ for chain lengths of $N = 64$ and $N = 4$ we find that the only remarkable differences are visible in the first and second peak. This effect is accounted for by the different relative ratio of end monomers. Two end monomers will approach each other not more closely than given by the Lennard-Jones potential. This leads to an inversion of the height of the peaks. For $N = 4$ the first peak is lower than for $N = 64$, whereas for the second peak the inverse observation can be done. This accounts for the fact that $\rho g(r)$ is a probability which obeys:

$$\int \mathrm{d}^3 r \; \rho g(r) = \text{const} \tag{3.21}$$

The small shift of $g(r)$ for $N = 64$ compared to that of $g(r)$ for $N = 4$ which occurs for distances larger than the monomer diameter seems to be explainable by the slightly larger density of the system consisting of chain length $N = 64$.

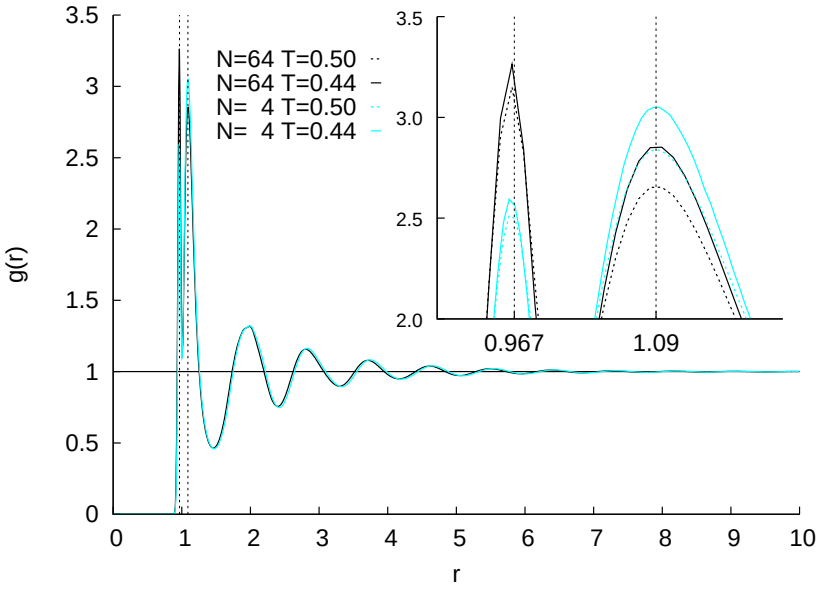

Figure 3.10: Main figure: For $T = 0.44$ the radial distribution function for $N = 64$ and $N = 4$ are compared. The black dash-dotted lines indicate $r = 0.967 = l_0$ and $r = 1.09$ around which the second peak occurs. Inset: Zoom on the first and second peaks of $g(r)$. An inversion of the height of these peaks for $N = 64$ and $N = 4$, when compared with each other, is observed.

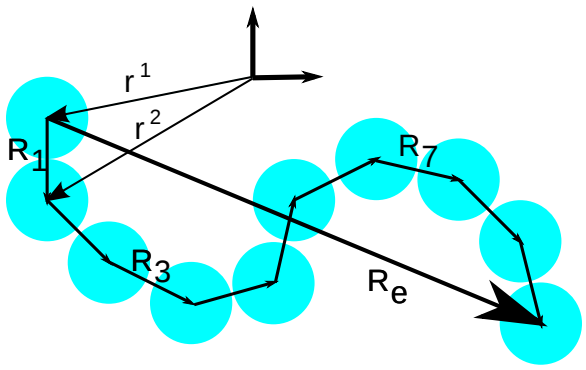

Figure 3.11: Schematic representation of the end-to-end vector. The vectors $\mathbf{r}^1$, $\mathbf{r}^2$ denote the position of monomer 1 and 2. The bond vector $\mathbf{R}_1$ denotes the bond from monomer 1 to 2 (analogously $\mathbf{R}_3$ and $\mathbf{R}_7$). $\mathbf{R}_\mathrm{e}$ denotes the end-to-end vector.

3.5 End-to-end vector

The quantities discussed so far can also be defined for non-polymeric systems. Now we turn to polymer specific quantities. A central quantity characterizing polymers is the end-to-end vector $\mathbf{R}_\mathrm{e}$ of the chains [26, 39, 71]. By considering the bond vectors $\mathbf{R}_a = \mathbf{r}^{a+1} - \mathbf{r}^a$ (where we dropped the indices denoting the chain) between the ath and $(a+1)$th monomer of a chain the end-to-end vector is given by (cf. Fig. 3.11)

$$\mathbf{R}_\mathrm{e} = \sum_{a=1}^{N-1} \mathbf{R}_a \ . \tag{3.22}$$

We consider the squared value of the end-to-end vector averaged over the whole system

$$R_\mathrm{e}^2 = \left\langle \mathbf{R}_\mathrm{e}^2 \right\rangle \ , \tag{3.23}$$

where $\langle\cdot\rangle$ denotes the canonical averaging.

In Fig. 3.12 we show in the inset the temperature dependence of R_e^2 for chain lengths $N = 64, 32, 16, 8, 4$. It can be seen that the absolute temperature dependence is only visible for chain length $N \gtrsim 16$ and that it increases with increasing chain length. Thus we show in the main figure of Fig. 3.12 $\frac{R_\mathrm{e}^2}{l_0^2 N}$ as a function of N. By doing so we relate the squared end-to-end vector to the $R_\mathrm{e}^2 = N l_0^2$ of an ideal chain [26] with bond length l_0. In this way the relative temperature dependence becomes obvious and the deviation from the behavior of an ideal chain. The reason for the deviation from the behavior of an ideal chain can be found in the excluded volume

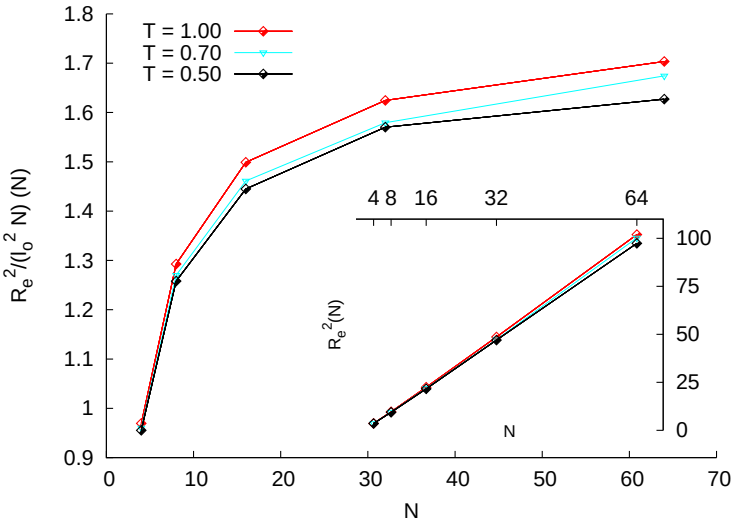

Figure 3.12: Main figure: $\frac{R_e^2}{l_0^2 N}$ as a function of N for temperatures $T = 1.00, 0.70, 0.50$ and chain lengths of $N = 64, 32, 16, 8, 4$. Inset: Mean squared end-to-end distance R_e^2 as a function of N for $T = 1.00, 0.70, 0.50$.

of the monomers. This constraint causes the chains to become swollen compared to ideal chains. We will discuss this in more detail in the next section.

The temperature dependence increases with chain length. This seems to be plausible as the main contribution of the change of the end-to-end distance as a function of temperature is found in the density. A lower temperature results in a higher density which just means that the monomers are tighter packed. As this affects all monomers of a chain the resulting effect is more pronounced for longer chains.

3.6 Intra-chain distances and effective bond length

In this section we discuss the internal distances of a chain. This is interesting to study as it reveals information about the conformation of the chains. The internal distances are measured between monomers of one chain. This distance can be related then to the curvilinear length between the considered monomers. This shows how monomer properties (e.g. the excluded volume) and system properties (e.g. the density) influence chain properties.

The mean-square intra-chain distance $\frac{R_s^2}{s}$ measures the mean-square distance between chain monomers that are separated by s bonds [8] and is given by

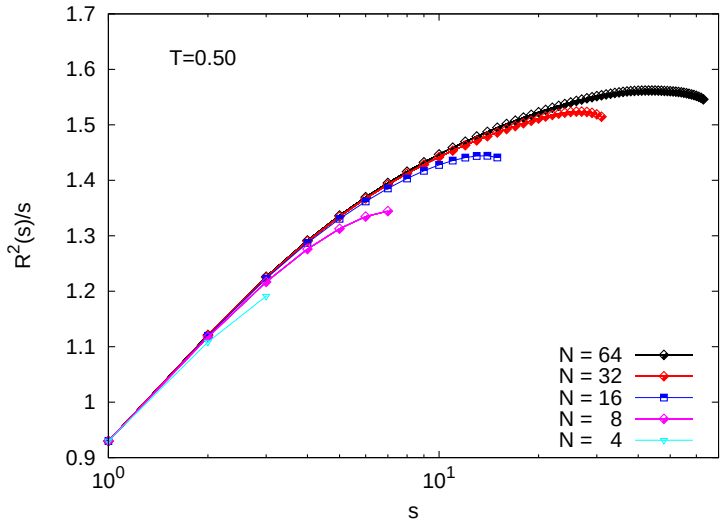

Figure 3.13: Mean-square intra-chain distance for $N = 64, 32, 16, 8, 4$ and $T = 0.50$ as a function of the curvilinear length s. $\frac{R_1^2}{1}$ is given by the squared equilibrium bond length $l_0^2 = 0.935$.

$$\frac{R_s^2}{s} = \frac{\langle \mathbf{R}_s^2 \rangle}{s} = \frac{1}{sn} \sum_{i=1}^{n} \frac{1}{N-s} \sum_{a=1}^{N-s} \langle (\mathbf{r}_i^{a+s} - \mathbf{r}_i^a)^2 \rangle \ , \tag{3.24}$$

where the positions of the monomers are denoted by $\mathbf{r}_i^a$. The subscript $i = 1, \ldots, n$ denotes the chains and the superscript $a = 1, \ldots, N$ the monomer in the chain. Equation (3.24) is evaluated for every mean-square intra-chain distance separately. s takes each value out of $s = 1, \ldots, N-1$ which corresponds to the smallest intra-chain distance between two monomers up to the end-to-end distance of the whole chain for $s = N - 1$.

As the mean-square intra-chain distance includes all intra-chain lengths it allows to compare systematically systems which only differ in the chain length of their constituting chains. Therefore it is an ideal quantity to compare the systems under consideration from a statical point of view.

In Fig. 3.13 we show the mean-square intra-chain distance $\frac{R_s^2}{s}$ at temperature $T = 0.50$ for different chain lengths $N = 64, 32, 16, 8, 4$. We want to point to the following observations: For $s = 1$ all curves start from a value that is given by the squared equilibrium bond length, which is given for our system by $l_0^2 = 0.935$.

For an ideal chain [26] (without excluded volume) which follows random walk statistics, $\frac{R_s^2}{s} = \text{const} = l_0^2$ for all s. The fact that $\frac{R_s^2}{s}$ in Fig. 3.13 is increasing indicates a swelling of the chain with respect to an ideal chain. An upper bound is

set by the limit of a completely extended conformation. In this situation the real-space distance is identical to the curvilinear distance, thereby $\frac{R_s^2}{s} = l_0^2 s$. Our data is not increasing so strongly, and the curves are levelling off for larger s. Our chains are thus not stiff. For large curvilinear length, $\frac{R_s^2}{s}$ reaches an apparent plateau. For $N \geq 16$, a final decrease of the curve is observed which can be explained by a finite chain length effect [79].

Effective bond length The mean-square intra-chain distance for the chains depicted in Fig. 3.13 follows an underlying universal curve. This curve can be described by [79]

$$\frac{R_s^2(s)}{s} = b_e^2\Big[1 - c_1\Big(\sqrt{\frac{24}{\pi^3}}\frac{1}{\rho b_e^3}\frac{1}{\sqrt{s}}\Big)\Big] \,, \tag{3.25}$$

with b_e being the effective bond length (see below) and c_1 a constant which is given by $c_1 = 1.2$ for a bead-spring model [79].

Wittmer and co-workers show that due to the incompressibility of the melt an effective repulsion between chain segments emerges which scales with $1/\sqrt{s}$ [79]. The effective repulsion gives rise to long range correlations in polymer melts. They argue that these long range correlations cause a systematic swelling of short chain segments. This swelling can be described by an effective bond length b_e. We employ equation Eq. (3.25), which is taken from this work, as a one-parameter extrapolation formula to determine the effective bond length b_e of our system as a function of temperature T.

We are aware of the fact that the studied chains here are comparatively smaller than the chains they focussed on. Nevertheless it should be possible to determine the temperature dependence of the effective bond length. In Eq. (3.25) the temperature dependence is accounted for by the temperature dependent density and effective bond length b_e. The temperature dependence of the density is conferred to the effective bond length.

In figures 3.14 – 3.16 we show the result of our fitting procedure. We choose a fitting interval of $s \in [3 : 30]$. This choice is motivated by the fact that in this interval $\frac{R_s^2}{s}$ is comparatively well approximated by Eq. (3.25) in [79]. See Fig. 3.17 for the values that we got by the fitting procedure. By plotting the values for the effective bond length as a function of temperature T we observe that they do not decrease in a linear way.

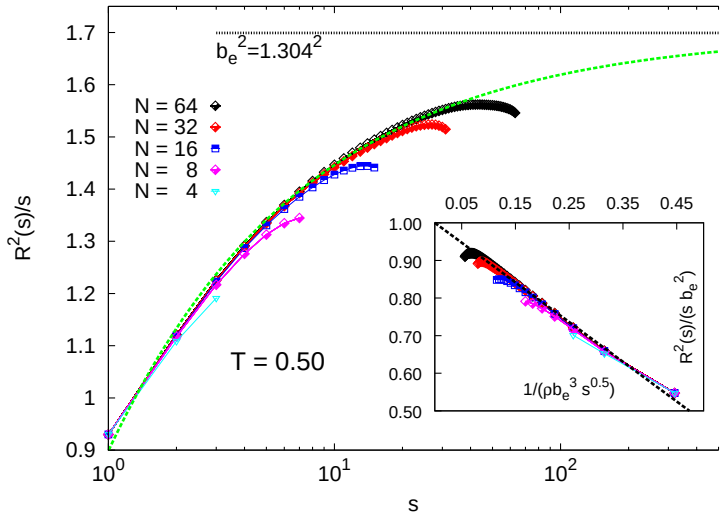

Figure 3.14: Main figure: Mean-square intra-chain distance for $N = 64, 32, 16, 8, 4$ vs curvilinear distance s for $T = 0.50$. $\frac{R_s^2}{s}$ is fitted using Eq. (3.25) to determine the effective bond length b_e which is found to be $b_e = 1.304$ for $T = 0.50$. The fitting interval is set to $s \in [3 : 30]$. Inset: The inset shows $R^2(s)/(sb_e^2)$ as a function of $1/(\rho b_e^3 \sqrt{s})$. The black dotted line is given by $f(x) = 1 - c_1\sqrt{\frac{24}{\pi^3}}\, x$. Thus the accordance of $\frac{R_s^2}{s}$ for the $N = 4, 8, 16, 32, 64$ with it shows the accuracy of the fit.

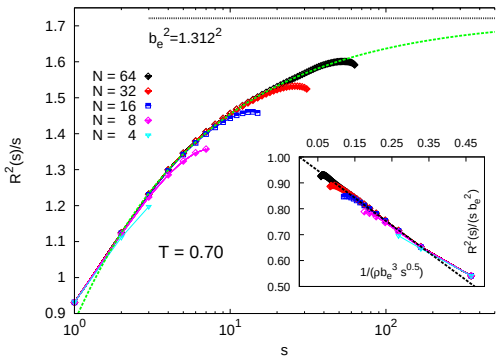

Figure 3.15: Mean-square intra-chain distance for $N = 64, 32, 16, 8, 4$ vs curvilinear distance s for $T = 0.70$. $\frac{R_s^2}{s}$ is fitted Eq. (3.25) to determine the effective bond length b_e which is found to be $b_e = 1.312$ for $T = 0.70$. The fitting interval is set to $s \in [3 : 30]$. Inset: The inset shows $R^2(s)/(sb_e^2)$ as a function of $1/(\rho b_e^3\sqrt{s})$. The black dotted line is given by $f(x) = 1 - c_1\sqrt{\frac{24}{\pi^3}}\,x$. Thus the accordance of $\frac{R_s^2}{s}$ for the $N = 4, 8, 16, 32, 64$ with it shows the accuracy of the fit.

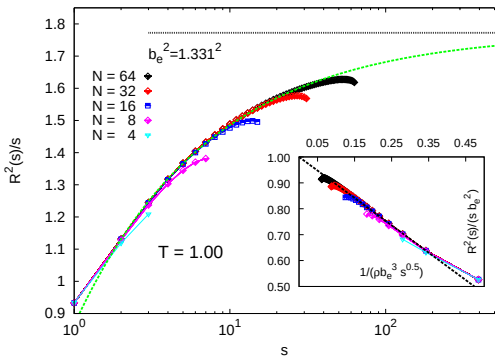

Figure 3.16: Mean-square intra-chain distance for $N = 64, 32, 16, 8, 4$ vs curvilinear distance s for $T = 1.00$. $\frac{R_s^2}{s}$ is fitted Eq. (3.25) to determine the effective bond length b_e which is found to be $b_e = 1.331$ for $T = 1.00$. The fitting interval is set to $s \in [3 : 30]$. Inset: The inset shows $R^2(s)/(sb_e^2)$ as a function of $1/(\rho b_e^3\sqrt{s})$. The black dotted line is given by $f(x) = 1 - c_1\sqrt{\frac{24}{\pi^3}}\,x$. Thus the accordance of $\frac{R_s^2}{s}$ for the $N = 4, 8, 16, 32, 64$ with it shows the accuracy of the fit.

In Fig. 3.18 we depict $\frac{R_s^2}{s}$ for a chain length of $N = 64$ and temperatures of $T = 0.50$ and 0.44. For $T = 0.44$ we observe that the mean-square intra-chain distance shows a behavior different from the one described above. We suppose that this is due to insufficient statistics. This can be explained when one takes into account that $\frac{R_s^2}{s}$ is always calculated over a finite number of phase space states given by simulation configurations. For this reason a behavior like the one found in Fig. 3.18, just reflects the fact, that the chains of the system were not given the chance to explore a big enough region of the phase space for the largest s [8].

Thus not all possible chain conformations could be realized which results in the undershoot of $\frac{R_s^2}{s}$. The example for the curve at $T = 0.44$ where a clear drop can be seen indicates that in this case chain configurations with a compressed conformation are overrepresented.

But due to the property of the mean-square intra-chain distance to scan the chains

T	b_e
1.00	1.331
0.70	1.312
0.50	1.304

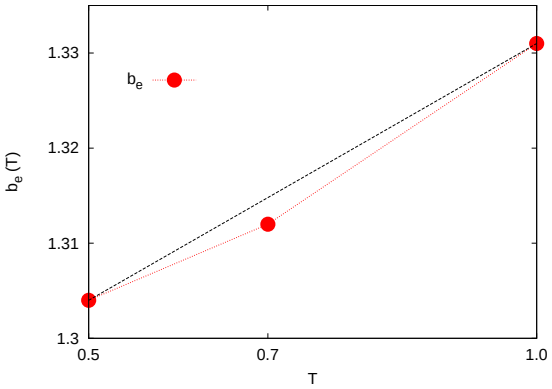

Figure 3.17: Left: Values determined for b_e by fitting $\frac{R_s^2}{s}$ for temperature $T = 1.00, 0.70, 050$ (see figures 3.14 – 3.16). We use equation Eq. (3.25) as a one-parameter extrapolation formula to determine the effective bond length b_e for our systems. Right: Effective bond length b_e as a function of temperature T. The effective bond length does not decrease as a linear function of T which is indicated by the black dashed line.

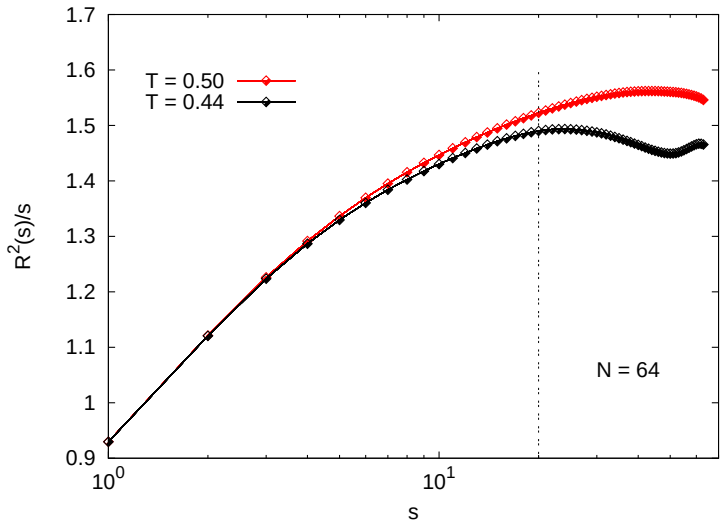

Figure 3.18: Mean-square intra-chain distance for $N = 64$ and temperature $T = 0.50, 0.44$. For $T = 0.44$ not enough simulation configurations are considered. The black dashed line indicates $s = 20$. Until this value $\frac{R_s^2}{s}$ shows a "normal" behavior.

on all s it is still possible to estimate up to which s the equilibration is sufficient. This argument will become stronger by referring to Fig. 3.18. It can be seen that up to an mean-square intra-chain distance of around $s \approx 20$, $\frac{R_s^2}{s}$ for $T = 0.50$ and $T = 0.44$ show a comparable behavior. For this reason we argue that the average

taken over simulation configurations up to internal distance of this order for this particular system reproduce sufficiently well an ensemble average. This is especially important when we approach lower temperatures. With decreasing temperatures it will get harder to have enough configurations in order to realize the ensemble average for all chain lengths. Due to the above consideration the finite number of configurations will be still sufficient to realize the ensemble average for subsegments of the chain.

Chapter 4

Dynamics: Mode-coupling theory inspired analysis

4.1 Introduction

In this chapter we analyse the dynamic properties of our system. Thereby we will focus on coherent and incoherent intermediate scattering functions, $\phi_q(t)$ and $\phi_q^s(t)$. Other dynamical quantities, like the mean square displacement of all monomers $g_0(t)$ or the shear relaxation function $G(t)$, will be discussed in the next chapter.

The coherent intermediate scattering function $\phi_q(t)$ [1] can be defined by [11]

$$\phi_q(t) = \frac{1}{MS(q)} \Big\langle \sum_{i=1}^{M} \sum_{j=1}^{M} \mathrm{e}^{-\mathrm{i}\mathbf{q}\cdot[\mathbf{r}_i(t)-\mathbf{r}_j(0)]} \Big\rangle \,, \tag{4.2}$$

where M denotes the total number of monomers, $\mathbf{r}_i(t)$ the position of monomer i of the melt at time t and $S(q)$ the static structure factor. The static structure factor accounts for the normalization of $\phi_q(t=0) = 1$:

$$\phi_q(t=0) = \frac{1}{MS(q)} \Big\langle \sum_{i=1}^{M} \sum_{j=1}^{M} \mathrm{e}^{-\mathrm{i}\mathbf{q}\cdot[\mathbf{r}_i(0)-\mathbf{r}_j(0)]} \Big\rangle = \frac{1}{MS(q)} MS(q) = 1 \,. \tag{4.3}$$

It can be regarded as the dynamic complement to the static structure factor. It shows how density fluctuations of the system are correlated. These density fluctua-

[1] In the context of the mode-coupling theory [37] the coherent intermediate scattering function is named density correlator and defined in terms of the total monomer density fluctuations, see section 3.3,

$$\phi_q(t) = \frac{1}{MS(q)} \big\langle \rho_{\mathrm{tot}}(\mathbf{q},t)^* \rho_{\mathrm{tot}}(\mathbf{q},t=0) \big\rangle \,. \tag{4.1}$$

tions are evaluated for a time difference $\Delta t = t - 0$ on a distinct real space wavelength λ which is given by the modulus of the considered wave vector, $|\mathbf{q}| = q = \frac{2\pi}{\lambda}$.

The incoherent intermediate scattering function $\phi_q^{\mathrm{s}}(t)$ can be defined by [11]

$$\phi_q^{\mathrm{s}}(t) = \frac{1}{M} \Big\langle \sum_{i=1}^{M} \mathrm{e}^{-\mathrm{i}\mathbf{q}\cdot[\mathbf{r}_i(t) - \mathbf{r}_i(0)]} \Big\rangle \,. \tag{4.4}$$

The incoherent and coherent intermediate scattering functions differ in the following fact: The coherent scattering function relates the position of a monomer at time t to the other monomers' position at time $t = 0$. In contrast to that the incoherent scattering function only correlates a monomer's position at time $t = 0$ to its position at a different time t.

In this sense $\phi_q(t)$ reveals more information about the system as the coherent intermediate scattering function especially probes the collective dynamics of the system. For large q-values $q \gg q^*$, where q^* denotes the first peak of the static structure factor $S(q)$, $\phi_q(t)$ and $\phi_q^{\mathrm{s}}(t)$ show a similar behavior. This is due to the fact that for the probed small distances the monomers — also in the case of the coherent intermediate scattering function — are only correlated with themselves.

4.2 Ideal mode-coupling theory analysis

In the following part we analyse our system in the framework of the ideal mode-coupling theory (MCT). Reference [11] suggests that this kind of analysis is appropriate for totally flexible models of polymer melts.

In the following paragraph we summarize the main aspects of the ideal MCT which are essential for our subsequent analysis. Our summary mainly follows [11] and references therein. For a more general introduction to MCT we refer to [37].

One of the key features of MCT [34–38] is the prediction of an ideal glass transition scenario. By this is understood that density fluctuation correlations will finally relax for temperatures above the critical temperature T_{c}. Below T_{c} these density fluctuations will not completely relax, but remain at some finite value. These density fluctuation correlations are described in terms of correlation functions like $\phi_q(t)$. MCT proposes a dynamical equation for $\phi_q(t)$, which is only determined by the static structure of the considered system.[2] Another key feature is that the time

[2] In the case of simple liquids the static structure can be captured only by $S(q)$. In an extension of the MCT to polymer systems [22], the static structure of the system — due to the existence of

evolution of $\phi_q(t)$ is coupled to that of all other products of coherent intermediate scattering functions, like $\phi_k(t)\phi_p(t)$, when $\mathbf{k}+\mathbf{p}=\mathbf{q}$ holds for the considered wave vectors $\mathbf{k}, \mathbf{p}$ and $\mathbf{q}$.

In the ideal MCT the ideal glass transition scenario is captured mathematically by a bifurcation, which occurs at T_c in the limit of $t \to \infty$:

$$\lim_{t\to\infty} \phi_q(t) = \begin{cases} 0 & \text{for } T > T_\mathrm{c}, \\ f_q(T) & \text{for } T \leq T_\mathrm{c}. \end{cases} \tag{4.5}$$

$f_q(T)$ is named the non-ergodicity parameter. It gives the finite value at which $\phi_q(t)$ remains for $t \to \infty$ for $T \leq T_\mathrm{c}$ and states the fact that below T_c $\phi_q(t)$ does not completely relax anymore.

As MCT especially deals with dynamics occurring for temperatures close to T_c, a measure to describe the 'distance' to T_c, the so-called separation parameter, is introduced by

$$\sigma = C\,\frac{T_\mathrm{c}-T}{T_\mathrm{c}}\ . \tag{4.6}$$

C is a constant depending on the considered system.

Another important prediction of MCT is that there is only one relevant time scale in a glass-forming system which is the microscopic time scale t_0. It is connected to the β relaxation time via

$$t_\sigma = \frac{t_0}{|\sigma|^{1/2a}} \qquad (0 < a < 0.3953), \tag{4.7}$$

and to the α relaxation time via

$$t'_\sigma = \frac{t_0}{|\sigma|^{\gamma}}\ , \tag{4.8}$$

with $\gamma = \frac{1}{2a}+\frac{1}{2b}$ $(\gamma > 1.765)$. The β relaxation time is the relevant time scale in the β regime and the α relaxation time in the α regime. (For a qualitative impression where this relaxation regimes occur see Fig. 4.1.)

The parameters a and b (the von Schweidler exponent) are related to each other via the exponent parameter λ by [11]

$$\lambda = \frac{\Gamma(1-a)^2}{\Gamma(1-2a)} = \frac{\Gamma(1+b)^2}{\Gamma(1+2b)} \qquad (1/2 \leq \lambda < 1)\ . \tag{4.9}$$

We will come back to this relation, when we determine γ from b.

polymer chains the system exhibits a higher structural complexity — is captured by $S(q)$ and the form factor $w(q)$.

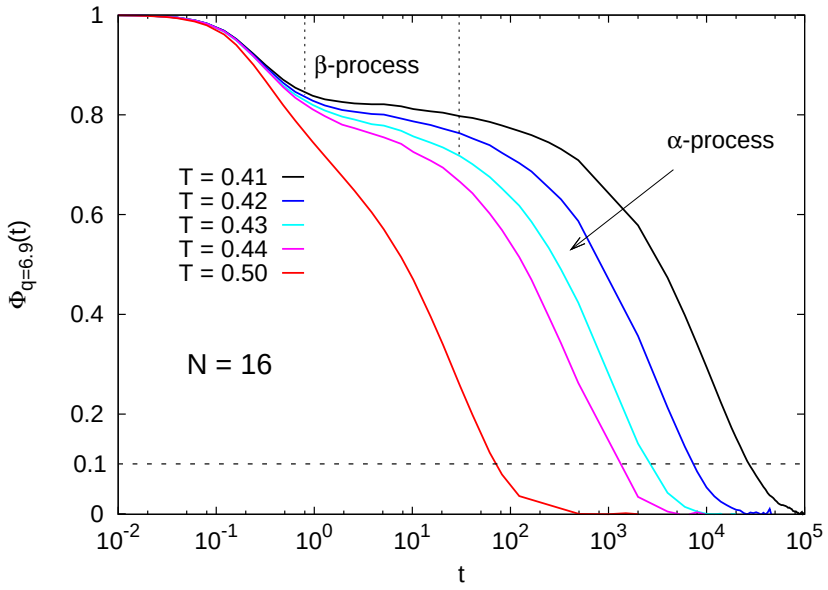

Figure 4.1: Coherent intermediate scattering function $\phi_{q=6.9}(t)$ for $N = 16$ as a function of time t. For $T = 0.43$ the approximated time intervals are indicated where the MCT α- and β processes occur. The value 0.1 is marked by a horizontal black dashed line. This value is used to determine a relaxation time τ_q^*.

Asymptotic formulae The following asymptotic expressions are only valid for temperatures close to T_c, which translates to small σ.

The intermediate time regime of the relaxation process within which $\phi_q(t)$ relaxes to the plateau ($\phi_q(t) \approx f_q$) and, for $T > T_c$, relaxes from it is called the β regime. This regime can be more precisely defined by $|f_q - \phi_q(t)| \ll 1$ [11]. Within this time regime MCT predicts that $\phi_q(t)$ can be expanded for $t \sim t_\sigma$ up to the first order by

$$\phi_q(t) = f_q^c + h_q \sqrt{|\sigma|}\, g(\hat{t}) \,, \tag{4.10}$$

with h_q the critical amplitude and $\hat{t} = t/t_\sigma$. Equation (4.10) can be rewritten using the β correlator $G_\beta(t) = g(\hat{t})\sqrt{|\sigma|}$ in the following form

$$\phi_q(t) = f_q^c + h_q G_\beta(t) \,. \tag{4.11}$$

Thereby it becomes obvious that the correction to f_q^c, namely $h_q G_\beta(t)$, splits into two factors: h_q only depends on q and the β correlator $G_\beta(t)$ only depends on t and σ. For this reason Eq. (4.11) is called the factorization theorem.

Mode-coupling theory predicts that there is a temperature interval in which intermediate scattering function can be collapsed onto each other by rescaling the time t

according to some relaxation time τ. The so rescaled $\phi_q(t)$ are predicted to collapse onto one temperature independent shape function $\widetilde{\phi}_q(\cdot)$, which is also referred to as a master function [37]. Mathematically this relation is expressed within the MCT by

$$\phi_q(t) = \widetilde{\phi}_q(t/t'_\sigma) \qquad (t \geq t_\sigma) \; . \tag{4.12}$$

This relation is referred to as the time-temperature superposition principle (TTSP).

Data analysis: procedure The final goal of this analysis is to determine mode-coupling-theory quantities like $T_\mathrm{c}, a, b, \lambda, \gamma$ as a function of the chain length N.

We perform this analysis in the following steps:

- First we check in which temperature interval the time-temperature superposition principle (TTSP) is valid. This gives a first estimate within which temperature interval the ideal MCT applies [11]. Additionally to that, it gives us an estimation for the lower bound of the non-ergodicity parameter f_q^c.
- In a second step we check if the factorization theorem is also valid. This step also serves as a crosscheck.
- In a subsequent step we fit $\phi_q(t)$ by employing the von Schweidler law and its leading order correction Eq. (4.14) This is done for each chain length for the lowest temperature that still obeys the TTSP. By this choice we can access the largest time interval possible for the fit. Therefore the fit results might reach the highest possible precision. From these fits we determine values for the MCT quantities of b, f_q^c.
- From the fitted b we calculate λ and a, and from a and b we calculate γ. The calculated γ is then used to determine T_c by fitting the α relaxation times for different temperatures in a temperature interval where the ideal MCT can be applied.

4.2.1 Time-temperature superposition principle

We start to determine the temperature interval within which the ideal mode-coupling theory should apply. This temperature interval can be found by testing the time-temperature superposition principle.

In the figures 4.2 – 4.6 we show the result of the rescaled coherent intermediate scattering function for the chain lengths of $N = 64, 32, 16, 8, 4$.

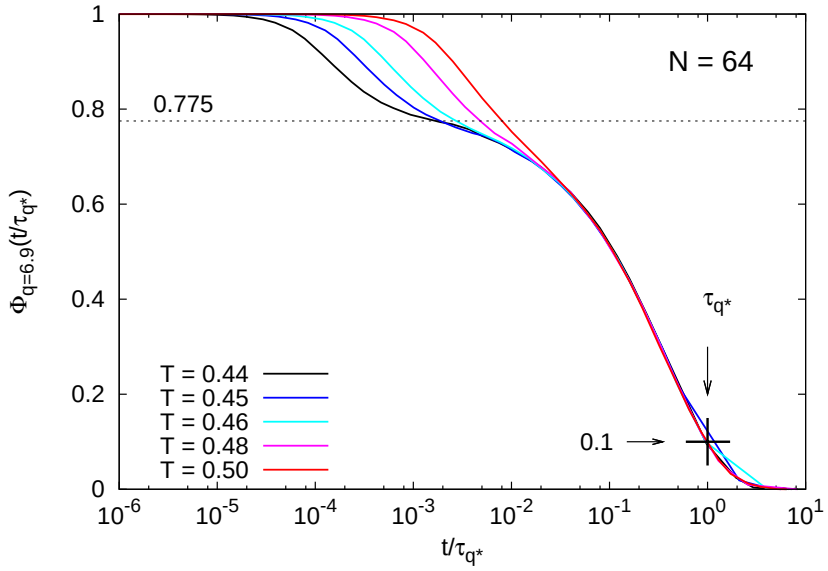

Figure 4.2: Coherent intermediate scattering function $\phi_{q=6.9}(t)$ for $N = 64$ rescaled according to the α relaxation time $(\tau_{q^*})^{-1}$, which is determined by $\phi_{q=6.9}(t = \tau_{q^*}) = 0.1$.

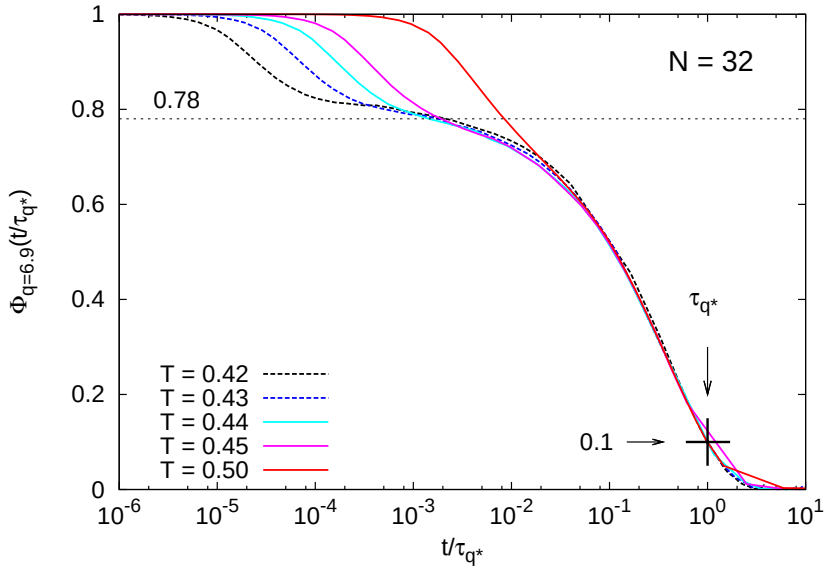

Figure 4.3: Coherent intermediate scattering function $\phi_{q=6.9}(t)$ for $N = 32$ rescaled according to the α relaxation time $(\tau_{q^*})^{-1}$, which is determined by $\phi_{q=6.9}(t = \tau_{q^*}) = 0.1$.

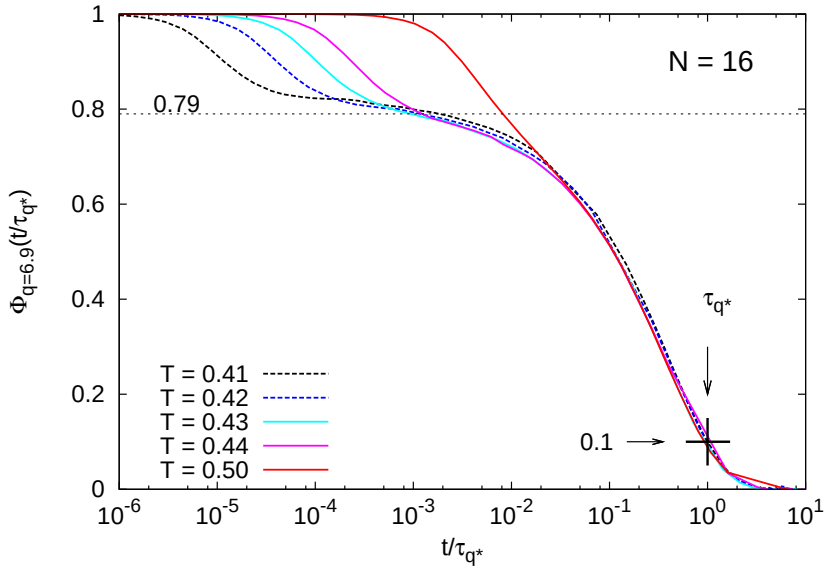

Figure 4.4: Coherent intermediate scattering function $\phi_{q=6.9}(t)$ for $N = 16$ rescaled according to the α relaxation time $(\tau_{q^*})^{-1}$, which is determined by $\phi_{q=6.9}(t = \tau_{q^*}) = 0.1$.

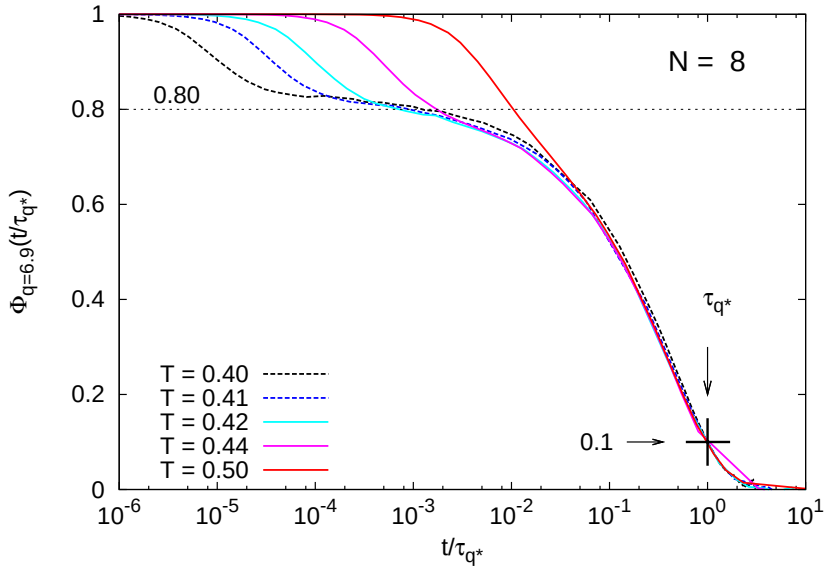

Figure 4.5: Coherent intermediate scattering function $\phi_{q=6.9}(t)$ for $N = 8$ rescaled according to the α relaxation time $(\tau_{q^*})^{-1}$, which is determined by $\phi_{q=6.9}(t = \tau_{q^*}) = 0.1$.

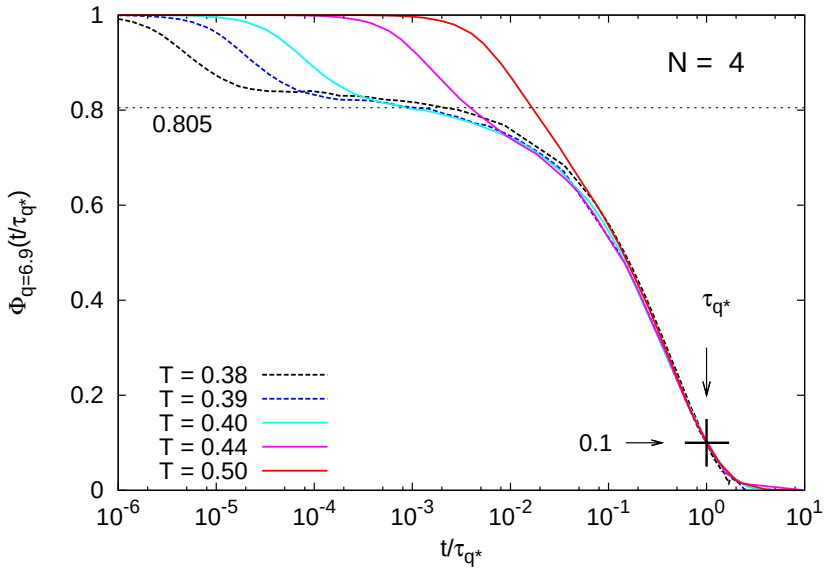

Figure 4.6: Coherent intermediate scattering function $\phi_{q=6.9}(t)$ for $N = 4$ rescaled according to the α relaxation time $(\tau_{q^*})^{-1}$, which is determined by $\phi_{q=6.9}(t = \tau_{q^*}) = 0.1$.

Procedure

To test the TTSP we proceed as follows: We start by considering $\phi_q(t)$ for $q = 6.9$ for a distinct chain length. We take $q = 6.9$ as for this value $\phi_q(t)$ shows a comparatively high plateau value and therefore promises to give more precise results.

We illustrate our approach for the example of $\phi_{q=6.9}(t)$ for $N = 64$. For this chain length we simulated in the NVT ensemble the following temperatures $T = 0.50, 0.48, 0.47, 0.46, 0.45, 0.44$. First we determine the time where $\phi_q(t)$ reaches a value of 0.1 for every simulated temperature. This time is determined by a linear interpolation between two data points which are closest to 0.1. Next the $\phi_q(t)$'s are rescaled according to these determined times. These times are the longer the lower the considered temperature is. (Compare Fig. 4.1 where a similar situation for $N = 16$ is depicted.) Due to the employed method to determine these relaxation times and the limited amount of data points one needs to adjust the relaxation times in order that $\phi_q(t)$ collapses onto one master curve. This is done as long as the following criteria are obeyed [32, 77]

- the final relaxation process should overlap for all temperatures close to T_c^{MCT},
- $\phi_q(t)$ for a temperature should not intersect with $\phi_q(t)$ of a higher temperature,

	$N = 64$	$N = 32$	$N = 16$	$N = 8$	$N = 4$
lowest temperature T	0.44	0.44	0.43	0.42	0.40
lower bound for $f^{\mathrm{c}}_{q=6.9}$	0.775	0.78	0.79	0.80	0.805

Table 4.1: Results obtained by testing the time-temperature superposition principle: Lowest temperature T denotes the lowest temperature that still seems to fulfill the TTSP. Lower bound for $f^{\mathrm{c}}_{q=6.9}$ denotes a lower bound for $f^{\mathrm{c}}_{q=6.9}$ for each distinct chain length N.

- the higher the temperature, the earlier $\phi_q(t)$ should leave the master curve.

Figure 4.2 shows the result of this procedure for the chain length $N = 64$. All simulated temperatures seem to fulfill the TTSP. Therefore the ideal MCT should apply even for the lowest temperature showed, $T = 0.44$. The black dashed line indicates a lower bound for the non-ergodicity parameter, $f^{\mathrm{c}}_{q=6.9} \geq 0.775$.

In Fig. 4.3 we show the result for $N = 32$. Here the lowest simulated temperature $T = 0.42$ (dash-dotted line) apparently violates the TTSP. The fact that $\phi_q(t)$ for $T = 0.42$ collapses in the final decay onto the other curves, but does not collapse onto the master curve for intermediate times can be taken as a sign that this temperature does not fulfill the TTSP. For $T = 0.43$ it is not so clear if the TTSP is still fulfilled or not, as the differences in the shape of its $\phi_q(t)$ and the master curve are rather small. The lower bound for $f^{\mathrm{c}}_{q=6.9} \geq 0.78$, determined from the data for $T > 0.43$, is indicated by a black dashed line.

The outcome of this procedure for $N = 16, 8$ and 4 is depicted in figures 4.4 – 4.6. For $N = 16$ the temperatures $T = 0.42$ and $T = 0.41$ violate the TTSP. From $T > 0.42$ a lower bound for $f^{\mathrm{c}}_{q=6.9} \geq 0.79$ is determined. For $N = 8$ $T = 0.41$ and $T = 0.40$ violate the TTSP. From $T > 0.41$ a lower bound for $f^{\mathrm{c}}_{q=6.9} \geq 0.80$ is determined. Finally, for $N = 4$ $T = 0.39$ and $T = 0.38$ violate the TTSP. From $T > 0.39$ a lower bound for $f^{\mathrm{c}}_{q=6.9} \geq 0.805$ is determined.

In Table 4.1 we summarize our first results by testing the TTSP. For each chain length we determined the lowest temperature T for which the associated coherent intermediate scattering function still obeys the TTSP. We also give a lower bound for $f^{\mathrm{c}}_{q=6.9}$.

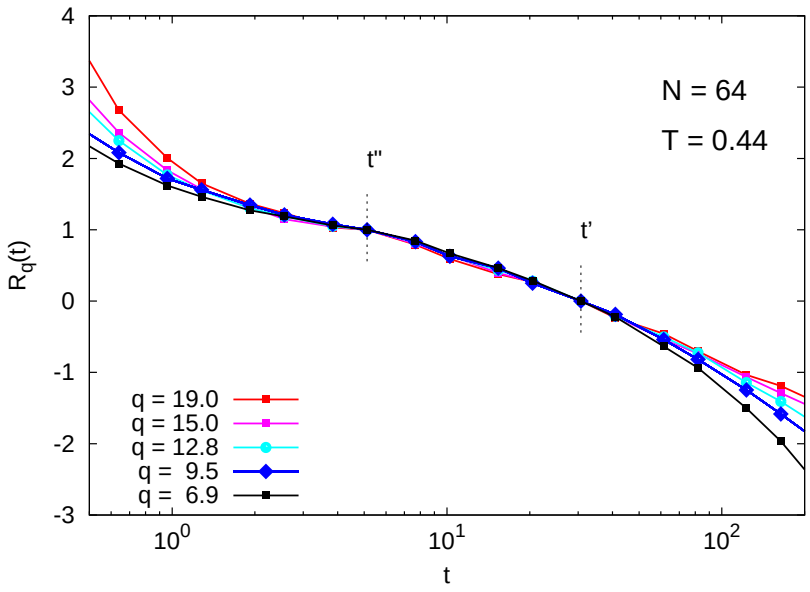

Figure 4.7: The factorization theorem is tested by applying Eq. (4.13) to $\phi_q(t)$ at $T = 0.44$ for $N = 64$. By definition $R_q(t'' = 5.12) = 1$ and $R_q(t' = 30.7)$=0. The times t'' and t' were chosen such that they are within the plateau region. Thereby it becomes visible that even for times $t \lesssim t''$ and $t \gtrsim t'$ the curves collapse onto each other. The ordering of $\phi_q(t)$ before entering the β regime and when leaving it is conserved. The curves follow some kind of 'ordering rule' [11].

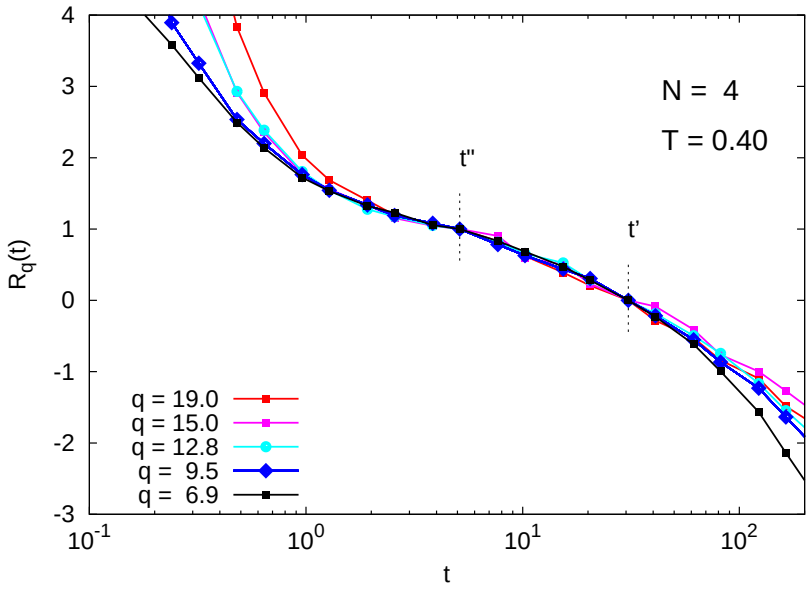

Figure 4.8: The factorization theorem is tested by applying Eq. (4.13) to $\phi_q(t)$ at $T = 0.40$ for $N = 4$. By definition $R_q(t'' = 5.12) = 1$ and $R_q(t' = 30.7)$=0. The times t'' and t' were chosen such that they are within the plateau region. Thereby it becomes visible that even for times $t \lesssim t''$ and $t \gtrsim t'$ the curves collapse onto each other. The ordering of $\phi_q(t)$ before entering the β regime and when leaving it is conserved, except for $q = 15$.

4.2.2 Factorization theorem

The factorization theorem (cf. Eq. (4.11)) can be tested by fixing two times t'' and t', with $t'' \lesssim t_\sigma \lesssim t'$, and evaluation of the following relation [11]

$$R_q(t) = \frac{\phi_q(t) - \phi_q(t')}{\phi_q(t'') - \phi_q(t')} = \frac{G_\beta(t) - G_\beta(t')}{G_\beta(t'') - G_\beta(t')} \,. \tag{4.13}$$

As this test is easy to implement it was widely tested in simulations of fragile glass formers [33, 47, 76, 78].

By definition $R_q(t)$ does not dependent on q anymore. Therefore — in the β regime — $\phi_q(t)$ for different q values should collapse onto each other for one fixed temperature. By this the MCT prediction of the factorization theorem can be effectively tested. In Fig. 4.7 this test is carried out for $N = 64$ and the lowest temperature that still obeys the TTSP. It can be seen that $\phi_q(t)$ for different q values collapse onto each other on a time interval of about two decades. The ordering rule [11] is valid, which is a more significant test, is also obeyed.

In Fig. 4.8 we show the similar test for a chain length of $N = 4$ and for the lowest

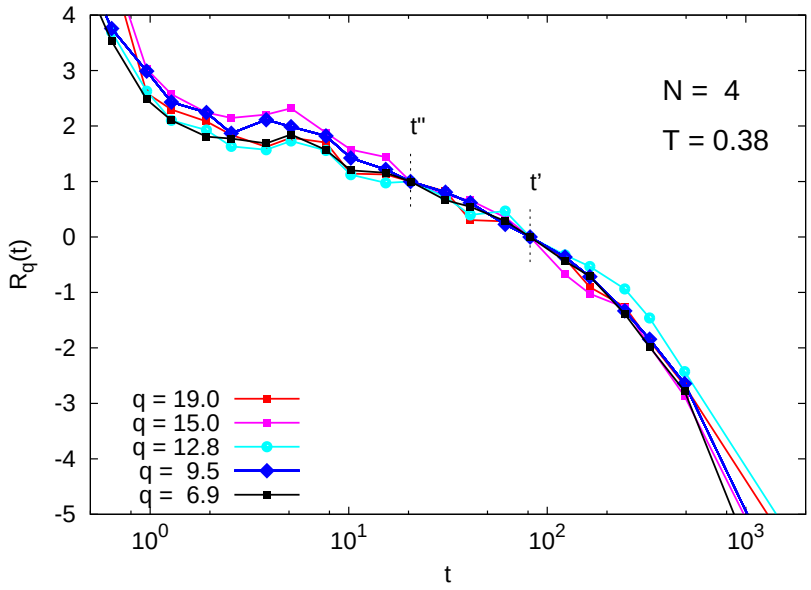

Figure 4.9: The factorization theorem is tested by applying Eq. (4.13) to $\phi_q(t)$ at $T = 0.38$ for $N = 4$. By definition $R_q(t'' = 20.48) = 1$ and $R_q(t' = 81.92)$=0. The times t'' and t' were chosen such that they are within the plateau region. Thereby it becomes visible that even for times $t \lesssim t''$ and $t \gtrsim t'$ the curves collapse onto each other. The ordering of $\phi_q(t)$ before entering the β regime and when leaving is not conserved.

temperature for which the TTSP still holds. t'' and t' are fixed for the same times as in the case for $N = 64$ and $T = 0.44$. Here, as well as for $N = 64$, $\phi_q(t)$ for different q values collapse onto each other. The ordering rule is valid except for $q = 15$.

In Fig. 4.9 we tested the factorization theorem for $N = 4$ and a temperature that is slightly below the value we determined for T_c (see section 4.2.4). The factorization theorem seems to be still valid but from our test it seems that the ordering rule is not fulfilled anymore. The fluctuations in the data shown in Fig. 4.9 can be explained by insufficient statistics.

4.2.3 Fit procedure

We proceed our analysis in the framework of the ideal mode-coupling theory by determining b and $f^c_{q=6.9}$ for each chain length. Therefore we fit the late β process, which overlaps with the early α process of the coherent intermediate scattering function [11]. For this purpose we use the following formulation of the von Schweidler

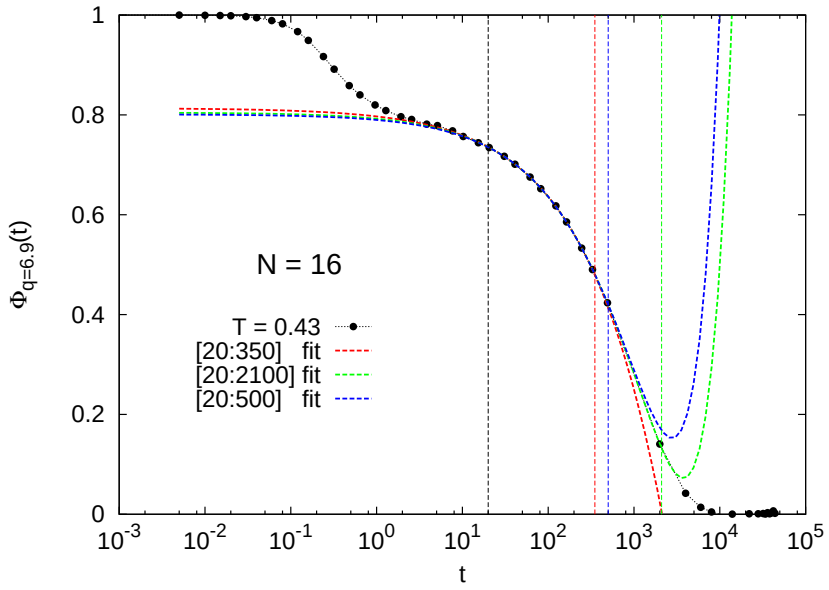

Figure 4.10: Coherent intermediate scattering function $\phi_{q=6.9}(t)$ for $N = 16$ and $T = 0.43$; fitted according to Eq. (4.14). Left border of the fit interval fixed at $t = 20$ while the right border is varied: $t = 350, 500, 2100$. Red color: right border $t = 350$ and corresponding fit. Blue color: right border $t = 500$ and corresponding fit. Green color: right border $t = 2100$ and corresponding fit.

law and the first leading order corrections to it as proposed in [11]

$$\phi_q(t) = f_q^{\mathrm{c}} - \widetilde{h}_q^{\mathrm{fit}} \left(t/t'_\sigma\right)^b + \widetilde{h}_q^{\mathrm{fit}} \widetilde{B}_q^{\mathrm{fit}} \left(t/t'_\sigma\right)^{2b} \qquad (t_\sigma \leq t) \; . \tag{4.14}$$

Here, f_q^{c} denotes the non-ergodicity parameter, t'_σ the α relaxation time, and b the von Schweidler exponent. $\widetilde{h}_q^{\mathrm{fit}}$ is given by $h_q B$, where h_q denotes the critical amplitude and B is a constant. $\widetilde{B}_q^{\mathrm{fit}}$ is given by BB_q, where B_q is a q dependent constant.

For the fitting procedure we use $\phi_q(t)$ for the lowest temperature where the TTSP is still fulfilled. We make this choice, as for this temperature the ideal mode-coupling theory should still hold. The lower the temperature, the longer the relaxation process exhibited by $\phi_q(t)$. Therefore, the time interval within which Eq. (4.14) can be fitted is the largest, which should finally result in an appropriate good fit result.

Before we start to fit our data according to Eq. (4.14), we first determine the appropriate fit interval. This is crucial, as it serves a some kind of "hidden" fit parameter [11]. In the subsequent part, we want to use one fit interval for all chain lengths to avoid inconsistencies. This choice is motivated by the following:

For $\phi_q(t)$ of all chain lengths and temperatures data is collected at the same times intervals. We are therefore restricted in the choice of the fit interval to these times intervals. The distances between the times at which the data is collected varies, as we use a logarithmic pattern to collect data. Thus, the fit interval cannot easily be adapted for each $\phi_q(t)$ so that it captures the same part of the relaxation process. Additionally to this, the accessible temperatures of $\phi_q(t)$ for each chain length considered separately do not have to be necessarily in the same relative distance to T_{c}.

Consequently, the best choice to make seems to use the same fit interval for all chain lengths within which $\phi_q(t)$ shows a similar relaxation behavior. To this end we fit different temperatures for each chain length for which $\phi_q(t)$ exhibits a similar relaxation process.

The choice of the temperatures for each chain length is made due to the following: We assume that T_{c} depends on the chain length, which seems likely when we consider our findings from the test of the TTSP. Furthermore, we assume that for all chain lengths the lowest temperature for which $\phi_q(t)$ still obeys the TTSP is at least at similar relative distance to T_{c}. Consequently, we assume that $\phi_q(t)$ for these lowest temperatures exhibit a similar relaxation process for each chain length. Therefore using the lowest temperature for which the TTSP is still valid for each chain length

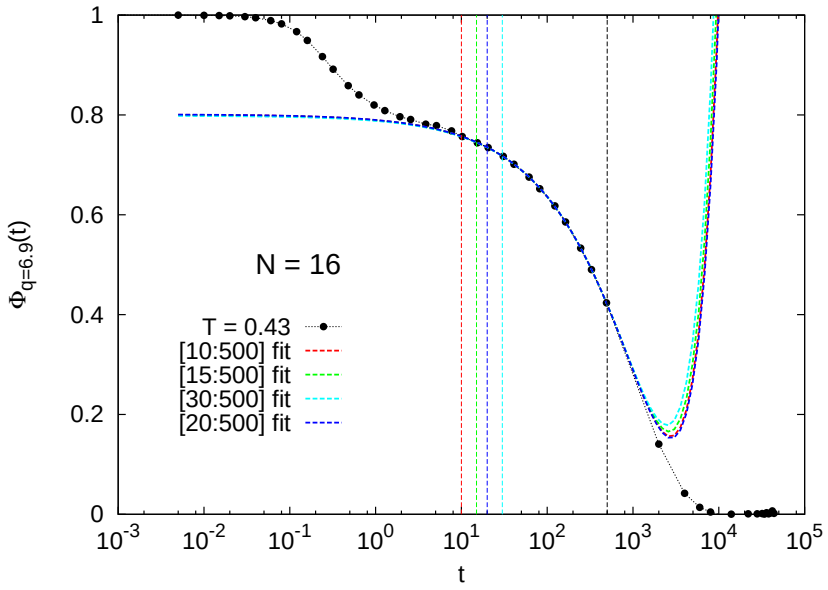

Figure 4.11: Coherent intermediate scattering function $\phi_{q=6.9}(t)$ for $N = 16$; fitted according to Eq. (4.14). Right border of the fit interval fixed at $t = 500$ while the left border is varied: $t = 10, 15, 20, 30$. Red color: left border $t = 10$ and corresponding fit. Green color: left border $t = 15$ and corresponding fit. Blue color: left border $t = 20$ and corresponding fit. Light blue color: left border $t = 30$ and corresponding fit.

separately, should lead to a comparable accuracy in the fit result. As above stated fitting the lowest temperature allows to use the largest fit range.

For these reasons we finally decide to choose one fit interval which we use for the fit of $\phi_q(t)$ for all chain lengths. By this approach we hope to minimize the systematic error or at least that the systematic error that we make is of comparable size for all chain lengths.

Determination of the fit interval

In the following, we use $\phi_{q=6.9}(t)$ for $N = 16$ and $T = 0.43$ to determine an appropriate fit interval when applying the von Schweidler fit (Eq. (4.14)). We choose $N = 16$, as it represents the intermediate chain length.

In Fig. 4.10 we fix the left border (small times) of the fit interval at $t = 20$ and vary the right border by using $t = 350, 500, 2100$. This choice is motivated by the demand that the fit interval should cover a large part of the late β relaxation. We then select the fit interval by the requirement that the fit should describe $\phi_{q=6.9}(t)$

fit interval	$[10, 500]$	$[15, 500]$	$[20, 500]$	$[30, 500]$	$[20, 2100]$	$[20, 350]$
$f_{\mathrm{q}}^{\mathrm{c\ fit}}$	0.800690	0.799937	0.801079	0.798482	0.804714	0.813493
$t_{\sigma}^{\prime\,\mathrm{fit}}$	1.73638	1.73835	1.73368	1.78833	1.71399	1.92642
b^{fit}	0.600357	0.604114	0.598863	0.610147	0.578552	0.517702
B_q^{fit}	0.00600064	0.00599139	0.00601125	0.00603533	0.00583008	0.00190140
h_q^{fit}	0.0154884	0.0152056	0.0156019	0.0149752	0.0170899	0.0232808

Table 4.2: Values obtained by fitting $\phi_{q=6.9}(t)$ according to Eq. (4.14) for $N = 16$ and $T = 0.43$ using different fit intervals (cf. Fig. 4.11).

	averaged	$[20, 500]$	standard deviation
$f_{\mathrm{q}}^{\mathrm{c\ fit}}$	0.80098	0.801079	0.0020671
$t_{\sigma}^{\prime\,\mathrm{fit}}$	1.7421	1.73368	0.024678
b^{fit}	0.59841	0.598863	0.010664
B_q^{fit}	0.0059737	0.00601125	7.3313×10^{-5}
h_q^{fit}	0.015672	0.0156019	7.4191×10^{-4}

Table 4.3: Values obtained by fitting $\phi_{q=6.9}(t)$ according to Eq. (4.14) for $N = 16$ and $T = 0.43$ using $[20, 500]$ as fit interval compared to the average value. This average is calculated for the obtained values using the fit intervals of $[10, 500]$, $[15, 500]$, $[20, 500]$, $[30, 500]$ and $[20, 2100]$. For this average the standard deviation is indicated.

for the largest possible range, especially outside the fit interval. This requirement seems to be best met, when the right right border is set to $t = 500$.

We then proceed to vary the left border using $t = 10, 15, 20, 30$, while keeping the right one fixed ($t = 500$, see Fig. 4.11). The variation of the left border (in the range that we probe) seems to result in a less pronounced influence on the fit than the variation of the right border.

In Table 4.2 we present the values that we obtained by fitting $\phi_q(t)$ of $N = 16$ for a temperature of $T = 0.43$ by using Eq. (4.14). As the values obtained by choosing $t_{\mathrm{left}} = 20$ and $t_{\mathrm{rigth}} = 350$ as fit interval differ strongly compared to the other values we excluded them from now on. This strong deviation can be explained as follows: This choice of the fit interval neglects a big part of the α relaxation. Therefore the fit is comparatively less descriptive compared to the other fits.

The mean value and the standard deviation of the obtained values for the other

fit intervals are given in Table 4.3. From this table it can inferred that the values by fitting within the border of $t_{\text{left}} = 20$ and $t_{\text{right}} = 500$ are comparable to the mean values obtained from different fits and within the standard deviation.

We studied this influence as it is done for $N = 16$ and $T = 0.43$ for the other chain length ($N = 4, 8, 32, 64$ for the lowest temperature that still obeys the TTSP) and we find comparable results meaning that the variation of different values for b^{fit} obtained for different fit intervals is comparable. But due to the restriction of the choice of the fit interval — as already mentioned above — it seems clearer to fix the fit interval. Therefore we fix the fit interval to $t_{\text{left}} = 20$ and $t_{\text{right}} = 500$ for the following fits.

Fit

Now we fit — using the determined fit interval — according to Eq. (4.14) $\phi_q(t)$ for all considered chain lengths $N = 64, 32, 16, 8, 4$ where we use the lowest temperature for which $\phi_{q=6.9}(t)$ still fulfills the TTSP.

In Fig. 4.12 we show the result for $N = 16$ and $T = 0.43$. We start to fit $\phi_{q=6.9}(t)$ according to Eq. (4.14) where all five parameters $f_{\text{q}}^{\text{c fit}}, t_\sigma^{\prime\text{fit}}, b^{\text{fit}}, B_q^{\text{fit}}, h_q^{\text{fit}}$ are treated as fit parameters. Thereafter we determine the crossover-time t_{co} by the condition $\phi_{q=6.9}(t_{\text{co}}) = f_{q=6.9}^{\text{c}}$ [11]. By using this relation we are then able to determine f_q^{c} for the other considered q-values of $4, 9.5, 12.8$. In a last step, we then fit $\phi_q(t)$ for $q = 4, 9.5, 12.8$ by setting $b^{\text{fit}}, t_\sigma^{\prime\text{fit}}$ to the values obtained from the fit for $q = 6.9$ and $f_{\text{q}}^{\text{c fit}}$ to the values obtained by using $\phi_{q=a}(t_{\text{co}}) = f_{q=a}^{\text{c}}$. Thus, only B_q^{fit} and h_q^{fit} are fitted.

As an additional test, we fitted the incoherent intermediate scattering function. In Fig. 4.13 the incoherent intermediate scattering function for $N = 16$ and $T = 0.43$ is fitted according to Eq. (4.14) where we used for $b^{\text{fit}}, t_\sigma^{\prime\text{fit}}$ and t_{co} the values determined by the fit of $\phi_{q=6.9}(t)$. As in these fits only two free fit parameters are employed, they show how comparatively well this fit procedure works.

In the figures Fig. 4.15 – Fig. 4.17 we show the results from the fit procedure for the other chain lengths. In Table 4.4 we give an overview of the values obtained by fitting $\phi_{q=6.9}(t)$ for each chain length for the lowest temperature for which the TTSP still holds according to Eq. (4.14).

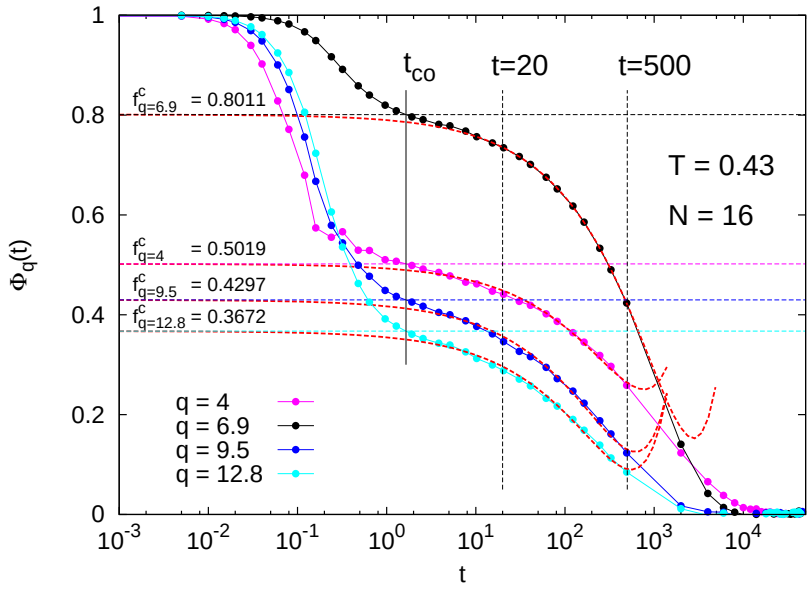

Figure 4.12: Coherent intermediate scattering function $\phi_{q=4,6.9,9.5,12.8}(t)$, for $N = 16$ and $T = 0.43$; fitted according to Eq. (4.14). For $q = 4, 9.5, 12.8$, $t'_\sigma = 1.73368$, $b = 0.598863$ and the corresponding f_q^c ($f^c_{q=4} = 0.5019$, $f^c_{q=9.5} = 0.4297$, $f^c_{q=12.8} = 0.3672$) are set. The crossover-time $t_{\rm co} = 1.6475$ and the fit interval are marked by vertical black lines.

	$N = 64$	$N = 32$	$N = 16$	$N = 8$	$N = 4$
$f_{\rm q}^{\rm c\ fit}$	0.789512	0.790253	0.801079	0.811316	0.819615
t'_σ	1.84349	1.69287	1.73368	1.75646	1.76730
$b^{\rm fit}$	0.595253	0.616997	0.598863	0.571892	0.546314
$B_q^{\rm fit}$	0.006146	0.007276	0.006011	0.005662	0.000279
$h_q^{\rm fit}$	0.018284	0.018166	0.015602	0.016771	0.014499
$t_{\rm co}$	1.8510	1.7508	1.6475	1.3325	1.6268

Table 4.4: Values obtained for $f_{\rm q}^{\rm c\ fit}, t'_\sigma, b^{\rm fit}, B_q^{\rm fit}, h_q^{\rm fit}$ by fitting $\phi_{q=6.9}(t)$ for each chain length according to Eq. (4.14). For each chain length the lowest temperature which still obeys the TTSP is used ($N = 64 : T = 0.44$, $N = 32 : T = 0.44$, $N = 16 : T = 0.43$, $N = 8 : T = 0.42$, $N = 4 : T = 0.40$). For all fits we used the fit interval $t_{\rm left\ border} = 20$ and $t_{\rm right\ border} = 500$. Additionally the crossover-times $t_{\rm co}$ are given which are determined by $\phi_{q=6.9}(t_{\rm co}) = f^c_{q=6.9}$.

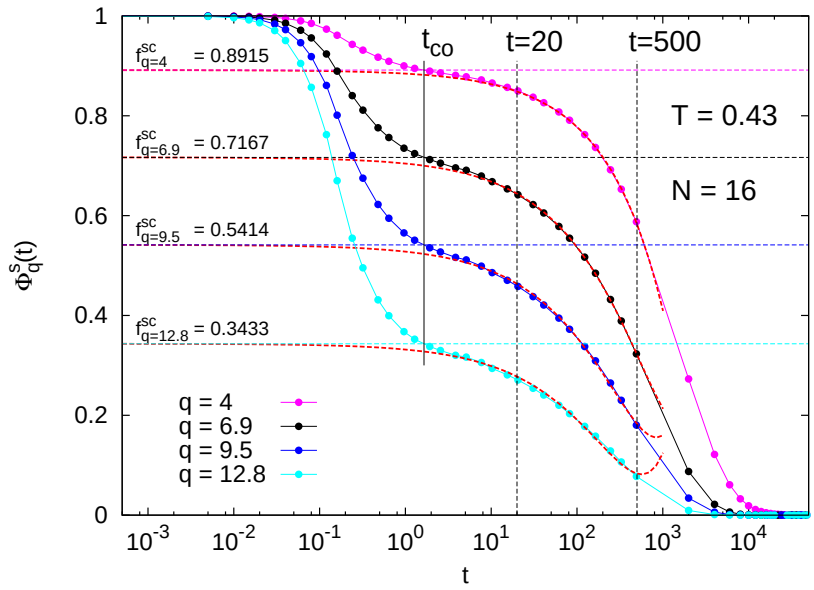

Figure 4.13: Incoherent intermediate scattering function $\phi^s_{q=4,6.9,9.5,12.8}(t)$ for $N = 16$ and $T = 0.43$; fitted according to Eq. (4.14). $t'_\sigma = 1.73368$, $b = 0.598863$ and the corresponding f^c_q ($f^c_{q=4} = 0.8915, f^c_{q=6.9} = 0.7167, f^c_{q=9.5} = 0.5414, f^c_{q=12.8} = 0.3433$) are set. The cross over time $t_{\rm co} = 1.6475$ and the fit interval are marked by vertical black lines.

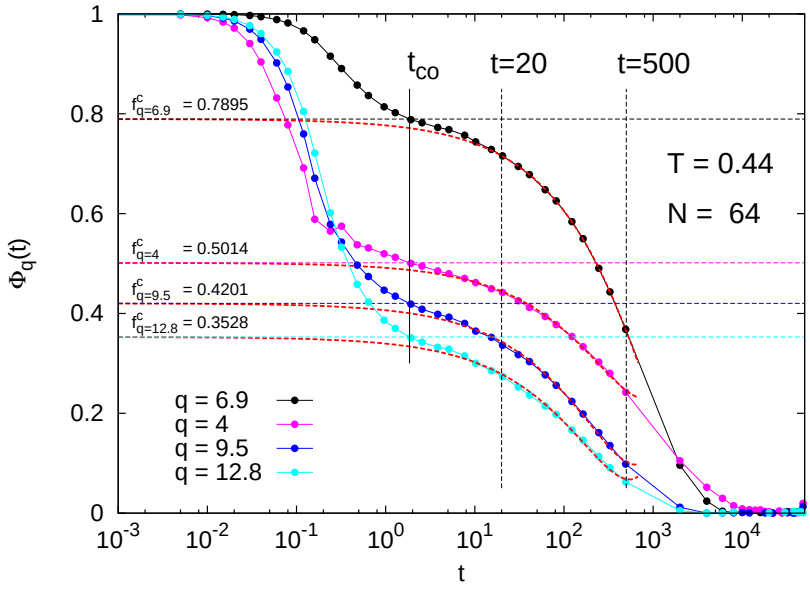

Figure 4.14: Coherent intermediate scattering function $\phi_{q=4,6.9,9.5,12.8}(t)$ for $N = 64$ and $T = 0.44$; fitted according to Eq. (4.14). For $q = 4, 9.5, 12.8$, $t'_\sigma = 1.84349$, $b = 0.595253$ and the corresponding f^c_q ($f^c_{q=4} = 0.5014$, $f^c_{q=9.5} = 0.4201$, $f^c_{q=12.8} = 0.3528$) are set. The crossover-time $t_{co} = 1.851$ and the fit interval are marked by vertical black lines.

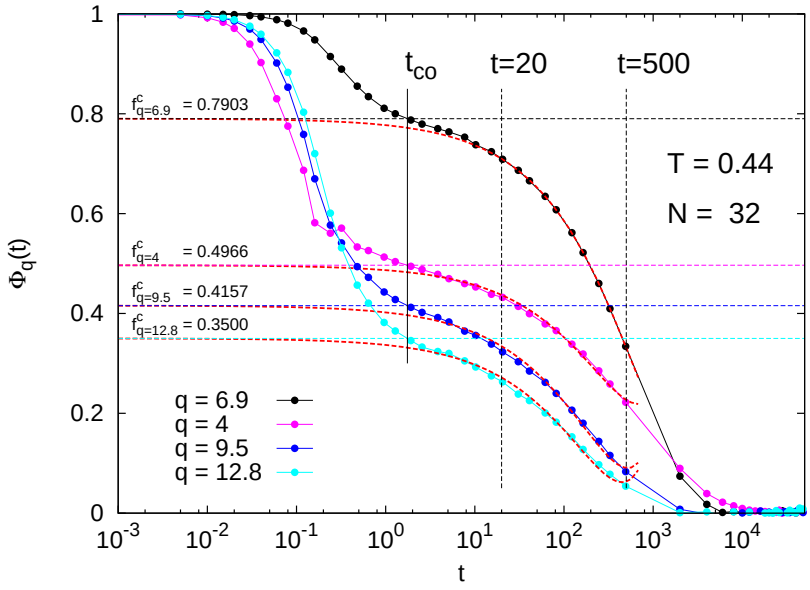

Figure 4.15: Coherent intermediate scattering function $\phi_{q=4,6.9,9.5,12.8}(t)$ for $N = 32$ and $T = 0.44$; fitted according to Eq. (4.14). For $q = 4, 9.5, 12.8$, $t'_\sigma = 1.69287$, $b = 0.616997$ and the corresponding f^c_q ($f^c_{q=4} = 0.4966$, $f^c_{q=9.5} = 0.4157$, $f^c_{q=12.8} = 0.3500$) are set. The crossover-time $t_{co} = 1.7508$ and the fit interval are marked by vertical black lines.

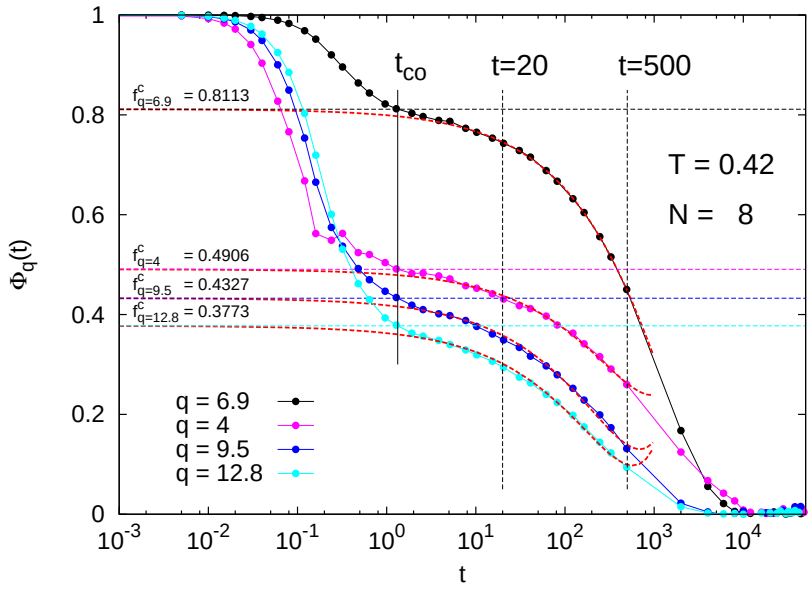

Figure 4.16: Coherent intermediate scattering function $\phi_{q=4,6.9,9.5,12.8}(t)$ for $N = 8$ and $T = 0.42$; fitted according to Eq. (4.14). For $q = 4, 9.5, 12.8$, $t'_\sigma = 1.75646$, $b = 0.571892$ and the corresponding f_q^c ($f^c_{q=4} = 0.4906$, $f^c_{q=9.5} = 0.4327$, $f^c_{q=12.8} = 0.3773$) are set. The crossover-time $t_{\rm co} = 1.3325$ and the fit interval are marked by vertical black lines.

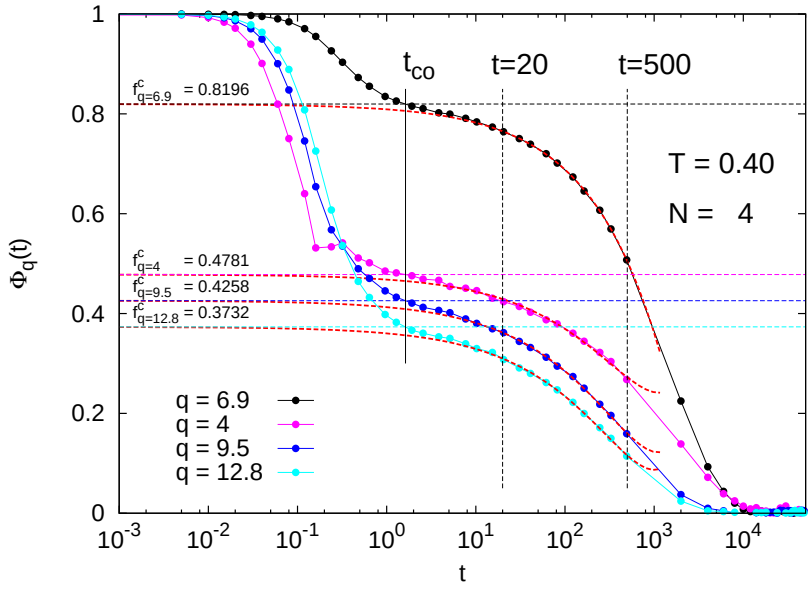

Figure 4.17: Coherent intermediate scattering function $\phi_{q=4,6.9,9.5,12.8}(t)$ for $N = 4$; fitted according to Eq. (4.14). For $q = 4, 9.5, 12.8$, $t'_\sigma = 1.7673$, $b = 0.546314$ and the corresponding f_q^c ($f^c_{q=4} = 0.4781$, $f^c_{q=9.5} = 0.4258$, $f^c_{q=12.8} = 0.3732$) are set. The crossover-time $t_{\rm co} = 1.6268$ and the fit interval are marked by vertical black lines.

	$N = 64$	$N = 32$	$N = 16$	$N = 8$	$N = 4$
b^{fit}	0.595253	0.616997	0.598863	0.571892	0.546314
a	0.315065	0.320868	0.316044	0.308580	0.301164
λ	0.727482	0.714315	0.725292	0.741670	0.757234
γ	2.4270	2.3686	2.4170	2.4946	2.5754

Table 4.5: b^{fit} obtained by fitting by fitting $\phi_{q=6.9}(t)$ for each chain length according to Eq. (4.14). For each chain length the lowest temperature which still obeys the TTSP is used ($N = 64 : T = 0.44$, $N = 43 : T = 0.44$, $N = 16 : T = 0.43$, $N = 8 : T = 0.42$, $N = 4 : T = 0.40$). The values of λ and a are obtained by exploiting the relation given in Eq. (4.15). γ is calculated by inserting b^{fit} and a in Eq. (4.16).

4.2.4 Analysis of T_{c}

In this paragraph we determine the critical temperature defined within the framework of the mode-coupling as a function of the chain length. We proceed as follows: First we use b^{fit} determined for each chain length to calculate λ and a. To this end, we exploit the relation between a, b and λ [11] given by

$$\lambda = \frac{\Gamma(1-a)^2}{\Gamma(1-2a)} = \frac{\Gamma(1+b)^2}{\Gamma(1+2b)} \qquad (1/2 \leq \lambda < 1) \; . \tag{4.15}$$

The calculated a and the determined b^{fit} enables us then to calculate γ [11] by using

$$\gamma = \frac{1}{2a} + \frac{1}{2b} \quad (\gamma > 1.765) \; . \tag{4.16}$$

Using this so obtained γ enables us to determine T_{c} by fitting the α relaxation times within the temperature range where the TTSP holds.

During our simulation procedure we continuously (in $\Delta T = 0.01$ steps) cooled down the considered system in the NpT ensemble (see section 2.5.2). Due to finite simulation resources we did not simulate for each temperature a trajectory also in the NVT ensemble. In order to increase the quality of the fit that we undertake to determine T_{c}, we added a few data points from NpT simulation runs. (We added following relaxation times τ_{q^*} determined for $\phi_{q=6.9}(t)$, which are obtained in the NpT ensemble: $N = 32$: $T = 0.46$; $N = 16$: $T = 0.45, 0.46$; $N = 8$: $T = 0.43, 0.45, 0.46$; $N = 4$: $T = 0.41, 0.42, 0.43$.) These trajectories are also equilibrated, but simulated in the NpT ensemble. This procedure was justified by comparing $\phi_{q=6.9}(t)$ calculated within the NpT and NVT ensemble for temperatures where both data are accessible.

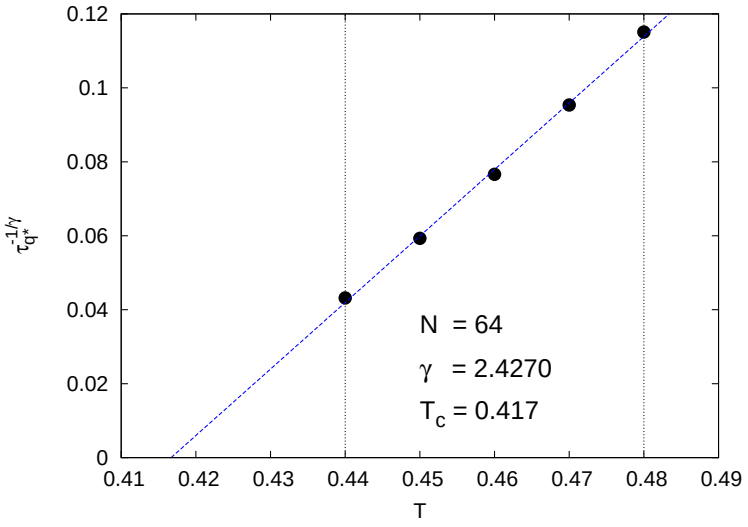

Figure 4.18: $N = 64$: α-relaxation times for $T = 0.44, 0.45, 0.46, 0.47, 0.48$ at $q = 6.9$. γ calculated from b^{fit} and a using Eq. (4.16). The α relaxation times for $\phi_{q=6.9}(t)$ (determined by the procedure described in section 4.2.1) are fitted according to $f(x) = A(x - T_c)$ where A and T_c are fit parameters.

The minor differences, which were noticed between $\phi_{q=6.9}(t)$ calculated within the NpT and NVT ensembles, seem to appear due to the poorer statistics we have for the NpT data. The influence on the determined relaxation time is small and does not influence the accuracy of the fit.

Finally we determine T_c by fitting the α relaxation time using following relation [11]

$$t'_\sigma = \frac{t_0}{|\sigma|^\gamma} , \tag{4.17}$$

which we use in the following form

$$(t'_\sigma)^{-\frac{1}{\gamma}} = a(T - T_c) . \tag{4.18}$$

In this way we are able to fit $(t'_\sigma)^{-\frac{1}{\gamma}}$ by using a linear fit.

In Fig. 4.18 we depict the fit result for $N = 64$, where we use a fit range of $T = 0.44 - 0.48$. Figure 4.19 shows the fit result for $N = 32$. In the case of $N = 32$ we use two different fit intervals, as it is not clear to which temperature the TTSP is still obeyed (cf. section 4.2.1). The values for T_c which are obtained are then averaged. Figures 4.20 - 4.22 show the fit results for chain length $N = 16, 8, 4$.

In Table 4.6 an overview over the so determined values for T_c is given.

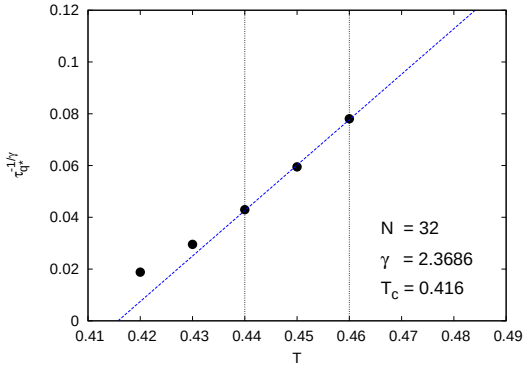

$N = 32$: α-relaxation times for $T = 0.42, 0.43, 0.44, 0.45, 0.46$ at $q = 6.9$.

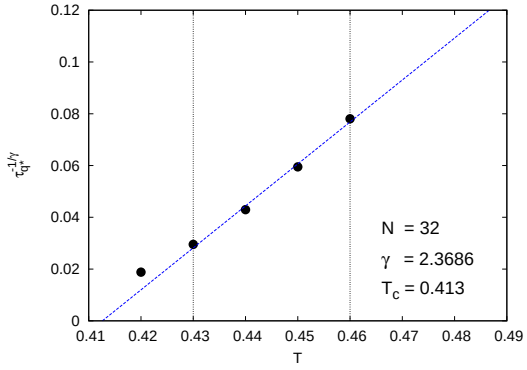

$N = 32$: α-relaxation times for $T = 0.42, 0.43, 0.44, 0.45, 0.46$ at $q = 6.9$. In contrast to the left figure a different lower bound for the fit interval is used ($T = 0.43$).

Figure 4.19: γ calculated from b^{fit} and a using Eq. (4.16). The α relaxation times for $\phi_{q=6.9}(t)$ (determined by the procedure described in section 4.2.1) are fitted according to $f(x) = A(x - T_c)$ where A and T_c are fit parameters.

	$N = 64$	$N = 32$	$N = 16$	$N = 8$	$N = 4$
T_c	0.417	0.415	0.409	0.401	0.382

Table 4.6: T_c obtained by fitting corresponding α relaxation times according to Eq. (4.18).

4.2.5 Chain length dependence of T_c, b, a, γ and λ

After we determined T_c and other mode-coupling theory related quantities like a, b, γ and λ we ask the question if these quantities also show some chain length dependency that can be treated like in the case of the density ρ (cf. section 3.1).

We start with T_c: In a first step we plot T_c as a function of the chain length. As this plot seems to follow a power law we fit according to $f(x) = Ax^{\alpha} + B$. From this fit we get for the exponent α a value close to minus unity: $\alpha = -1.02583$ (see Fig. 4.23). For this reason it seems to be appropriate to linearize T_c by plotting it as a function of the reciprocal chain length $1/N$, which is shown in Fig. 4.24. This functional dependence of T_c on $1/N$ — which is similar to the $1/N$-dependence of the density ρ (cf. section 3.1) — seems to be explainable also by chain end effects.

The fact that T_c can be linearized as a function of $1/N$ rises the question if

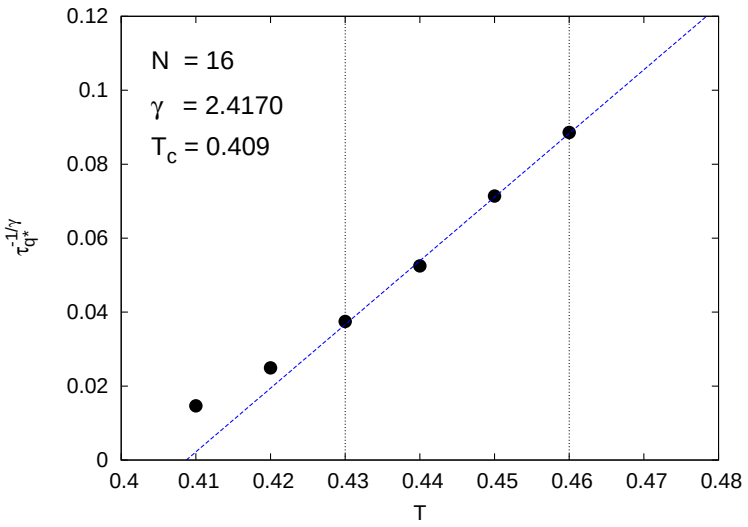

Figure 4.20: $N = 16$: α-relaxation times for $T = 0.41, 0.42, 0.43, 0.44, 0.45, 0.46$ at $q = 6.9$. The α relaxation times for $\phi_{q=6.9}(t)$ (determined by the procedure described in section 4.2.1) are fitted according to $f(x) = A(x - T_c)$ where A and T_c are fit parameters. The fit interval is denoted by black vertical lines.

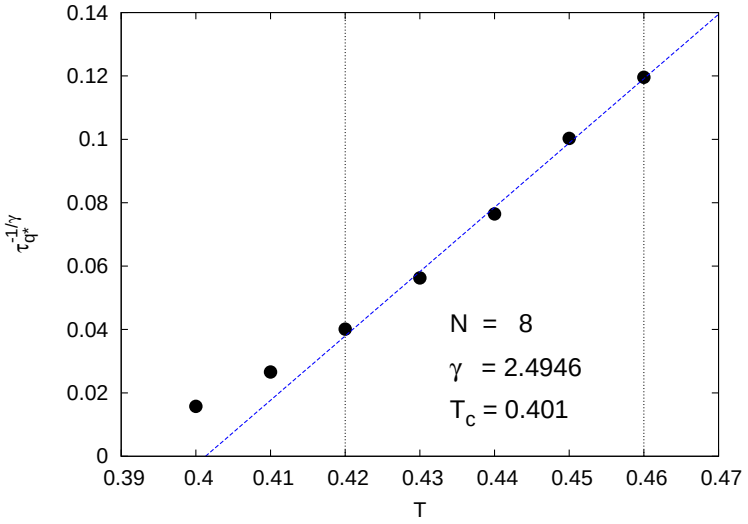

Figure 4.21: $N = 8$: α-relaxation times for $T = 0.40, 0.41, 0.42, 0.43, 0.44$ at $q = 6.9$. The α relaxation times for $\phi_{q=6.9}(t)$ (determined by the procedure described in section 4.2.1) are fitted according to $f(x) = A(x - T_c)$ where A and T_c are fit parameters. The fit interval is denoted by black vertical lines.

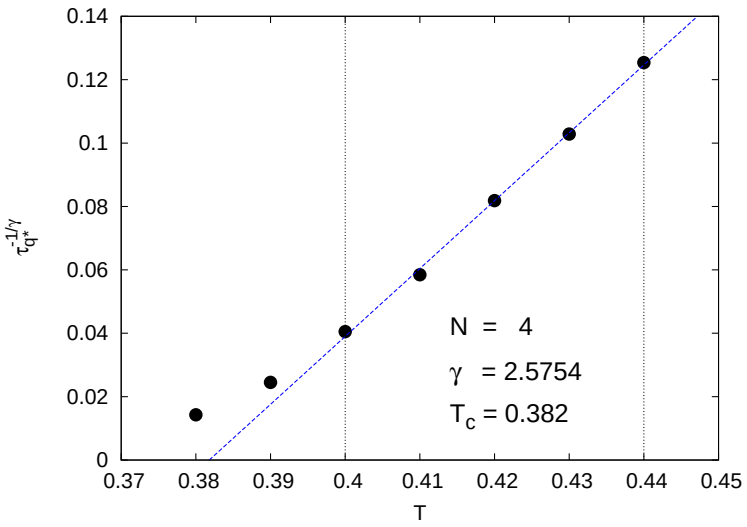

Figure 4.22: $N = 4$: α-relaxation times for $T = 0.38, 0.39, 0.40, 0.41, 0.42, 0.43, 0.44$ at $q = 6.9$. The α relaxation times for $\phi_{q=6.9}(t)$ (determined by the procedure described in section 4.2.1) are fitted according to $f(x) = A(x - T_c)$ where A and T_c are fit parameters. The fit interval is denoted by black vertical lines.

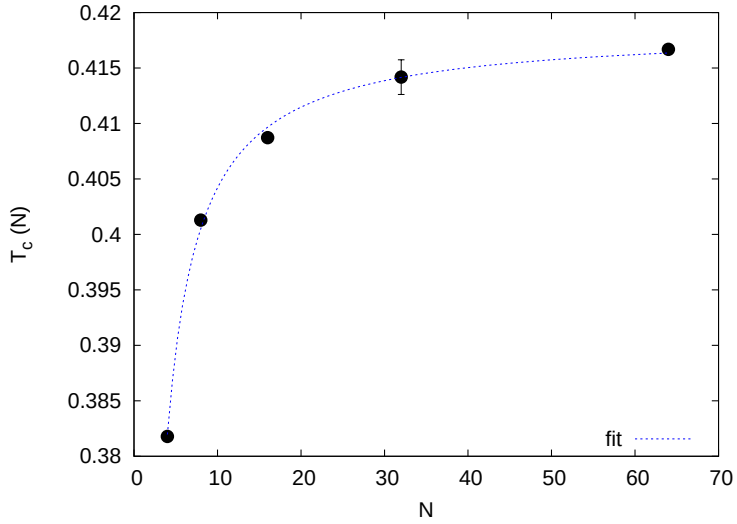

Figure 4.23: T_c as a function of the chain length N. The error bar for $N = 32$ indicates the error due to the usage of different fit intervals to obtain T_c by fitting the α relaxation time. The blue line indicates a fit according to $f(x) = Ax^{\alpha} + B$. Values obtained by fitting: $A = -0.151402$ $B = 0.418476$ $\alpha = -1.02583$

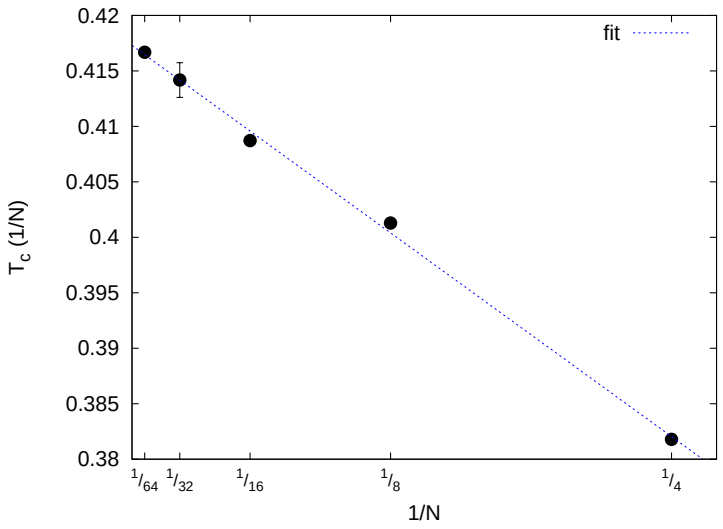

Figure 4.24: T_c as a function of the reciprocal chain length $1/N$. The error bar for $N = 32$ indicates the error due to the usage of different fit intervals to obtain T_c by fitting the α relaxation time. The blue line denotes a linear fit given by $f(x) = Ax + B$ with $A = -0.146914$, $B = 0.418765$.

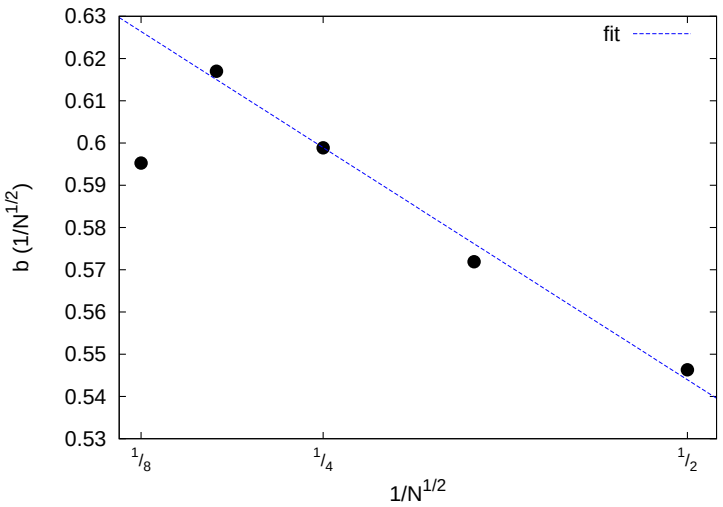

Figure 4.25: b as a function of the reciprocal value of the square root of the chain length $1/\sqrt{N}$. The blue line denotes a linear fit given by $f(x) = Ax + B$ with $A = -0.21982$, $B = 0.653877$.

the other MCT related quantities like b, a, γ and λ do also show such a behavior. Consequently we proceed with b: Here it is not so obvious whether or not there is a simple underlying scaling law according to which the chain length dependence of b can be rescaled to obtain a linear behavior of the resulting plot. By comparing the numerical values for b^{fit} one finds that there is a trend (see Table 4.5): Starting with the chain length of $N = 4$ the values for b^{fit} increase with growing chain length except for the longest chain length of $N = 64$. The reason why especially the longest chain length shows a deviation from this trend is not clear. We will come back to this point later on.

We then try to linearize b by rescaling the dependence on N while neglecting the value for $N = 64$. We find that this is possible by rescaling with $\frac{1}{\sqrt{N}}$. By proceeding in the same way for the other MCT related quantities a, γ and λ we find the same scaling behavior. Which means that the N dependence of these quantities can comparatively well linearized by rescaling with $\frac{1}{\sqrt{N}}$.

Why does $N = 64$ deviate from the trend? The question of why b^{fit} for $N = 64$ deviates from the trend showed by the other chain lengths is not clear so far. A possible explanation could be given by the fact that the chain length of $N = 64$ approaches the value for which entanglement effects are expected for this kind of model [43]. Another point which should be mentioned is the influence of the employed fit interval when fitting according to Eq. (4.14). As already mentioned the fit results depend also on this hidden fit parameter. This effect could be for some chain length more pronounced than for others depending on which amount of the late β relaxation is captured by the fit. However, it is rather complicated to determine the absolute influence of the employed fit interval.

Although there is some uncertainty for the b^{fit} values, the chain length dependence of b^{fit} seems to be quite robust and show a non monotonic behavior. Longer chain lengths have to be studied to check if b^{fit} continues to decrease or settle.

4.3 Analysis of the q-dependence of the α relaxation time

In the last section we exploited the time-temperature superposition principle to determine the range of the ideal mode-coupling theory. Therefore we use the cri-

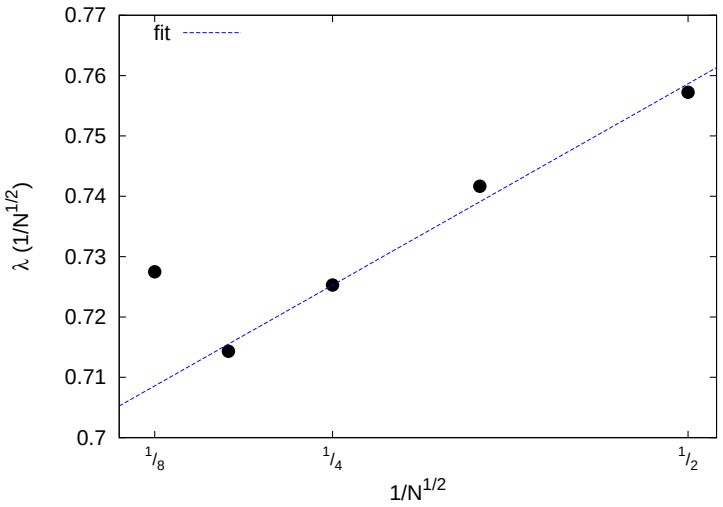

Figure 4.26: λ as a function of the reciprocal value of the square root of the chain length $1/\sqrt{N}$. The blue line denotes a linear fit given by $f(x) = Ax + B$ with $A = 0.133498$, $B = 0.691897$.

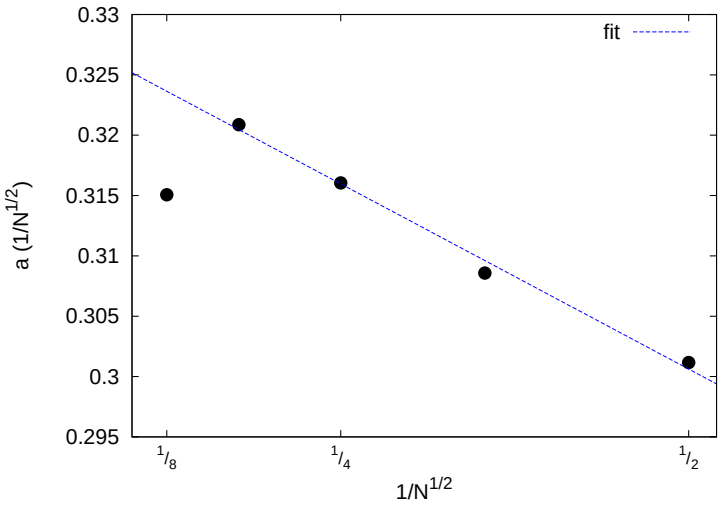

Figure 4.27: a as a function of the reciprocal value of the square root of the chain length $1/\sqrt{N}$. The blue line denotes a linear fit given by $f(x) = Ax + B$ with $A = -0.061391$, $B = 0.331314$.

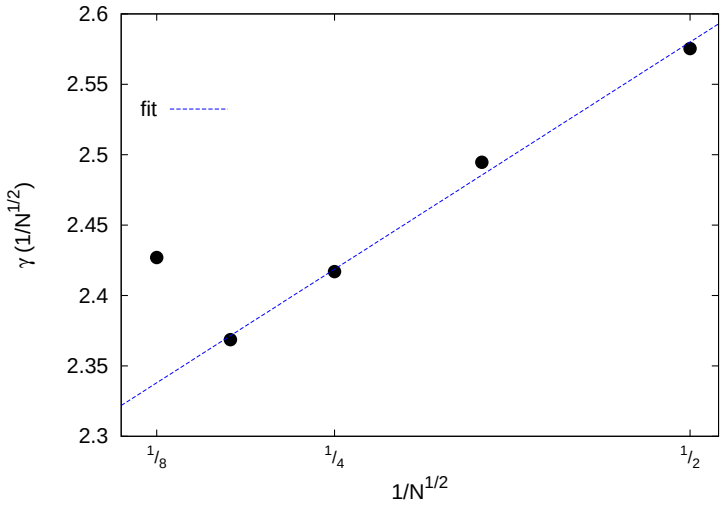

Figure 4.28: γ as a function of the reciprocal value of the square root of the chain length $1/\sqrt{N}$. The blue line denotes a linear fit given by $f(x) = Ax + B$ with $A = 0.645285$, $B = 2.25736$.

	$N = 64$	$N = 32$	$N = 16$	$N = 8$	$N = 4$
analyzed T	0.44	0.44	0.43	0.42	0.40
T_c	0.417	0.415	0.409	0.401	0.382
$T - T_c$	0.023	0.025	0.021	0.019	0.018

Table 4.7: Analyzed T corresponds to the temperatures from which the relaxation times are determined and depicted in Fig. 4.29 (bottom). These temperatures are contrasted with T_c, the critical temperature of the ideal MCT, which are determined in section 4.2.4). $T - T_c$ gives the relative distance of analyzed T to T_c.

terion $\phi_{q=6.9}(t)(\tau_{q^*}) = 0.1$ to define relaxation time τ_{q^*}. In this paragraph, we use the same threshold , namely 0.1, to determine relaxation times $\tau_{q=q'}$ for a q vector range of $q' = 1 - 8$ by using the criterion $\phi_{q=q'}(t)(\tau_{q=q'}) = 0.1$. Technically we proceed as before: First we calculate the coherent intermediate scattering function, and then we determine $\tau_{q=q'}$ by linear interpolation of $\phi_{q=q'}(t)$ between values close to 0.1. This procedure is carried out for all chain lengths for the temperatures of $T = 1.00$,$T = 0.50$ and $T - T_c \approx 0.02$ (see Fig. 4.29).

By comparing the result for the different temperatures we observe:

- For $T = 1$ the longest relaxation times are present for a q range from 3 – 5. Especially for $N > 8$ a broad peak region for this q interval can be observed.

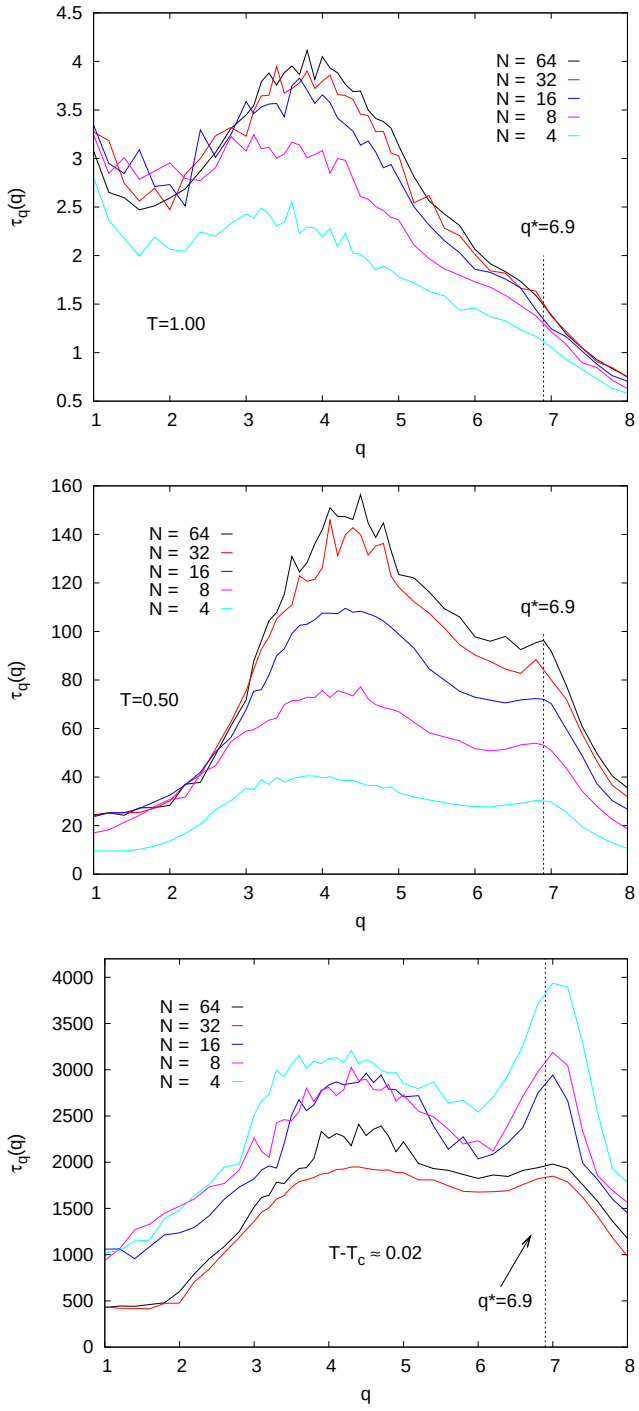

Figure 4.29: For $N = 64, 32, 16, 8, 4$ and temperatures $T = 1$ (top), 0.5 (middle) and $T - T_c \approx 0.02$ (bottom) the α relaxation times τ_q, defined by the condition $\phi_q(\tau_q) = 0.1$, are shown as a function of q. The black dashed line indicates the value $q^* = 6.9$, which is around the position of the peak of the static structure factor $S(q)$.

- For $T = 0.5$ all relaxation times increase compared to $T = 1$ but particularly for $3 < q < 5$ and for q values around the peak of the static structure factor $\sim S(q^*)$ (cf. section 3.3).

- For $T - T_c \approx 0.02$ all relaxation times further increase. As in the case of $T = 0.5$ especially for q values in the region of $3 < q < 5$ and $q \sim q^*$ the increase is very pronounced. As for the various N different relative distances to T_c are probed, we are able to observe how the relaxation times change in the approach of T_c. The temperatures from which the relaxation times are determined for $T - T_c \approx 0.02$ are summarized in Table 4.7. These temperatures correspond to the lowest temperatures for which the TTSP is still fulfilled (cf. section 4.2.1).

  Thereby it can be observed that the height of the peak around q^* is mainly influenced by the distance to T_c. The height of the peak in the q range of $3 < q < 5$ is influenced by the relative distance to T_c, but also depends on the chain length. This last point can be inferred by the comparison of the relaxation times for $N = 8$ and $N = 16$. Although the temperature for which the relaxation times for $N = 8$ are determined is closer to T_c compared to $N = 16$ — which is reflected by a larger value at the peak position at $q \sim q^*$ — the relaxation times for $3 < q < 5$ are comparable.

Chapter 5

Dynamics: Shear relaxation function and case study on finite-size effects

In this chapter we extend the discussion on the dynamics by considering two additional quantities which are the mean square displacement and the shear relaxation function [54]. By this extension we obtain a broader picture about the dynamics of our system, and we will also focus more on polymer effects.

Furthermore we carry out a case study on the effects of the finite simulation box size on the dynamics of a polymer system. This analysis concentrates on observable differences in dynamic correlation functions as a function of the temperature.

5.1 Shear relaxation function

In the previous chapter we focused on the intermediate scattering functions $\phi_q(t)$ to study the dynamics of the system under consideration. $\phi_q(t)$ reveals information about the system in terms of density fluctuations for one specific wavelength. Here we want to proceed in another way where we explore the cooperative viscoelastic properties of the system. To this end, we study the linear response of the system to an infinitesimal shear in the $q \to 0$ limit, i.e., we consider the shear relaxation function $G(t)$. This quantity can be introduced as the autocorrelation function of the microscopic stress $\sigma_{\alpha\beta}$, which is given by [55]

$$\sigma_{\alpha\beta} = \sum_{i=1}^{M} m v_{i,\alpha} v_{i,\beta} - \frac{1}{2} \sum_{i=1}^{M} \left(r_{i,\alpha} \frac{\partial U(\mathbf{r}^M)}{\partial r_{i,\beta}} + r_{i,\beta} \frac{\partial U(\mathbf{r}^M)}{\partial r_{i,\alpha}} \right), \tag{5.1}$$

where the components of the position $\mathbf{r}_i$ (the velocity $\mathbf{v}_i$) of monomer i $(= 1, \ldots, M)$ are denoted by $r_{i,\alpha}$ $(v_{i,\alpha})$, and total potential is denoted by U.

In terms of the microscopic stress, σ_{zx}, the shear relaxation function [5, 9] is given by

$$G(t) = \frac{1}{k_{\mathrm{B}}TV}\big\langle \sigma_{zx}(t)\sigma_{zx}(0)\big\rangle = \frac{1}{TV}\big\langle \sigma_{zx}(t)\sigma_{zx}(0)\big\rangle \;, \tag{5.2}$$

with T denoting the temperature and V the volume.

By this definition it can be understood that $G(t)$ can be employed as a measure to probe the viscoelastic properties of the whole system. The microscopic stress σ_{zx} takes the whole system into account.[1] In the systems under consideration the internal stress of the system is caused by the thermal movement of the monomers relative to one another. These movements cause local stresses which relax with time. This relaxation process is probed by the stress autocorrelation function, the shear relaxation function $G(t)$.

The analysis of the shear relaxation function is compared with the analysis of the mean square displacement. The mean square displacement (MSD) of all monomers (g_0) [11] can be defined by

$$g_0(t) = \frac{1}{M}\sum_{i=1}^{M}\Big\langle \Big[\mathbf{r}_i(t) - \mathbf{r}_i(0)\Big]^2\Big\rangle \;, \tag{5.4}$$

where M denotes the total number of monomers and $\mathbf{r}_i$ the position of monomer i. Additionally the mean square displacement of the center of mass of each chain (g_3) [11] can be defined as

$$g_3(t) = \frac{1}{n}\sum_{i=1}^{n}\Big\langle \Big[\mathbf{R}_i(t) - \mathbf{R}_i(0)\Big]^2\Big\rangle \;, \tag{5.5}$$

where n denotes the total number of chains and $\mathbf{R}_i$ the position of the center of mass of chain i.

By this comparison we explore the connection between the collective behavior of the studied system — probed by $G(t)$ — and properties that characterize the system in an incoherent way — g_0.

We start our discussion with the chain length $N = 64$. In Fig. 5.1 we contrast $g_0(t)$ and $G(t)$. To put this discussion in relation to $\phi_q(t)$, on which we focused in the last chapter, we add $\phi_q(t)$. In order to improve the comparability among these quantities we also show $\phi_q(t)$ with both axes logarithmically scaled.

[1] By a Green-Kubo relation the shear relaxation function $G(t)$ is related to the shear viscosity

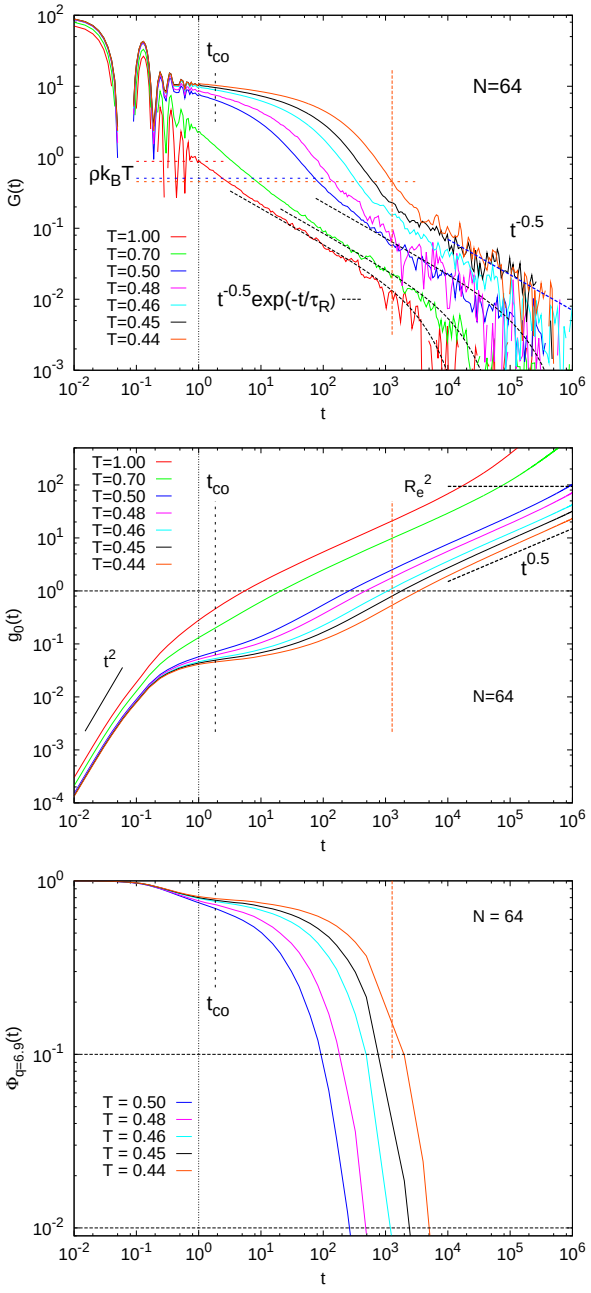

Figure 5.1: $N = 64$: Top: Shear relaxation function $G(t)$ versus time t; Center: Mean square displacement for all monomers $g_0(t)$ versus time t; Below: Coherent intermediate scattering function $\phi_{q=6.9}(t)$ versus time t. The black vertical dotted line marks $t = 1$. The black dashed line indicates the crossover time t_{co}, determined in section 4.2.3. The red vertical line denotes the start of the polymer regime for a temperature of $T = 0.44$ defined by $G(t) = \rho k_{\mathrm{B}} T$ (see text for details). The colored horizontal lines (top) indicate the value of $\rho k_{\mathrm{B}} T$ for $T = 1, 0.5, 0.44$.

The time interval can be naturally divided into four main regimes[2]:

- For very small times t the monomers move freely and follow a ballistic motion. For this reason the motion of the monomers shown in the MSD follow a power law $\propto t^2$ which seems to be observable. We write "seems" as this time regime stops as soon as the monomers "feel" their nearest neighbors, so the purely ballistic motion is only to a little extent visible. Rather, the ballistic regime already overlaps for small times t with the subsequent regime which starts when interaction between the monomers begin to determine the dynamics. Due to these interactions the monomers slow down which is observable by the fact that the slope of the MSD becomes weaker. In the shear relaxation function $G(t)$ the interactions with nearest neighbors results in the oscillations for times $t \lesssim 1$. Reference [54] suggests that these oscillations are due to interplay between the inertia of the monomer mass and the harmonic bond potential because they are absent in a Brownian dynamics simulation. A possible test of this idea within the framework of our MD simulation (with inertia) could employ a separation of the bond and non-bonded part. We then expect that the bonded contributions causes the oscillations in $G(t)$, whereas the non-bonded part relaxes without oscillations.

- For intermediate times — that means for times larger than 1 and smaller than the monomer relaxation time ${\tau_0}^3$ — the monomers are, for low enough temperatures, temporarily trapped by their neighboring monomers. (All the mode-coupling related analyses done in the last chapter took place in this time regime.) The idea that monomers are trapped by the surrounding monomers gives rise to the "cage effect" of the mode-coupling theory [37]. For a specific time window the dynamics of the monomers becomes partially or almost totally arrested. This time window is visible by the fact that the slope of the MSD is close to zero. As can be seen in Fig. 5.1 there is no clear signature of the "cage effect" anymore for high temperatures, i.e.,$T > 0.5$. In the shear

η [5]:

$$\eta = \int_0^\infty \mathrm{d}t\, G(t)\ . \tag{5.3}$$

[2]Actually all considered quantities are given as a function of time differences : All three studied functions are autocorrelation functions, which probe the system under consideration in terms of time differences between two specific times.

[3]τ_0 can be defined by $g_0(\tau_0) = 1$ [11].

relaxation function and in the coherent intermediate scattering function $\phi_q(t)$ this trapping is observable by a protracted decrease of the correlation.

- By means of the Rouse theory [26] we define the next time regime which starts as soon as the shear relaxation function $G(t)$ has reached the value of $\rho k_\mathrm{B}T$. This value sets the starting point of the Rouse theory. The shear relaxation can be expressed as the sum over all Rouse modes which relax exponentially with time given by $c_p(t) = \mathrm{e}^{-tp^2/\tau_\mathrm{R}}$ with τ_R denoting the Rouse time [26] and p the considered Rouse mode. The Rouse time can be related to the reciprocal monomer friction coeffiecient w by $\tau_\mathrm{R} \sim N^2 w^{-1}$, where N denotes the number of monomers in the chain. This leads to [75]

$$\begin{aligned} G(t) &= \tfrac{k_\mathrm{B}T\rho}{N} \textstyle\sum_{p=1}^{N-1} c_p^2(t) = \tfrac{k_\mathrm{B}T\rho}{N} \textstyle\sum_{p=1}^{N-1} \mathrm{e}^{-2tp^2/\tau_\mathrm{R}} \\ &\xrightarrow[N\gg 1]{\tau_0 \ll t \ll \tau_\mathrm{R}} \textstyle\int_0^\infty \mathrm{d}p\ \mathrm{e}^{-2tp^2/\tau_\mathrm{R}} \sim \tfrac{1}{\sqrt{wt}}\ . \end{aligned} \tag{5.6}$$

  For times on the order of the Rouse time all modes accept the one for $p = 1$ are assumed to have already relaxed. Therefore the long time limit is captured by an exponential cut off

$$G(t) \sim \mathrm{e}^{-t/\tau_\mathrm{R}}\ . \tag{5.7}$$

  Equations 5.6 and 5.7 can be combined to following approximation for the shear relaxation function [68]

$$G(t) \sim \frac{1}{\sqrt{t}}\,\mathrm{e}^{-t/\tau_\mathrm{R}}\ . \tag{5.8}$$

  The MSD shows for this time regime a transition to the sub-diffusive regime. In this regime the MSD follows a power law which is given by $\propto t^{0.5}$ for the chain length $N = 64$.[4] This power law behavior can also be observed in the shear relaxation function $G(t)$. Here it is given by $t^{-0.5}$ for $N = 64$.

- When the MSD reaches a value which corresponds to the mean-square end-to-end vector R_e^2 the dynamics starts to become purely diffusive and the MSD is $\propto t$. This time regime is only depicted for the highest temperatures. In this time regime the shear relaxation function is described by a final exponential decay which is not observable in our data. The reason for this is the missing statistics.

[4] For the shorter chain lengths under consideration effective power laws for the sub-diffusive regime can be found, e.g., for $N = 10$ a power law dependence of $t^{0.63}$ is observed [22].

Globally it can be said that the lower the temperature, the more extended the intermediate time regime. This means that lowering the temperature results in a slowing down of the monomer dynamics which seems to leave the dynamics occurring in subsequent regimes unchanged. The starting point of subsequent regimes is only shifted to later times.

N=64 In the upper plot of Fig. 5.1 the starting point of the "polymer regime" is marked for $T = 0.44$ by a vertical red line (corresponding to the color in which $G(t)$ is depicted for this temperature). By the term "polymer regime" we understand times t for which $G(t) < \rho k_{\mathrm{B}} T$. A dotted black vertical line indicates the starting point of the "monomer regime" where the crossover time t_{co} (cf. section 4.2.3) is indicated by a dashed black line. The term "monomer regime" refers to times for which it holds $1 \lesssim t < t_{\mathrm{polymer}}$, where t_{polymer} is given by $G(t_{\mathrm{polymer}}) = \rho k_{\mathrm{B}} T$. The horizontal lines indicate the value of $\rho k_{\mathrm{B}} T$ for $T = 1.00, 0.50, 0.44$. The plot in the middle of Fig. 5.1 shows the corresponding $g_0(t)$. Here, as well as in the lower plot ($\phi_q(t)$) the just discussed time regimes are marked similarly. Additionally $g_0(t) = 1$ and $\phi_{q=6.9}(t)(t) = 0.1$ are marked.

Figure 5.1 shows that compared to $g_0(t)$ it is very demanding to obtain similar statistics for $G(t)$.

N=16 As in the discussion of $N = 64$ the mentioned time regimes are marked by horizontal lines (see Fig. 5.2). The values for $\rho k_{\mathrm{B}} T$ are marked for $T = 1, 0.5, 0.43$. Here $T = 0.43$ is chosen as it is the lowest temperature (for $N = 16$) for which the time temperature-superposition principle is still fulfilled (cf. section 4.2). Contrasting $G(t)$ with $g_0(t)$ and $\phi_q(t)$ results in a similar comparison as for $N = 64$. In contrast to $N = 64$ we have for $N = 16$ access to lower temperatures with respect to T_{c}. This extension of the temperature window to lower temperatures seems not to unveil additional effects. As stated above a lower temperature most prominently results in a prolongation of the monomer relaxation regime, which shifts the starting of the subsequent regimes to later times. $G(t)$ (and $\phi_q(t)$) show for temperatures below $T = 0.43$ an increase in the plateau value. Additionally $g_0(t) = 1$ and $\phi_{q=6.9}(t)(t) = 0.1$ are marked.

In contrast to $N = 64$ the shear relaxation function for $N = 16$ shows no clear signature of a power law (for $N = 4$ no power law can be observed, neither). For smaller chain length τ_{R} is comparatively small as $\tau_{\mathrm{R}} \propto N^2 w^{-1}$. Therefore with

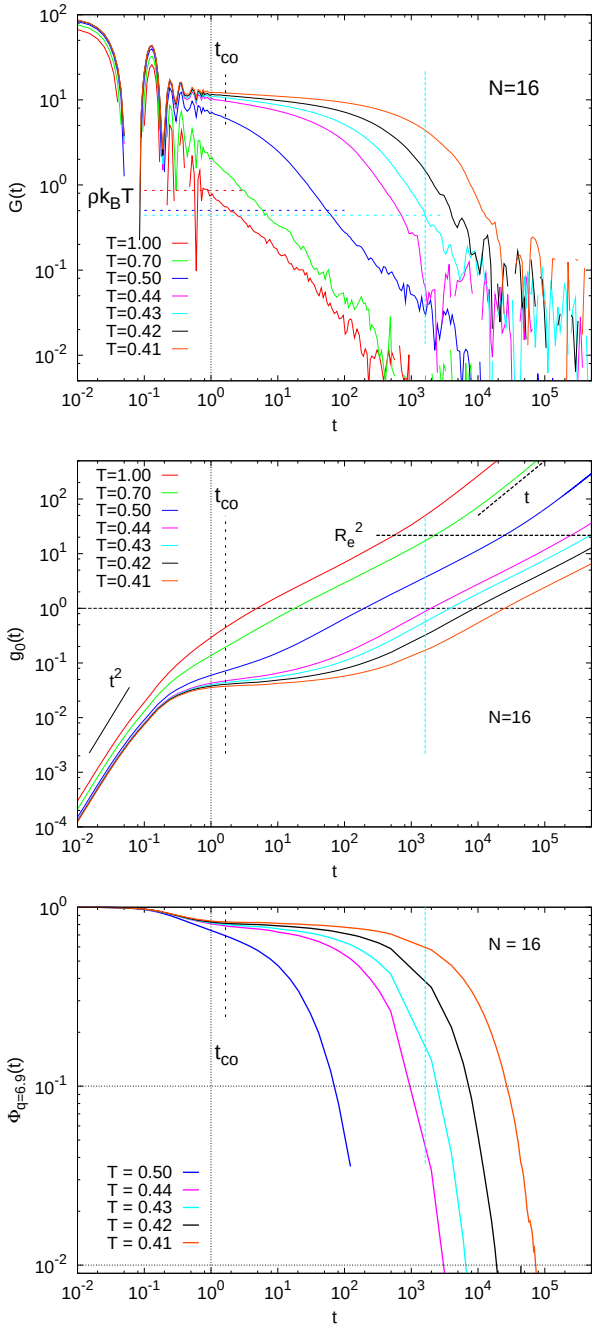

Figure 5.2: $N = 16$: Top: Shear relaxation function $G(t)$ versus time t; Center: Mean square displacement for all monomers $g_0(t)$ versus time t; Bottom: Coherent intermediate scattering function $\phi_{q=6.9}(t)$ versus time t. The black vertical dotted line marks $t = 1$. The black dashed line indicates the crossover time t_{co}, determined in section 4.2.3. The light blue vertical line denotes the start of the polymer regime for a temperature of $T = 0.43$ (see text for details). The colored horizontal lines (top) indicate the value of $\rho k_{\mathrm{B}} T$ for $T = 1, 0.5, 0.43$.

decreasing chain length the power law regime is blurred by the exponential cut off (cf. Eq. (5.8)).

N=4 In Fig. 5.3 we show the corresponding results for chain length $N = 4$. The results obtained can be interpreted in a similar way as above. Here for $T = 0.40$ the start of the "polymer regime" is marked. $T = 0.40$ is the lowest temperatures that still fulfills the time-temperature superposition principle for $N = 4$. The values for $\rho k_{\mathrm{B}} T$ are marked for $T = 1, 0.5, 0.40$. For $N = 4$ we also have access to temperatures that are below the T_{c} of the ideal mode-coupling theory. Additionally $g_0(t) = 1$ and $\phi_{q=6.9}(t)(t) = 0.1$ are marked.

5.2 Polymer effects

In this section we shortly point to some aspects about polymer effects. The comparison above between the MSD and shear relaxation function revealed several similarities between these two correlation functions which are not seen to the same extent in the coherent scattering function $\phi_{q=6.9}(t)$. This could be because $q \approx 6.9$ probes local density fluctuations, and not the dynamics in the limit $q \to 0$, as the MSD or $G(t)$ do. In this limit, and for times longer than the α-relaxation time, one would expect polymer effects to determine the dynamics of the melt [26, 68]. Therefore we discuss $\phi_q(t)$ for lower q values, down to the smallest q value accessible in our simulation which is given by $q_{\mathrm{min}} = \frac{2\pi}{l_{\mathrm{box}}}$, where l_{box} denotes the length of the simulation box.

Figure 5.4 compares the shear relaxation function $G(t)$ with $\phi_{q=q_{\mathrm{min}}}(t)$. For $N = 64$, q_{min} is given by $q \approx 0.27$.[5] We clearly observe that for small times $\phi_{q=q_{\mathrm{min}}}(t)$ also shows oscillations like the shear relaxation function. But for $\phi_q(t)$ these oscillations are related to damped sound waves (precursor of the hydrodynamic Brillouin spectrum [9]). They are fully developed for $\phi_{q=q_{\mathrm{min}}}(t)$ for $t \sim t_{\mathrm{co}}$ so that the non-ergodicity parameter f_q^{c} cannot be read off, contrary to larger wave vectors or to $G(t)$.

These oscillations blur the beginning of the β-relaxation at low T. However, a further interesting feature becomes visible for $\phi_q(t) \lesssim 10^{-2}$: At these late times, an

[5] As we equilibrate our systems at constant pressure and fix in a subsequent production run the simulation box size to the average volume from the equilibration run the box length slightly decreases with decreasing temperature. Therefore q_{min} is only given by a value close to $q \approx 0.27$.

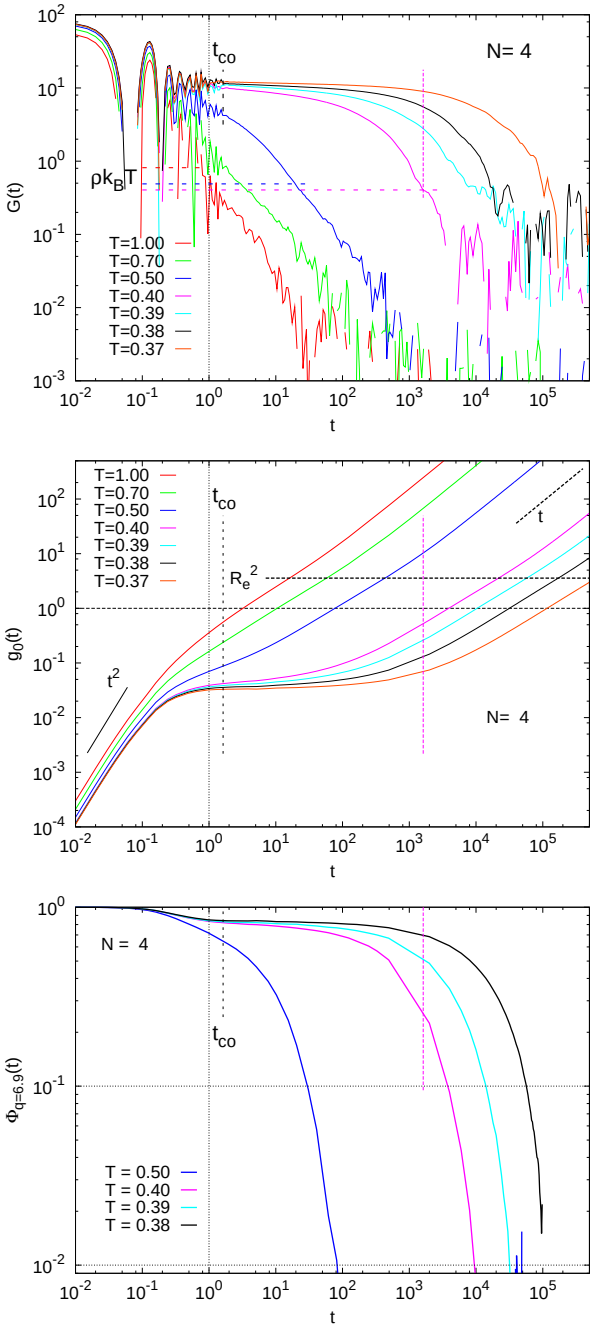

Figure 5.3: $N = 4$: Top: Shear relaxation function $G(t)$ versus time t; Center: Mean square displacement for all monomers $g_0(t)$ versus time t; Bottom: Coherent intermediate scattering function $\phi_{q=6.9}(t)$ versus time t. The black vertical dotted line marks $t = 1$. The black dashed line indicates the crossover time t_{co}, determined in section 4.2.3. The magenta vertical line denotes the start of the polymer regime for a temperature of $T = 0.40$ (see text for details). The colored horizontal lines (top) indicate the value of $\rho k_{\mathrm{B}} T$ for $T = 1, 0.5, 0.40$.

apparent power $t^{-0.5}$ shows up for all T.

In Fig. 5.5 we show that such a power law behavior is only observable for the lowest q values, $q \lesssim 3q_{\min}$. For q values above this value the signature of this power law is not well pronounced so that it cannot be observed anymore. The lower plot of Fig. 5.5 shows that the power law behavior is also restricted to chain lengths that are close to the entanglement length (it is barely visible for $N = 16$) [43]. Tentatively, we attribute this (apparent) power law to a polymer effect. That such effects could also determine $\phi_q(t)$ is suggested by the dynamic Random Phase Approximation [29] which expresses the time dependence of $\phi_q(t)$ fully in terms of the dynamic polymer form factor $F(q,t)$. In Laplace space this relation reads

$$\hat{\phi}_q(z) = \frac{\hat{w}(q,z)/w(q)}{1 + \frac{w(q)}{S(0)}[1 - z\hat{w}(q,z)/w(q)]} \,, \tag{5.9}$$

where z denotes the conjugate Laplace variable of t and $S(0)$ is zero wave vector limit of $S(q)$ (cf. section 3.3 for a definition of S and w). It would be interesting to apply Eq. (5.9) quantitatively to the simulation data to test whether it can account for the apparent power law $t^{-0.5}$.

5.3 Time-temperature superposition of the shear relaxation function

In section 4.2.1 we showed that the intermediate scattering function can be rescaled according to the α relaxation time τ_{q^*}. Here we investigate if such a rescaling is also possible for the shear relaxation function. The upper plot of Fig. 5.6 shows that the MSD $g_0(t)$ can be well rescaled according to the diffusion constant D (this result is known see e.g. [37] and references therein). D is determined from the long time evolution of the MSD $g_3(t)$ of the center of mass of the chains by employing $g_3(t) \propto 6Dt$. As $G(t)$ has similarities with both the intermediate scattering function and $g_0(t)$ (cf. section 5.1), it is a priori not clear whether $G(t)$ could be rescaled by τ_{q^*} or by D. Therefore, we test both possibilities after normalizing $G(t)$ by $\rho k_{\mathrm{B}}T$. (This normalization is suggested by polymer theory [26].)

The center plot of Fig. 5.6 shows $G(t)$ rescaled according to the diffusion constant D. For intermediate times ($10^{-5} \lesssim t \lesssim 10^{-3}$) this rescaling does not work well. For times $t \gtrsim 10^{-3}$ we cannot validate the quality of the scaling due to the noise of the data.

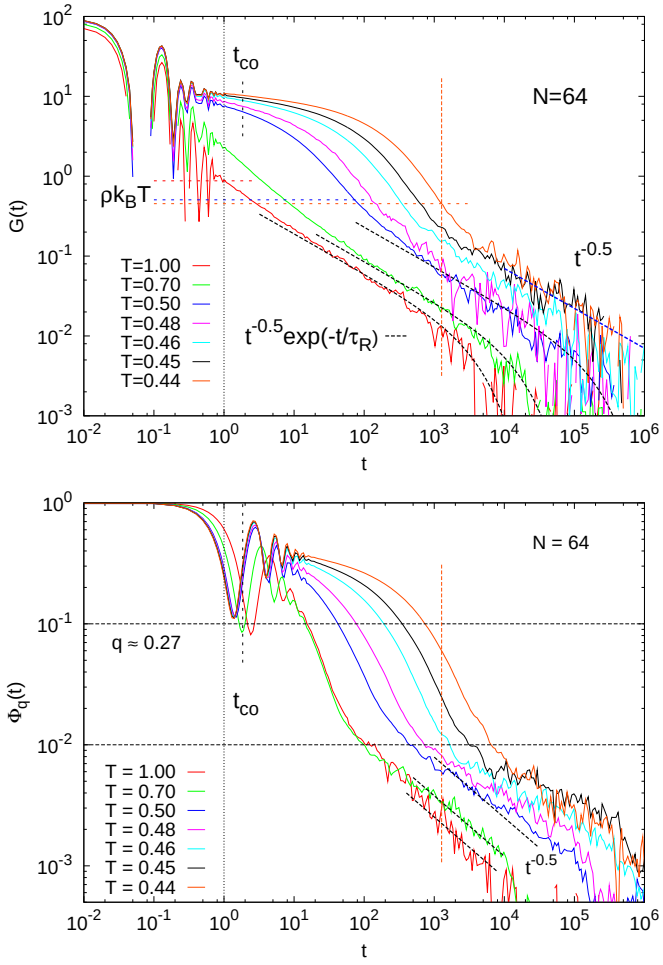

Figure 5.4: $N = 64$: Top: Shear relaxation function $G(t)$ versus time t; a behavior $\propto \frac{1}{\sqrt{t}}\,\mathrm{e}^{-t/\tau_\mathrm{R}}$ is indicated by black dashed lines. The colored horizontal lines indicate the value of $\rho k_\mathrm{B}T$ for $T = 1, 0.5, 0.44$. Bottom: $\phi_{q=q_\mathrm{min}}(t)$ versus time t for $T = 0.44, 0.45, 0.46, 0.48, 0.50, 0.70, 1.00$. A behavior $\propto t^{-0.5}$ is indicated by black dashed lines.

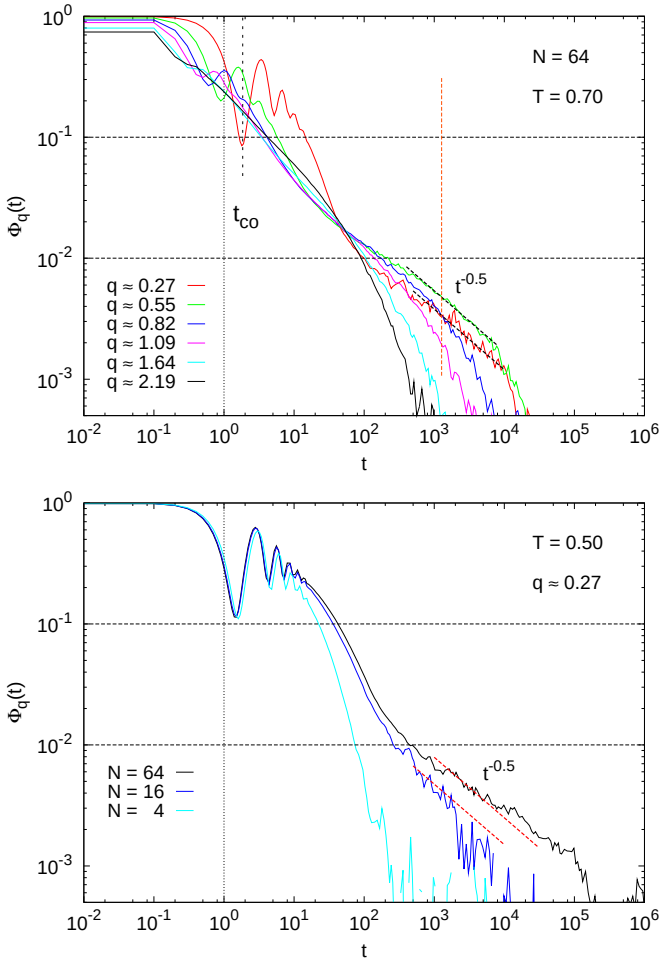

Figure 5.5: Top: For $N = 64$ and $T = 0.70$ $\phi_q(t)$ is shown for $q = 0.27, 0.55, 0.82, 1.09, 1.64, 2.19$. A power law $\propto t^{-0.5}$ is indicated by black dashed lines. Bottom: $\phi_{q=q_{\min}}(t)$ for $N = 64$ (black), $N = 16$ (dark blue) and $N = 4$ (light blue) for a temperature of $T = 0.50$. For $N = 64$ and $N = 16$ a power law $\propto t^{-0.5}$ is indicated by red dashed lines.

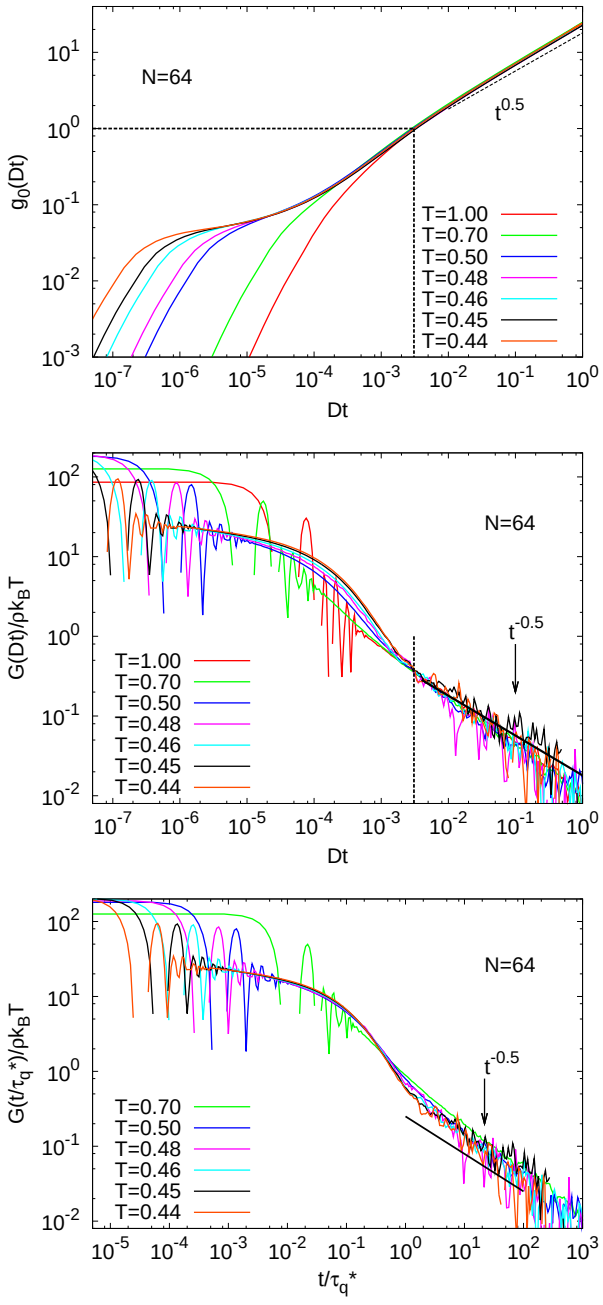

Figure 5.6: $N = 64$: Top: $g_0(t)$ rescaled according to the diffusion constant D. Center: $G(t)$ rescaled according to the diffusion constant D. Bottom: $G(t)$ rescaled according to the α relaxation time τ_{q^*} determined $\phi_{q=6.9}(\tau_{q^*}) = 0.1$.

In the lower plot of Fig. 5.6 $G(t)$ is rescaled according to the α relaxation time τ_{q^*}. Here, for temperatures $T \lesssim 0.5$, the rescaling works well for (rescaled) times $t \lesssim 0.5$ and $T < 0.7$. For times $t \gtrsim 0.5$ the data collapse is comparable in quality to that of the middle figure, provided $T < 0.7$. In summary, the present data suggest that the TTSP of $G(t)$ is better fulfilled with τ_{q^*} than with D. However, this issue certainly requires further investigation to arrive at a definitive conclusion. The statistics in the polymer regime should be improved. There could be the interesting situation that the "monomer regime" can be rescaled with τ_{q^*}, whereas the polymer regime is rescaled with $D \sim \tau_{\mathrm{R}}^{-1}$, as expected from polymer theory.

5.4 Case study on finite size effects

In this section we compare the effect of the finite simulation box size on the dynamics of a polymer system. Thereto we consider two systems that are simulated at a pressure $p = 1$ with chains of chain length $N = 10$, and consisting of $M = 1000$ and $M = 8000$ monomers.[6]

It is known that so-called finite size effects could affect the dynamics of colloidal systems. The explanation can be summarized by the following argument: Due to the finite box size only a finite number of possible relaxation modes are accessible. For this reason smaller system sizes might exhibit a slower dynamical relation (see e.g. [45]).

We study the influence of the different simulation box sizes by means of the coherent intermediate scattering function $\phi_q(t)$ and by the mean square displacement of all monomers $g_0(t)$.

Coherent intermediate scattering function In Figs. 5.7 and 5.8 the obtained results for $\phi_q(t)$ for $q = 4, 6.9, 9.5, 12.8$ are shown. As an overall observation we can state that the smaller system exhibits a slower relaxation for the depicted temperatures below $T = 1$. For $T = 1$ no differences in the relaxation of $\phi_q(t)$ are noticeable. For lower temperatures the differences in the relaxation process exhibited by $\phi_q(t)$ seem to become more pronounced on cooling and reach a maximum at $T \approx 0.45$.

In Table 5.1 we display the thermodynamical data of the studied systems. The values for the density and the pressure for both system sizes is in good accordance.

[6] The same model is employed as for the systems studied before.

	$T = 0.44$	$T = 0.45$	$T = 0.46$	$T = 0.47$	$T = 0.50$	$T = 1.00$
$\rho(M = 1000)$	1.0447	1.0434	1.0406	1.0374	1.0290	0.90970
$\rho(M = 8000)$	1.0450	1.0425	1.0397	1.0372	1.0291	0.90965
$p(M = 1000)$	0.969928	1.00963	1.03397	1.01163	0.987964	0.997480
$p(M = 8000)$	0.992614	1.00205	0.998268	1.00165	0.999094	0.999208

Table 5.1: Density ρ and pressure p as a function of temperature T for the system sizes of $M = 1000$ and $M = 8000$. Values are given for $T = 1.00, 0.50, 0.47, 0.46, 0.45, 0.44$. (For chain length $N = 10$ and pressure $p = 1$.)

The small discrepancies in the density and the pressure appears to be too weak to explain the different relaxation behavior of the two system sizes.

To compare the emerging differences shown by $\phi_q(t)$ for different q values in more detail we depict in Fig. 5.9 in the main figure the difference of the relaxation time for each q value. Using the relaxation time τ_q — defined as in the previous chapter by $\phi_q(\tau_q) = 0.1$ — we calculate the absolute difference of the relaxation times $\Delta\tau_q(T)$ by $\tau_{q,M=1000}(T) - \tau_{q,M=8000}(T)$, which is evaluated for each temperature and q value separately. We observe that $\Delta\tau_q(T)$ increases by lowering the temperature and reaches, for $q = 4$ and 6.9 a maximum value at $T = 0.45$. The inset of Fig. 5.9 shows the normalized difference of the relaxation times which is defined by $\Delta^*\tau_q(T) = (\tau_{q,M=1000}(T) - \tau_{q,M=8000}(T))/\tau_{q,M=8000}(T)$. We normalized by the relaxation time of the larger system, as the sampling of the larger system is closer to the thermodynamical limit. This depiction shows a clear maximum for all studied q values at the temperature of $T = 0.45$.

Mean square displacement We then proceed to the mean square displacement of all monomers and analyse if the difference in the structural relaxation, observed by $\phi_q(t)$, is also noticeable by this quantity. Additionally, the MSD probes the system on larger length scales.

In Fig. 5.10 the MSD of the two considered systems is shown for the temperatures of $T = 1, 0.50, 0.47, 0.46, 0.45, 0.44$. The evolution of the MSD shows for all temperatures for times $t > 10$ discrepancies between the two system sizes. For the lower temperatures, $T \leq 0.5$, these discrepancies become already obvious for times $t \approx 1$. The differences are most pronounced for the temperatures of $T = 0.46$ and $T = 0.45$, for which they reach, as in the case of the $\phi_q(t)$, a maximum.

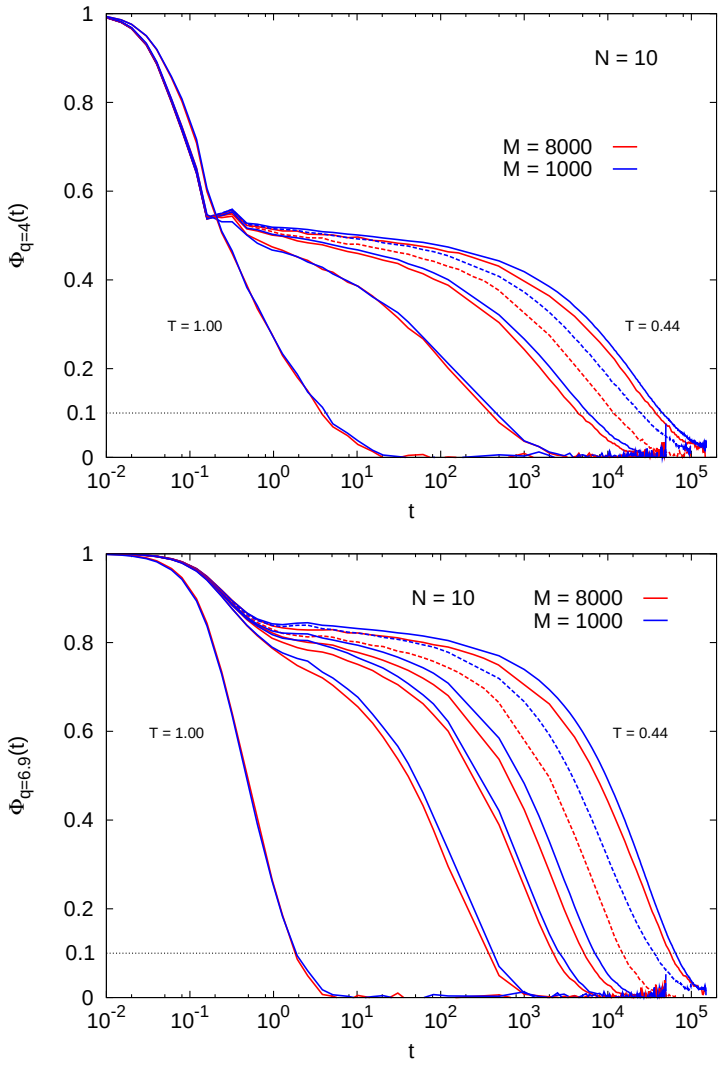

Figure 5.7: Comparison between two system sizes ($M = 1000$ and $M = 8000$) at pressure of $p = 1$ and a chain length of $N = 10$. Coherent intermediate scattering function $\phi_q(t)$ is depicted for $q = 4, 6.9$ for temperatures $T = 1.00, 0.50, 0.47, 0.46, 0.45, 0.44$ (from left to right). $\phi_q(t)$ for the system size $M = 8000$ is depicted in red and $\phi_q(t)$ for $M = 1000$ in blue. The smaller system shows a slower structural relaxation. $\phi_q(t)$ for $T = 0.45$ is depicted with dashed lines. This temperature corresponds to the critical temperature of the ideal mode-coupling theory [15]. The differences in the structural relaxation showed by the two system sizes increase with decreasing temperature. The value 0.1 is marked by a horizontal black dashed line. This value is used to determine a relaxation time τ_q by $\phi_q(\tau_q) = 0.1$.

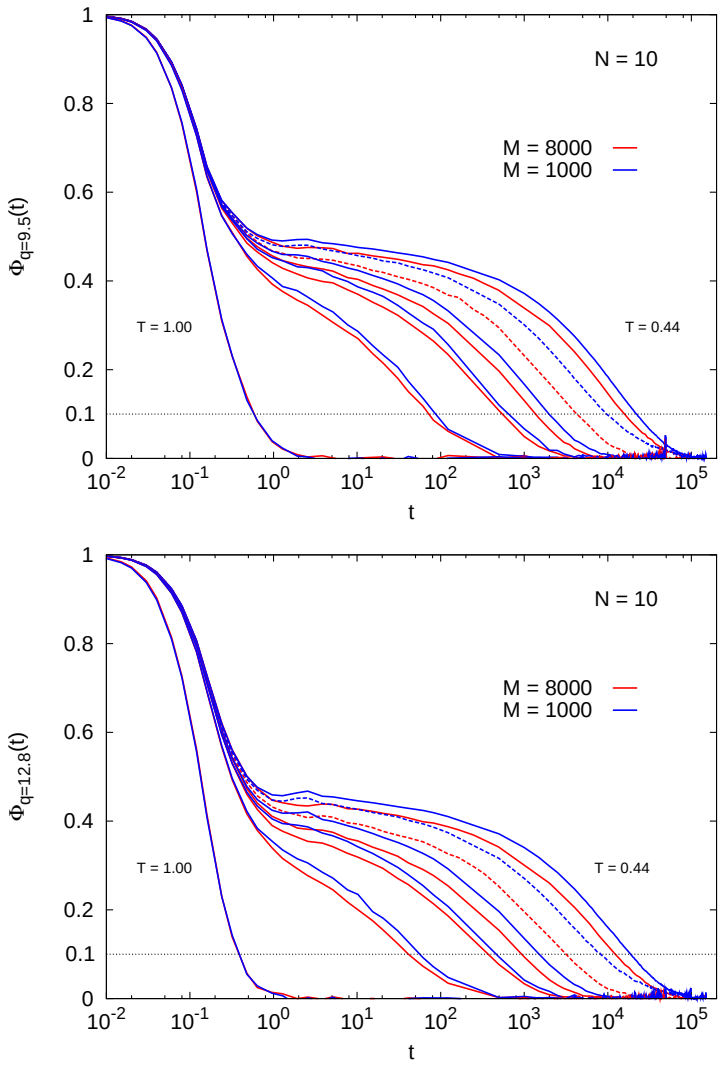

Figure 5.8: Comparison between two system sizes ($M = 1000$ and $M = 8000$) at pressure of $p = 1$ and a chain length of $N = 10$. Coherent intermediate scattering function $\phi_q(t)$ is depicted for $q = 9.5, 12.8$ for temperatures $T = 1.00, 0.50, 0.47, 0.46, 0.45, 0.44$ (from left to right). $\phi_q(t)$ for the system size $M = 8000$ is depicted in red and $\phi_q(t)$ for $M = 1000$ in blue. The smaller system shows a slower structural relaxation. $\phi_q(t)$ for $T = 0.45$ is depicted with dashed lines. This temperature corresponds to the critical temperature of the ideal mode-coupling theory [15]. The differences in the structural relaxation showed by the two system sizes increase with decreasing temperature. The value 0.1 is marked by a horizontal black dashed line. This value is used to determine a relaxation time τ_q by $\phi_q(\tau_q) = 0.1$.

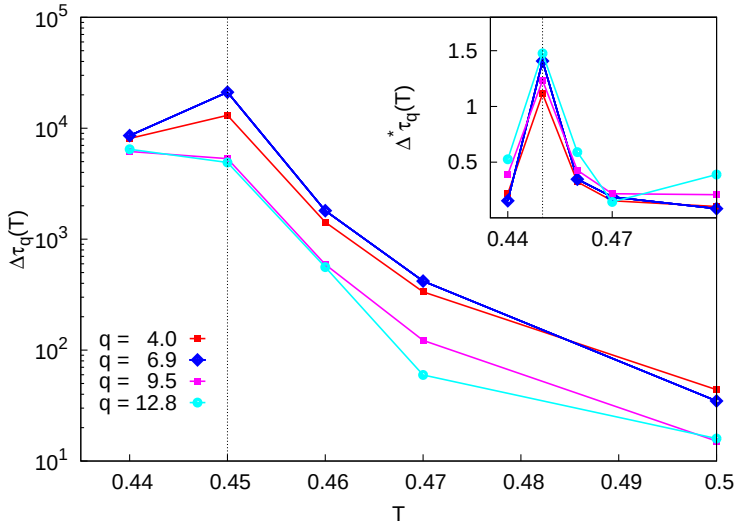

Figure 5.9: Comparison between two system sizes ($M = 1000$ and $M = 8000$) at pressure of $p = 1$ and a chain length of $N = 10$. Main figure: Depicted is the difference ($\Delta\tau_q$) between the relaxation times (determined by $\phi_q(\tau_q) = 0.1$) evaluated for $M = 1000$ and $M = 8000$ and $q = 4, 6.9, 9.5, 12.8$ as a function of temperature T. Inset: Depicted is the normalized difference ($\Delta^*\tau_q$) between the relaxation times (determined by $\phi_q(\tau_q) = 0.1$) evaluated for $M = 1000$ and $M = 8000$ and $q = 4, 6.9, 9.5, 12.8$ as a function of temperature T. It is normalized by the relaxation time of the larger system ($M = 8000$) for each considered temperature and q value.

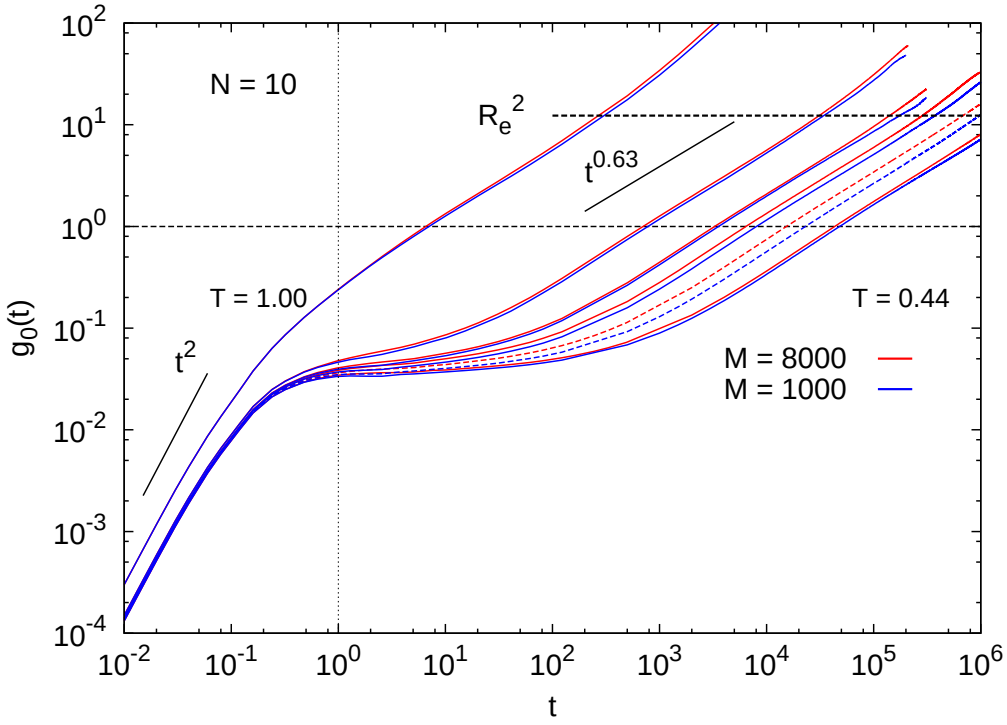

Figure 5.10: Comparison between two system sizes ($M = 1000$ and $M = 8000$) at pressure of $p = 1$ and a chain length of $N = 10$. Mean square displacement $g_0(t)$ for $T = 1.00, 0.50, 0.47, 0.46, 0.45, 0.44$ (from left to right). $g_0(t)$ for the system size $M = 8000$ is depicted in red and $g_0(t)$ for $M = 1000$ in blue. The smaller system shows a slower dynamics. $g_0(t)$ for $T = 0.45$ is depicted with dashed lines. This temperature corresponds to the critical temperature of the ideal mode-coupling theory [15].

Figure 5.11 shows the differences of the MSD normalized by the MSD of the larger system $\Delta g_0(t) = \frac{g_{0,M=8000}(t) - g_{0,M=1000}(t)}{g_{0,M=8000}(t)}$. At $t = 2.56$[7] $\Delta g_0(t)$ shows for all depicted temperatures a small peak. The reason for this occurring peak might be found in the sound wave propagation which couples to other modes at larger q and gives rise to an echo for these q values [42]. For the smaller system sound waves need lesser time to travel through the whole system. Therefore the effect on density fluctuations caused by sound waves in the two system could be different and finally result in a different evolution of the MSD in a time interval where this effect is most pronounced.

Especially we want to point to the observation that the MSD for $T = 0.46, 0.45$ shows a non monotonic behavior after this first peak, whereas the temperatures $T = 0.50, 0.47$ show only weak oscillations. The lowest temperature $T = 0.44$ also shows a non monotonic behavior, but only to a small extent when compared to the temperatures of $T = 0.46, 0.45$. In Fig. 5.12 we show another possible analysis of the difference observed in the MSD. Here the ratio of the MSD of the larger system compared to that of the smaller one is shown: $\Delta^* g_0(t) = \frac{g_{0,M=8000}(t)}{g_{0,M=1000}(t)}$. (The two considered ratios are related to each other by $\Delta g_0(t) = 1 - (\Delta^* g_0(t))^{-1}$.)

By this representation the different evolution of the "MSD ratio" for different temperatures becomes more obvious. For $T = 0.45$ we observe after the first peak a strong increase which then seems to saturate for times $t > 10^4$. A similar behavior is seen for $T = 0.46$ but less pronounced where the saturation begins earlier.

[7] The MSD for all system and temperatures is evaluated using the same sampling scheme for times $t \lesssim 200$. Therefore the position of the peak appears at the same time. A more detailed time sampling might show smaller deviations in the position of the peak for different temperatures.

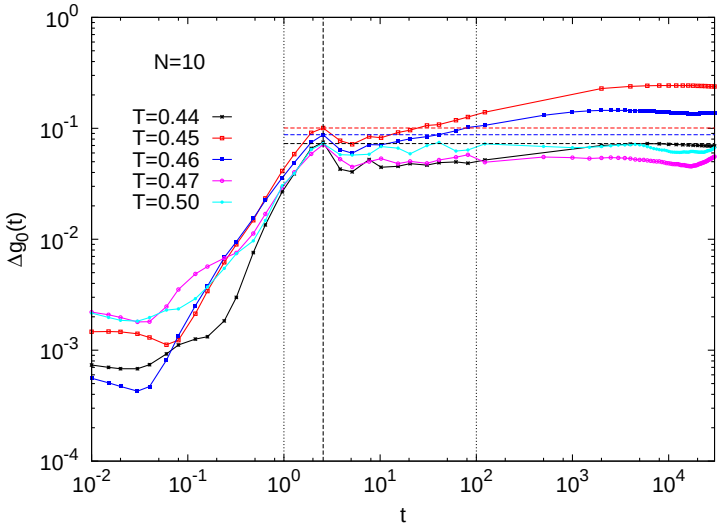

Figure 5.11: Comparison between two system sizes ($M = 1000$ and $M = 8000$) at pressure of $p = 1$ and a chain length of $N = 10$. The relative difference of the mean square displacement $\Delta g_0(t) = \frac{g_{0,M=8000}(t) - g_{0,M=1000}(t)}{g_{0,M=8000}(t)}$ is depicted for $T = 0.50, 0.47, 0.46, 0.45, 0.44$. The horizontal lines give the value of $\Delta g_0(t)$ at the peak position for $T = 0.45$ (red), $T = 0.46$ (blue) and $T = 0.44$ (black).

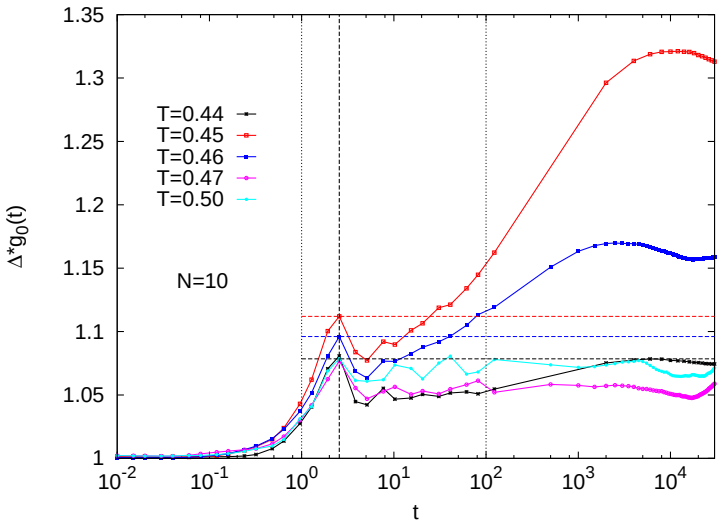

Figure 5.12: Comparison between two system sizes ($M = 1000$ and $M = 8000$) at pressure of $p = 1$ and a chain length of $N = 10$. The ratio of the mean square displacement $\Delta^* g_0(t) = \frac{g_{0,M=8000}(t)}{g_{0,M=1000}(t)}$ is depicted for $T = 0.50, 0.47, 0.46, 0.45, 0.44$. The horizontal lines give the value of $\Delta g_0(t)$ at the peak position for $T = 0.45$ (red), $T = 0.46$ (blue) and $T = 0.44$ (black).

Chapter 6

Summary and Outlook

By performing molecular dynamics simulation of a generic bead spring model we studied the structure, the conformational and structural relaxation, and the viscoelastic properties of glass-forming polymer melts. This study was mainly focussed on dynamic quantities as they reveal the most prominent features of these polymer melts: the protracted structural relaxation preceding the glass transition temperature. For the employed model we studied the influence of the chain length of the polymers on the dynamical and the static properties. The dynamics were mainly analyzed in the framework of the ideal mode-coupling theory [37].

Our work is the logical continuation and extension of two previous theses performed in the group. The work by M. Aichele studied bulk systems of short chains $N = 10$ at $p = 1.0$ [1, 4, 22]. That work performed almost ten years ago was restricted to systems of $1000 - 1200$ particles. The second work is the thesis of S. Peter [64–66] who used the same model to study the supercooled dynamics in thin films. As a reference, some bulk systems with $N = 64$ were studied at $p = 0$.

In the present work, we go beyond the previous work by using larger systems of 12288 particles and by studying systematically the chain length dependence of the supercooled dynamics using $N = 4, 8, 16, 32, 64$. The increased computer power makes it possible to equilibrate the systems down to the MCT critical temperature and for small chains even below. In the following, we summarize the main results and point out possible extensions of this work.

- We started with the analysis of the static properties. We investigated how the density evolves as a function of the chain length and temperature (see figures 3.1 and 3.3). Thereby we found that the evolution can be described as a function of the reciprocal chain length. A signature of this feature was also

observed in the static structure factor (cf. figures 3.6 and 3.7). It would be interesting if this observed behavior is still present for longer chains especially on cooling.

- We investigated how the effective bond length [79] evolves as a function of the temperature (cf. figures 3.14 – 3.16). We found that the effective bond length decreases on cooling the temperature. This counter-intuitive feature arises from the full flexibility of the employed model which is chemically not realistic. Therefore it would be interesting to continue the study by considering chemically more realistic models (like in [16]).

- The dynamics were studied in the framework of the ideal mode-coupling theory (MCT) [11, 37]. A first step was the examination of the temperature interval within which the time-temperature superposition principle (TTSP) is fulfilled as a function of the chain length (cf. figures 4.2 – 4.6). This was contrasted with the factorization theorem which was verified in the β regime (cf. figures 4.7 – 4.9). In summary the scaling in the β regime is possible even for temperatures for which the TTSP does not hold anymore.

- Thereafter we determined the critical temperature T_c of the ideal MCT as a function of the chain length (cf. figures 4.18 – 4.22). A chain length dependence of T_c which can be rescaled by $1/N$ was found (see figures 4.23 and 4.24). This is in contrast to the von Schweidler exponent b for which an effective scaling behavior with $1/\sqrt{N}$ was found for $N < 64$ (see Fig. 4.25). Future work could focus on longer chain lengths. Does b continue to decrease for $N > 64$ or does it converge to a constant value?

- The q-dependence of the α relaxation time was evaluated for a high and a medium temperature and close to T_c (see Fig. 4.29). It was observed that for the temperatures close to T_c the relaxation processes on the monomer level — as predicted by ideal MCT — are most pronounced. However, for higher temperatures relaxation processes on larger length scales are more pronounced.

- In comparison to the previous work, we consider as an additional quantity the shear relaxation function, and we are able to calculate the coherent intermediate scattering function with high resolution so that a long time tail, specific to polymers, becomes visible (cf. figures 5.1 – 5.4). By employing the shear relaxation function [54] the considered systems were studied on larger length

scales. It was found that upon cooling the monomer relaxation times increase which shifts the relaxation on length scales comparable to the polymer size to longer times. A similar behavior was observed also by analyzing the intermediate scattering function for the smallest q values accessible in the simulation (see Fig. 5.4). This study showed that significant polymer effects — which show a power law signature — become visible only for the smallest q values and the longest chains studied (cf. Fig. 5.5). This deserves a more detailed theoretical analysis.

- By rescaling the mean square displacement according to the diffusion constant an analogous scaling behavior as for the intermediate scattering function by rescaling according to the α relaxation time was found (cf. Fig. 5.6). For the shear relaxation function a scaling according to only one of these quantities does not lead to a completely satisfying result.

- In the last part we undertook a case study on finite size effects. To this end we compared two system sizes of a polymer system with a chain length $N = 10$. This comparison focussed on the coherent intermediate scattering function (cf. figures 5.7 and 5.8) and the mean square displacement (cf. Fig. 5.10). These functions measured for both systems were compared to each other for temperatures around T_c of the ideal MCT (cf. coherent intermediate scattering function: Fig. 5.9; MSD: figures 5.11 and 5.12). Thereby it was observed that interestingly for T_c the most pronounced differences in the dynamics of these two system sizes were found. It is not clear how these findings can be interpreted. In the future the findings should be complemented by studying an even larger system. By this it would be possible to check how the observed differences in the dynamics evolve with the system size. If our findings are confirmed, one could conclude that although at the critical temperature of the ideal MCT not a total dynamical arrest is observed, the dynamics seem to change qualitatively.

Appendix A

Tables

In the following tables we summarize the simulation parameters (A.1) and report the numerical values of the relaxation times (A.2 and A.3), the density (A.4), the bulk modulus (A.5) and the shear modulus (A.6).

integration time step	NVT: Tdamp	NPT: Tdamp	NPT: Pdamp
0.005	0.1	10	75

Table A.1: Simulation parameters used for the systems with $p = 0$ and $N = 64, 32, 16, 8, 4$. The Tdamp / Pdamp parameter specifies how rapidly the temperature / pressure is relaxed [51]. For the systems with $p = 1$ the same parameter set is used. The used parameters are chosen such that they fulfill the criteria described in Ref. [73].

T	$N = 64$	$N = 32$	$N = 16$	$N = 8$	$N = 4$
0.36					4.44089×10^6
0.37					949525
0.38					246795
0.39				2.13892×10^6	85233.6
0.40				658706	33161.2
0.41			2.34229×10^6	246692	
0.42			1.03979×10^6	108388	
0.43		2.59966×10^6	434806		
0.44	9.47817×10^6	1.30924×10^6	215894	32340.9	3664.05
0.45	4.84449×10^6	666717			
0.46	2.47327×10^6				
0.48	1.08361×10^6				
0.50	647803	117530	23717.6	4601.86	782.66
0.70	50587.2	10718.7	2260.14	516.646	111.357
1.00	12074.2	2549.07	596.687	141.315	32.7051

Table A.2: Survey of relaxation times: For the systems with a pressure of $p = 0$ the relaxation time τ_{relax} is given. τ_{relax} correponds to the time interval in which the orientational correlation function of the end-to-end-vector, $\phi_{\text{e}}(t)$, has relaxed to 0.1: $\phi_{\text{e}}(\tau_{\text{relax}}) = 0.1$. The relaxation times are determined from a run in the NVT ensemble.

T	$N = 10\ n = 800$	$N = 10\ n = 100$
0.43	5.60663×10^6	
0.44	1.6253×10^6	1.72823×10^6
0.45	638440	868551
0.46	278558	339260
0.47	155734	
0.48	84613.6	
0.50	34311.6	34500.5
1.00	346.12	351.418

Table A.3: Survey of relaxation times: For the systems with a pressure of $p = 1$ the relaxation time τ_{relax} is given. τ_{relax} correponds to the time interval in which the orientational correlation function of the end-to-end-vector, $\phi_{\text{e}}(t)$, has relaxed to 0.1: $\phi_{\text{e}}(\tau_{\text{relax}}) = 0.1$. The relaxation times are determined from a run in the NVT ensemble.

T	$N = 64$	$N = 32$	$N = 16$	$N = 8$	$N = 4$
0.36					1.02580
0.37					1.02230
0.38					1.01931
0.39				1.03149	1.01615
0.40				1.02818	1.01267
0.41			1.03311	1.02522	
0.42		1.03396	1.02997	1.02191	
0.43		1.03096	1.02688		
0.44	1.02985	1.02789	1.02390	1.01576	0.99941
0.45	1.02688	1.02486			
0.46	1.02391				
0.48	1.01792				
0.50	1.01193	1.00980	1.00550	0.99684	0.97947
0.70	0.95462	0.95192	0.94657	0.93570	0.91358
1.00	0.87456	0.87084	0.86313	0.84746	0.81472

Table A.4: Density ρ as a function of the temperature T for N=64,32,16,8,4.

T	$N = 64$	$N = 32$	$N = 16$	$N = 8$	$N = 4$
0.36					37.4746
0.37					38.0425
0.38					36.3333
0.39				38.0227	35.3873
0.40				37.5067	34.1172
0.41			37.4682	36.3409	
0.42		37.5582	36.9232	35.2078	
0.43		36.6071	36.1268		
0.44	36.4644	35.8789	35.0838	33.7902	31.0700
0.45	35.6703	35.1631			
0.46	34.9340				
0.48	33.5773				
0.50	32.3471	31.9424	31.0951	29.7592	27.0134
0.70	22.6267	22.2413	21.4544	20.0960	17.5000
1.00	13.3534	12.9897	12.2217	10.8711	8.45599

Table A.5: Bulk modulus $K(T)$ as a function of the temperature T for N=64,32,16,8,4.

T	$N = 64$	$N = 32$	$N = 16$	$N = 8$	$N = 4$
0.38					79.8422
0.39				93.2129	77.9908
0.40				88.7825	79.1402
0.41			92.5351	89.2449	
0.42		94.6029	92.2997	87.6220	
0.43		94.0628	91.9207		
0.44	94.6634	93.6428	91.5402	86.7888	77.3178
0.45	94.8497	93.6448			
0.46	94.5608				
0.48	93.6125				
0.50	92.8976	91.6347	89.1075	84.5495	74.9590
0.70	85.6090	84.5181	82.0420	77.0911	67.7084
1.00	76.4073	75.1542	72.5174	67.5512	57.8094

Table A.6: Shear modulus $G_\infty(T)$ as a function of the temperature T for N=64,32,16,8,4.

Bibliography

[1] M. Aichele. *Simulation Studies of Correlation Functions and Relaxation in Polymeric Systems.* PhD thesis, Johannes Gutenberg-University Mainz, 2003.

[2] M. Aichele and J. Baschnagel. Glassy dynamics of simulated polymer melts : Coherent scattering and van Hove correlation functions Part I : Dynamics in the β-relaxation regime. *Eur. Phys. J. E*, 5:229–243, 2001.

[3] M. Aichele and J. Baschnagel. Glassy dynamics of simulated polymer melts : Coherent scattering and van Hove correlation functions Part II : Dynamics in the α-relaxation regime. *Eur. Phys. J. E*, 5:245–256, 2001.

[4] M. Aichele, S.-H. Chong, J. Baschnagel, and M. Fuchs. Static properties of a simulated supercooled polymer melt: Structure factors, monomer distributions relative to the center of mass, and triple correlation functions. *Phys. Rev. E*, 69(6):1–14, 2004.

[5] M. P. Allen and D. J. Tildesley. *Computer Simulation of Liquids.* Clarendon Press, Oxford, 1987.

[6] H. Andersen. Molecular dynamics simulations at constant pressure and/or temperature. *J. Chem. Phys.*, 72:2384, 1980.

[7] C. A. Angell. Formation of Glasses from Liquids and Biopolymers. *Science*, 267(5206):1924–1935, 1995.

[8] R. Auhl, R. Everaers, G. S. Grest, K. Kremer, and S. J. Plimpton. Equilibration of long chain polymer melts in computer simulations. *J. Chem. Phys.*, 119(24):12718, 2003.

[9] U. Balucani and M. Zoppi. *Dynamics of the liquid State.* Oxford University Press, Oxford, 2003.

[10] A. Barbieri, D. Prevosto, M. Lucchesi, and D. Leporini. Static and dynamic density effects due to the finite length of polymer chains: a molecular-dynamics investigation. *J. Phys.: Condens. Matter*, 16(36):6609–6618, 2004.

[11] J. Baschnagel and F. Varnik. Computer simulations of supercooled polymer melts in the bulk and in confined geometry. *J. Phys.: Condens. Matter*, 17(32):R851–R953, 2005.

[12] C. Bennemann, J. Baschnagel, and W. Paul. Molecular-dynamics simulation of a glassy polymer melt: Incoherent scattering function. *Eur. Phys. J. B*, 10:323–334, 1999.

[13] C. Bennemann, J. Baschnagel, W. Paul, and K. Binder. Molecular-dynamics simulation of a glassy polymer melt: Rouse model and cage effect. *Comput. Theo. Polym. Sci.*, 9:217–226, 1999.

[14] C. Bennemann, W. Paul, J. Baschnagel, and K. Binder. Investigating the influence of different thermodynamic paths on the structural relaxation in a glass forming polymer melt. *J. Phys.: Condens. Matter*, 11(10):2179–2192, 1999.

[15] C. Bennemann, W. Paul, K. Binder, and B. Dünweg. Molecular-dynamics simulations of the thermal glass transition in polymer melts: α-relaxation behavior. *Phys. Rev. E*, 57(1):843–851, 1998.

[16] M. Bernabei, A. J. Moreno, and J. Colmenero. The role of intramolecular barriers on the glass transition of polymers: Computer simulations versus mode coupling theory. *J. Chem. Phys.*, 131(20):204502, 2009.

[17] L. Berthier and G. Biroli. Theoretical perspective on the glass transition and amorphous materials. *Rev. Mod. Phys.*, 83(2):587–645, 2011.

[18] K. Binder and W. Kob. *Glassy Materials and Disordered Solids: An Introduction to Their Statistical Mechanics*. World Scientific, Singapore, 2011.

[19] J. Buchholz, W. Paul, F. Varnik, and K. Binder. Cooling rate dependence of the glass transition temperature of polymer melts: a molecular dynamics study. *J. Chem. Phys.*, 117:7364–7372, 2002.

[20] A. Cavagna. Supercooled liquids for pedestrians. *Phys. Rep.*, 476(4-6):51–124, 2009.

[21] P. M. Chaikin and T. C. Lubensky. *Principles of condensed matter physics.* Cambridge University Press, Cambridge, 1997.

[22] S.-H. Chong, M. Aichele, H. Meyer, M. Fuchs, and J. Baschnagel. Structural and conformational dynamics of supercooled polymer melts: Insights from first-principles theory and simulations. *Phys. Rev. E*, 76(5):1–22, 2007.

[23] S.-H. Chong and M. Fuchs. Mode-coupling theory for structural and conformational dynamics of polymer melts. *Phys. Rev. Lett.*, 88:185702, 2002.

[24] P.-G. de Gennes. *Scaling Concepts in Polymer Physics.* Cornell University Press, Ithaca, 1996.

[25] P. G. Debenedetti and F. H. Stillinger. Supercooled liquids and the glass transition. *Nature*, 410:259, 2001.

[26] M. Doi and S. F. Edwards. *The theory of polymer dynamics.* Oxford University Press, Oxford, 1988.

[27] E. Donth. *The Glass Transition.* Springer, Berlin–Heidelberg, 2001.

[28] M. Durand. *Molecular dynamics simulations of oligomer diffusion in polymer melts.* PhD thesis, Université de Strasbourg, 2010.

[29] J. Farago, A. N. Semenov, H. Meyer, J. P. Wittmer, A. Johner, and J. Baschnagel. Mode-coupling approach to polymer diffusion in an unentangled melt. i. the effect of density fluctuations. *Phys. Rev. E*, 85:051806, 2012.

[30] P. J. Flory. *Principles of Polymer Chemistry.* Cornell University Press, Ithaca, 1953.

[31] D. Frenkel and B. Smit. *Understanding molecular simulation.* Academic Press, San Diego, 2002.

[32] M. Fuchs. Private communication.

[33] T. Gleim and W. Kob. The β-relaxation dynamics of a simple liquid. *Eur. Phys. J. B*, 13:83–86, 2000.

[34] W. Götze. Aspects of structural glass transitions. In J. P. Hansen, D. Levesque, and J. Zinn-Justin, editors, *Proceedings of the Les Houches Summer School of Theoretical Physics, Les Houches 1989, Session LI*, pages 287–503. North-Holland, Amsterdam, 1991.

[35] W. Götze. The essentials of the mode-coupling theory for glassy dynamics. *Condens. Mat. Phys.*, 1:873, 1998.

[36] W. Götze. Recent tests of the mode-coupling theory for glassy dynamics. *J. Phys.: Condens. Matter*, 11:A1, 1999.

[37] W. Götze. *Complex Dynamics of Glass-Forming Liquids: A Mode-Coupling Theory*. Oxford University Press, Oxford, 2009.

[38] W. Götze and L. Sjögren. Relaxation processes in supercooled liquids. *Rep. Prog. Phys.*, 55:241, 1992.

[39] W. W. Graessley. *Polymeric Liquids & Networks: Structure and Properties*. Taylor & Francis, New York, 2004.

[40] J.-P. Hansen and I. R. McDonald. *Theory of simple liquids*. Academic Press, London, 3rd edition, 2006.

[41] W. G. Hoover. Canonical dynamics: Equilibrium phase-space distributions. *Phys. Rev. A*, 31:1695, 1985.

[42] J. Horbach, W. Kob, K. Binder, and C. A. Angell. Finite size effects in simulations of glass dynamics. *Phys. Rev. E*, 54:R5897–R5900, 1996.

[43] R. Hoy, K. Foteinopoulou, and M. Kröger. Topological analysis of polymeric melts: Chain-length effects and fast-converging estimators for entanglement length. *Phys. Rev. E*, 80(3):14–16, 2009.

[44] S. Ibold. Kunststoffe in der Küche. Homepage der Abteilung Didaktik der Chemie, Freie Universität Berlin. (Online), 2001. Available: http://www.chemie.fu-berlin.de/chemistry/kunststoffe/kueche.htm (25.05.2012).

[45] J. Jäckle. Expected influence of spatial confinement on glass transitions. *J. Phys. IV France*, 10:Pr7–3–Pr7–7, 2000.

[46] R. A. L. Jones. *Soft Condensed Matter*. Oxford University Press, Oxford, 2002.

[47] W. Kob and H. C. Andersen. Testing mode-coupling theory for a supercooled binary lennard-jones mixture: The van hove correlation function. *Phys. Rev. E*, 51(5):4626–4641, 1995.

[48] K. Kremer and G. S. Grest. Dynamics of entangled linear polymer melts: A molecular-dynamics simulation. *J. Chem. Phys.*, 92(8):5057, 1990.

[49] LAMMPS Molecular Dynamics Simulator. (Online).
Available: http://lammps.sandia.gov (25.05.2012).

[50] LAMMPS Molecular Dynamics Simulator. (Online).
Available: http://lammps.sandia.gov/doc/fix_deform.html (25.05.2012).

[51] LAMMPS Molecular Dynamics Simulator. (Online).
Available: http://lammps.sandia.gov/doc/fix_nh.html (25.05.2012).

[52] W. B. Lee and K. Kremer. Entangled Polymer Melts: Relation between Plateau Modulus and Stress Autocorrelation Function. *Macromolecules*, 42:6270–6276, 2009.

[53] L. Leuzzi and T. M. Nieuwenhuizen. *Thermodynamics of the Glassy State*. Taylor & Francis, Boca Raton, 2008.

[54] A. E. Likhtman, S. K. Sukumaran, and J. Ramirez. Linear viscoelasticity from molecular dynamics simulation of entangled polymers. *Macromolecules*, 40:6748, 2007.

[55] J. F. Lutsko. Generalized expressions for the calculation of elastic constants by computer simulation. *J. Appl. Phys.*, 65:2991, 1989.

[56] T. C. B. McLeish. Tube theory of entangled polymer dynamics. *Adv. Phys.*, 51:1379, 2002.

[57] S. Melchionna, G. Ciccotti, and B. L. Holian. Hoover NPT dynamics for systems varying in shape and size. *Molec. Phys.*, 78(3):533–544, 1993.

[58] H. Meyer. Private communication.

[59] H. Meyer and F. Müller-Plathe. Formation of chain-folded structures in supercooled polymer melts. *J. Chem. Phys.*, 115:7807–7810, 2001.

[60] H. Meyer and F. Müller-Plathe. Formation of Chain-Folded Structures in Supercooled Polymer Melts Examined by MD Simulations. *Macromolecules*, 35:1241–1252, 2002.

[61] K. L. Ngai. *Relaxation and Diffusion in Complex Systems.* Springer, New York, 2011.

[62] S. Nosé. A molecular dynamics method for simulations in the canonical ensemble. *Molec. Phys.*, 52:255, 1984.

[63] S. Nosé. A unified formulation of the constant temperature molecular dynamics methods. *J. Chem. Phys.*, 81:511, 1984.

[64] S. Peter. *Structure et relaxation structurale des fondus de polymères vitrifiables en couches minces.* PhD thesis, Université Louis Pasteur Strasbourg, 2007.

[65] S. Peter, H. Meyer, and J. Baschnagel. Thickness-dependent reduction of the glass transition temperature in thin polymer films with a free surface. *J. Polym. Sci. B*, 44:2951–67, 2006.

[66] S. Peter, H. Meyer, and J. Baschnagel. MD Simulation of Concentrated Polymer Solutions: Structural Relaxation near the Glass Transition. *Eur. Phys. J. E*, (28):147–158, 2009.

[67] S. Plimpton. Fast Parallel Algorithms for Short-Range Molecular Dynamics. *J. Comput. Phys.*, 117:1–19, 1995.

[68] M. Rubinstein and R. H. Colby. *Polymer Physics.* Oxford University Press, Oxford, 2003.

[69] B. Schnell, H. Meyer, C. Fond, J. P. Wittmer, and J. Baschnagel. Simulated glass-forming polymer melts: glass transition temperature and elastic constants of the glassy state. *Eur. Phys. J. E*, 34(9):97, 2011.

[70] H. Schulz. *Statistische Physik. Beruhend auf Quantentheorie. Eine Einführung.* Harri Deutsch, Frankfurt am Main, 1st edition, 2005.

[71] G. Strobl. *The Physics of Polymers: Concepts for Understanding their Structures and Behavior.* Springer, Berlin–Heidelberg, 1997.

[72] W. C. Swope, H. C. Andersen, P. H. Berens, and K. R. Wilson. A computer simulation method for the calculation of equilibrium constants for the formation of physical clusters of molecules: Application to small water clusters. *J. Chem. Phys.*, 76(1):637, 1982.

[73] F. Varnik. *Molecular Dynamics Simulations on the Glass Transition in Macromolecular Films*. PhD thesis, Johannes Gutenberg-Universität Mainz, 2000.

[74] L. Verlet. Computer "Experiments" on Classical Fluids. I. Thermodynamical Properties of Lennard-Jones Molecules. *Phys. Rev.*, 159:98–103, 1967.

[75] M. Vladkov and J.-L. Barrat. Linear and Nonlinear Viscoelasticity of a Model Unentangled Polymer Melt: Molecular Dynamics and Rouse Modes Analysis. *Macromol. Theory Simul.*, 15(3):252–262, 2006.

[76] T. Voigtmann, A. M. Puertas, and M. Fuchs. Tagged-particle dynamics in a hard-sphere system: mode-coupling theory analysis. *Phys. Rev. E*, 70:061506, 2004.

[77] F. Weysser. Private communication.

[78] F. Weysser, A. M. Puertas, M. Fuchs, and T. Voigtmann. Structural relaxation of polydisperse hard spheres: Comparison of the mode-coupling theory to a langevin dynamics simulation. *Phys. Rev. E*, 82:011504, 2010.

[79] J. Wittmer, P. Beckrich, H. Meyer, A. Cavallo, A. Johner, and J. Baschnagel. Intramolecular long-range correlations in polymer melts: The segmental size distribution and its moments. *Phys. Rev. E*, 76(1):1–18, 2007.

Propriétés viscoélastiques des fondus de polymères vitrifiables

Thèse soutenue par Stephan Frey le 29 juin 2012 (Université de Strasbourg)

Résumé À l'approche de la transition vitreuse les fondus de polymères montrent une augmentation importante de la viscosité de plusieurs ordres de grandeur. Le but de cette étude est d'acquérir une compréhension plus profonde des propriétés viscoélastiques des fondus de polymères vitrifiables. Les polymères sont modélisés comme des chaînes flexibles en utilisant un modèle de bille-ressort. Nous étudions des polymères avec différentes longueurs de chaîne pour lesquels nous analysons les propriétés statiques et dynamiques pour une gamme de température proche de la température de transition vitreuse. Les propriétés dynamiques sont analysées dans le cadre de la théorie de couplage de mode idéale. Nous constatons que la température critique de couplage de mode varie avec l'inverse de la longueur de chaîne. Cette loi d'échelle se retrouve également pour les propriétés statiques. En étudiant la fonction de relaxation de cisaillement, nous constatons que les processus de relaxation polymériques, qui peuvent être décrits par la théorie de Rouse, ne sont pas modifiés, mais décalés vers des temps plus importants en approchant la transition vitreuse. Dans cette gamme de température la relaxation monomérique est prolongée de plusieurs ordres de grandeur. De plus, nous analysons les effets de taille finie sur la dynamique du fondu de polymère près de la transition vitreuse, et nos résultats suggèrent que la dynamique est modifiée qualitativement à la température critique de couplage de mode.

Summary Polymer melts show a remarkable increase of their viscosity by many orders of magnitude on approaching the glass transition. The aim of this study is to gain a deeper insight into the viscoelastic properties of glass forming polymer melts. The polymers are modeled as flexible chains using a bead-spring model. We investigate polymers with different chain lengths for which we analyze the static and dynamic properties for a temperature range close to the glass transition temperature. The dynamic properties are analyzed in the framework of the ideal mode-coupling theory. We find that the critical temperature of the ideal mode-coupling theory scales with the reciprocal chain length. This scaling is also found for the static properties. By studying the shear relaxation function we find that the polymer relaxation processes, which can be described by the Rouse theory, are not altered but shifted to later times in the approach of the glass transition. In this temperature range the monomer relaxation is protracted by many orders of magnitude. Additionally, we analyze finite size effects on the dynamics of polymer melts close to the glass transition. Our findings of this case study suggest that the dynamics change qualitatively at the critical temperature of the ideal mode-coupling theory.

Keywords: Glass-forming polymer melts, molecular dynamics simulation, mode-coupling theory, Rouse theory, shear relaxation function, viscoelasticity, bead-spring model